HOLISTIC ENERGY MANAGEMENT AND THERMAL WASTE INTEGRATED SYSTEM FOR ENERGY OPTIMIZATION

HEATWISE

Development and validation of open-source CFD model for thermal analyses of IT systems

Project ID: 101138491

Prepared by: DSTECH

October, 2024

Development and validation of open-source CFD model for thermal analyses of IT systems

Project acronym	**HEATWISE**
Project title	Holistic Energy Management and Thermal Waste Integrated System for Energy Optimization
GA Number	101138491
Call identifier	HORIZON-CL5-2023-D4-01
Topic identifier	HORIZON-CL5-2023-D4-01-04
Project duration	36 months
Related work package	WP4 Theoretical validation of pilot configurations
Deliverable no.	D4.1
Dissemination Level	Public
Deliverable type	Other
Due Date of deliverable	October 2024
Completion date of deliverable	21. October 2024
Coordinator	H1 Systems
Website	www.heatwise.eu

Lead beneficiary of deliverable	DSTECH
Author(s)	Yılmaz, Sibel Kuzay, Mustafa Sarıkaya, Onur Muhammed Demirel, Ender
Contributor(s)	
Reviewer(s)	Jensen, Rasmus L. Melgaard, Simon P.
Keywords	CFD modelling, Thermal analysis, Data centre, Two-phase, Boiling Heat Transfer

Document history:

Revision	Date	Status
V0.1	20.09.2024	Initial draft
V0.8	20.09.2024	Draft for review
V0.9	09.10.2024	Final draft after implementing comments, ready for editing
V0.9.1	16.10.2024	Final draft after editing, ready for approval
V1.0	22.10.2024	Final report

Disclaimer

The European Commission's and the Swiss Secretariat for Education, Research, and Innovation's support for the production of this publication does not constitute endorsement of the contents which reflects the views only of the authors, and the

Commission cannot be held responsible for any use which may be made of the information contained therein.

Table of contents

Executive Summary

Data centres (DC) are estimated to account for 3% of European Union (EU) electricity demand by 2030. The energy efficiency directive (EED) adopted by the EU in January 2024 sets new standards for rating the energy efficiency of data centres based on key performance indicators (KPIs) focusing on energy and sustainability, information and communication technologies (ICT) equipment and data traffic. As also indicated in the EU code of conduct for energy efficiency in data centres, thermal and cooling efficiencies of existing data centres need to be reevaluated for an efficient airflow and reinforced hot/cold aisle design to align with the objectives of the EED. Airflow and thermal structures should be thoroughly investigated not only to reveal the underlying mechanism that reduces thermal efficiency of a data centre but also to propose retrofitting alternatives. In addressing this need, Computational Fluid Dynamics (CFD) has emerged as an effective tool for the simulations of flow and thermal structures in data centres with the rapid developments in computer technologies in recent years.

The aim of this study is to develop and validate an open-source CFD model for the thermal analysis of information technologies (IT) systems. To this end, the dataCenterDST software has been developed based on OpenFoam libraries for the thermal simulations of pilot sites. The IT components are modelled using an open-box server model, where heat sources, fans, flow rate and pressure drop can be modelled in detail to adjust various workloads and server models. In this scope, a virtual wind tunnel has been developed for the modelling of pressure drop through the Open Compute Project (OCP) server using the Darcy-Forchheimer porosity model. A series of numerical simulations performed under various airflow rates demonstrated that the proposed porous model can predict pressure drop between inlet and outlet of the server reliably even on a coarse mesh.

The Computational Fluid Dynamics (CFD) model developed in this study has been enhanced with a Conjugate Heat Transfer (CHT) capability, representing a significant advancement in the simulation accuracy of data centre thermal management. The CHT feature allows for a more comprehensive and realistic modelling of the heat transfer processes by treating air, liquid, and solid regions separately. In order to validate the present CHT model, experimental studies were conducted at Empa pilot site using various water flow rates and fan speeds of the cooling system. Comparison of the numerical results with the experimental data proved that the present CHT model could accurately

---

predict air and water temperatures at the outlet of the cooling system. Thus, the present model can be used reliably for the maximization of waste heat recovery from a data centre by optimizing the workload traffic.

Another objective of the present study is to develop an open-source CFD model for the simulation of two-phase heat transfer, which is a cutting-edge solution for the state-of-art at both academia and industry. The two-phase heat transfer model focuses on simulating the complex interactions between liquid and vapor phases within a data centre cooling system. By accurately capturing the phase change phenomena, such as boiling and condensation, this model offers significant improvements over traditional single-phase cooling simulations. The CHT part of the two-phase heat transfer plays an important role in the realistic modelling of the heat removal system since the heat generated by electronic components can be removed by the phase-change heat transfer for an effective cooling. The present open-source two-phase model twoPhaseCoolDST has been validated on the one-dimensional Stefan and two-phase film boiling problems. Numerical simulations conducted under various thermal conditions showed that the present phase-change model could capture formations of bubbles, as well as heat transfer mechanism between heat source and liquid accurately. This study was accepted to present as poster in 2024 OCP Future Technologies Symposium organized under OCP Global Summit. During the development and validation studies of the two-phase heat transfer model, a novel micro-baffle design has been developed and optimized for the heat transfer enhancement in film-boiling. The optimal baffle design achieved a 57.4% improvement in the Nusselt number and a 66.4% increase in the critical heat flux (CHF). Furthermore, the proposed design facilitated continuous bubble formation even with a reduced temperature difference between the heated surface and the subcooled liquid, which is crucial for energy-efficient thermal management in engineering systems. Results of this study have been published as an open-access paper with gold access, which disseminates the scientific impact of the HEATWISE project. Finally, the validated two-phase model is implemented to the direct-to-chip two-phase cooling system to be demonstrated during project studies.

List of abbreviations

Acronym	Meaning
EU	European Union
EED	Energy Efficiency Directive
DC	Data Centre
BEMS	Building Energy Management System
DLC	Direct Liquid Cooling
PUE	Power Usage Effectiveness
ICT	Information and Communication Technologies
CHT	Conjugate Heat Transfer
CPU	Central Process Unit
IT	Information Technology
CFD	Computational Fluid Dynamics
HPC	High Performance Computing
CSO	Central Statistics Office
CAD	Computer Aided Design
OCP	Open Compute Project
MTG	Medium Temperature Grid
LTG	Low Temperature Grid
STL	Standard Triangle Language

RANS	Reynolds Averaged Navier Stokes
SIMPLE	Semi Implicit Method for Pressure Linked Equations
PISO	Pressure Implicit With Splitting of Operator
IBM	International Business Machines
RMSE	Root Mean Square Error
VOR	Valve Opening Ratio
VOF	Volume of Fluid
IFS	Inverter Fan Speed
CSF	Continuum Surface Force
GAMG	Generalised Geometric Algebraic MultiGrid
HRU	Heat Rejection Unit
TDP	Thermal Design Power
TRP	Total Rack Power

1. Introduction

Rapid advancements in IT capacity have highlighted the crucial role played by data centres (DCs) with exceptional performance and increasing demand in recent years. These facilities are associated with high energy usage and significant carbon emissions [1,2,3,4]. Global emissions from cloud computing account for approximately 2.5% to 3.7% of total global greenhouse gas emissions, surpassing the emissions generated by commercial flights and other essential activities that drive the global economy [5].
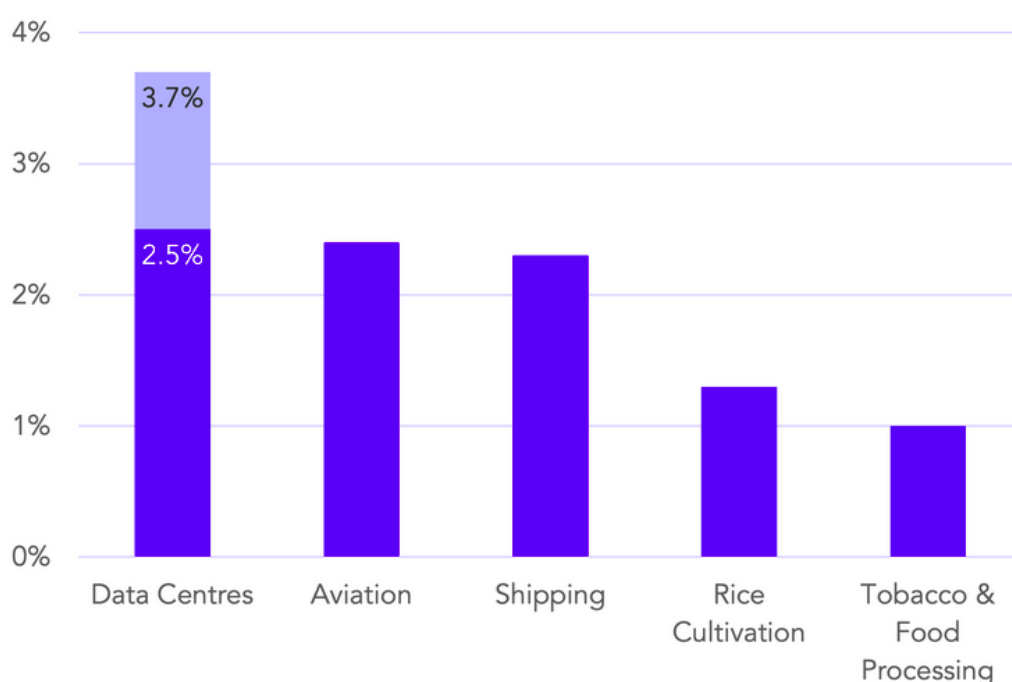
Figure 1.1: Share of global CO2 emission generated by sector [5].

Effective cooling is essential in data centre operations, as it ensures the reliable performance and longevity of the IT equipment by preventing overheating. Additionally, the waste heat generated by IT equipment offers a valuable opportunity for recovery. The excess heat can be utilised in heating buildings, reducing overall energy consumption and enhancing the sustainability of data centre operations by integrating waste heat recovery systems. This dual approach improves energy efficiency by contributing to environmental sustainability and resource optimization [6,7,8,9,10,11].

Electricity usage (TWh) of Data Centers 2010-2030
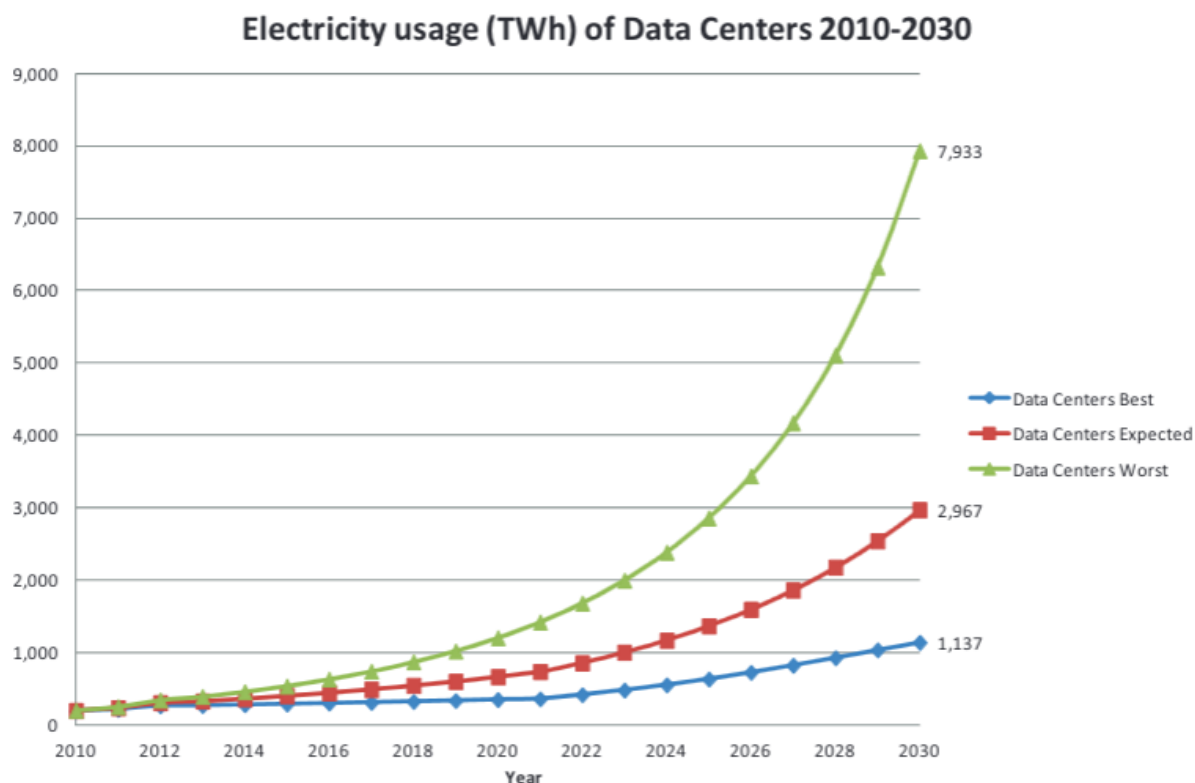
Figure 1.2: Global electricity demand of data centres 2010–2030 [12].

Data centres serve as the critical foundation of IT networks worldwide, encompassing the necessary infrastructure to power and cool IT equipment. These facilities range in complexity from a single rack in a server closet to expansive warehouses, often featuring built-in redundancy to minimise downtime and ensure continuous operation [13,14,15].

Figure 1.3: Fraction of U.S. data centre electricity use [16].

Data centres are significant energy consumers. New figures from the Central Statistics Office (CSO) reveal that energy consumption by Irish data centres increased by 31% during the last year, now accounting for 18% of Ireland's to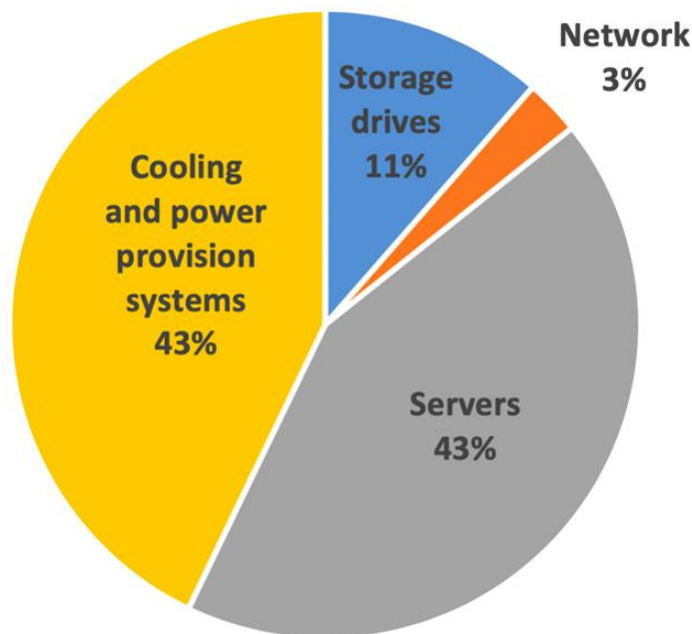tal energy consumption [17]. The operation of data centres alone accounts for about a quarter of these emissions [18] and is considered to have the fastest growing carbon footprint within the entire ICT sector [17]. Their primary goal is to ensure a network environment and services that are safe, stable, efficient, and uninterrupted [19]. The importance of DCs is immense, as they play a crucial role in virtually every aspect of our lives. Air cooling is widely used as a practical option in DCs and high-performance computing (HPC) applications. The maximum heat load that modular air-cooled systems, such as those using in-row [20,21], rear-door [22], and rack-mountable cooling [23,24], can usually handle is 20 kW of heat per rack. Since air has a limited capacity for heat transfer, liquid cooling has been explored as a potential solution. As mentioned in [25], which identifies and discusses the most promising techniques and technologies for recovering low-temperature waste heat from data centres in an efficient and financially feasible manner, there are numerous options for cooling data centres. One potential alternative is on-chip cooling, wherein the primary coolant, such as a liquid or refrigerant, is delivered directly to the main processor and ancillary circuits, thereby replacing traditional air-cooling techniques. Recent researchers have identified four

major competing chip cooling technologies: microchannel single-phase flow, porous medium flow, jet impingement cooling, and microchannel two-phase flow [26]. Research by [27] demonstrated that employing new cooling technologies for chips could lead to energy savings exceeding 60% [26]. Among the four technologies, microchannel two-phase cooling was the most promising. While single-phase microchannel cooling offers the advantage of being relatively easy to implement, its benefits are less pronounced compared to the two-phase approach. This technology is currently utilised in the launched Aquasar project [28], an IBM bladecenter modified to employ a water-cooled cycle. However, using water comes with several drawbacks. It necessitates high pumping power to maintain acceptable temperature gradients on the microprocessor. Additionally, water poses challenges due to its high freezing point, potential for microbe formation, corrosive properties, electrical conductivity, and erosive nature at high fluid velocities. The majority of data centres today are air-cooled, meaning that extra heat is released into the atmosphere, usually with the use of a cooling tower or a chiller. This air-cooled server waste heat has a temperature range of 35 to 45°C, making it suitable for recovery and use to heat neighbouring buildings. Consequently, contemporary data centres have a significant opportunity to reduce their impact on climate change. This is because, in addition to improving system energy efficiency through the use of waste heat recovery for heating [29], they can also reduce the energy consumption of their cooling systems, which accounts for 30%–40% of their overall energy consumption [30]. Data centre waste heat recovery lowers greenhouse gas emissions in addition to saving energy, particularly when it replaces heat production based on fossil fuels. In [31], the effects of eliminating coal in the Despôte (Finland) district heating system were examined, along with the potential for data centre waste heat to serve as an affordable external heat supply for the system. It was determined that by combining the utilisation of waste heat sources and renewable fuels, the city's aim of producing 85% of its heat from carbon-neutral sources could be met [32].

The CFD models are critical tools for optimising waste heat recovery systems, offering detailed analysis of fluid dynamics and heat transfer processes. CFD can be employed to simulate the temperature distribution and particle behaviour within a waste heat recovery boiler, enabling predictions of deposition on boiler walls and ensuring combustion stability [33]. This approach highlights the importance of CFD in optimising boiler design under varying combustion conditions. CFD analysis is useful to assess the heat transfer performance of fin prolonged heat exchangers enhanced with nanofluids

[34]. Furthermore, CFD modelling can be applied to simulate the behaviour of different nanofluids in finned heat exchangers, focusing on their impact on waste heat recovery efficiency [35]. The results underscored the potential of using advanced nanofluids to enhance energy recovery processes. These studies collectively emphasise the pivotal role of CFD in advancing waste heat recovery technologies, particularly in enhancing system efficiency and reducing environmental impact.

Film boiling is of great importance in both industrial and scientific applications due to its distinct thermal features such as high heat flux, a significant temperature difference between the heated surface and the boiling liquid and the formation of a stable vapour film that insulates the surface. Accurate modelling of film boiling is essential for predicting the performance of emergency core cooling systems and ensuring reactor safety in the nuclear industry [36]. Film boiling also plays a vital role in storage and transfer of cryogenic liquids such as nitrogen and hydrogen. Understanding the heat transfer mechanism is essential for designing efficient insulation and heat transfer to minimise evaporation losses in these applications [37]. Quenching processes in the metallurgical industry has emerged as another application area of film boiling. As the hot metal is immersed in a coolant, film boiling occurs initially, followed by a transition to nucleate boiling. Controlling the transition between these boiling regimes is essential for achieving desired mechanical properties in metals [38]. Film boiling is widely utilised in spacecraft thermal management systems since spacecraft often experiences extreme temperature variations and film boiling can be used to manage heat transfer during re-entry or in cryogenic fuel tanks [39]. Therefore, managing film boiling has attracted a significant interest in various engineering applications in recent years.

Researchers have developed various approaches such as addition of surfactants, surface coatings and geometry modifications to enhance heat transfer in film boiling. Surfactants enhance heat transfer by reducing surface tension, leading to smaller bubble diameters and more frequent bubble formation to increase heat transfer during the boiling process. You et al. [40] achieved a significant increase in the Critical Heat Flux (CHF) value using the Al_2O_3. Park et al. [41] demonstrated that the addition of graphene nanofluids could result in 84% increase in the CHF. Adding specific patterns and geometries to the surface is crucial for controlling the formation of vapour bubbles and improving the heat transfer during boiling. Additionally, potential benefits of increasing surface area and geometry makes these approaches viable in terms of heat transfer performance because these modifications enhance nucleation sites, promote more efficient fluid distribution and

reduce thermal resistance. They can significantly improve the overall heat transfer rate by facilitating faster bubble detachment and increasing the surface area of heat exchange. Mori and Okuyama et al. [42] investigated the influence of honeycomb structures on the heat transfer performance and demonstrated that the proposed honeycomb could increase the CHF by 2.5 times compared to that of a flat plate. The use of a porous fence plate in subcooled flow boiling experiments resulted in a 2.3-fold increase in heat transfer performance [43]. This improvement was observed at a specific pitch-to-diameter ratio of 2.5:1.7. On the other hand, Hao et al. [44] investigated the effect of a deformable structure made from shape memory alloy with working fluids such as ethanol, FC-72 and water. A significant increase was achieved in the Heat Transfer Coefficient (HTC) and the adaptive control of boiling heat transfer could be attained using these structures. Surface coatings can modify the energy distribution across a surface, thereby altering vapour bubble formation and enhancing their detachment, thanks to their advantages such as ease of application and the ability to control surface properties. However, the wear of the coating material over time and its inherent thermal resistance can limit their applications. Surtaev et al. [45] studied capillary porous coating to enhance heat transfer in pool boiling. They found that the capillary-porous coating applied by the plasma spraying method had a porosity of 60% with a variable thickness of 400–1390 µm. Coating process increased the heat transfer by 4 times with liquid nitrogen as the working fluid and by 3.5 times for the boiling of water. Das et al. [46] investigated the effect of SiO_2 nanomaterial coating and they achieved 80% increase in the HTC due to the enhanced hydrophilicity and surface cavities.

Both Euler-Euler and Euler-Lagrange models emerge as promising approaches for the numerical modelling of the phase interface in boiling. While homogeneous phases are modelled by Euler conservation equations in the Euler-Lagrange method, the vapour phase is tracked by the motion of individually moving spherical bubbles. On the other hand, the Euler-Euler method can handle any number of phases without major modifications in the formulation, which leads to yield accurate results for well-mixed or dispersed phases in engineering applications such as fluidized beds, bubble columns and spray formation. It effectively models complex interactions such as drag, lift and phase change using less computational resources than other methods that require explicit interface tracking. However, the lack of tracking of sharp interfaces emerges as a drawback in explicit tracking of interfaces. Additionally, it relies on empirical or theoretical closure models to describe phase interactions, which may produce uncertainty and

complexity. To this end, the Euler-Euler approach is often used in conjunction with the volume of fluid (VOF) method based on the assumption that both phases share the same kinematic space. The vapour volume fraction is updated via the solution of a transport equation including the source term associated with mass transfer between liquid and vapour [47, 48, 49, 50]. It uses a single set of momentum equations shared by the fluids and tracks the volume fraction of each phase within each computational cell across the domain. The VOF method accurately handles complex interface phenomena such as breaking waves, splashing and droplet formation to satisfy mass conservation for each phase. Additionally, it provides a clear and accurate representation of the interface, which is critical in the visualisation of bubbles [51, 52, 53, 54, 55, 56, 57, 58]. Moreover, application of open-source software in this context has been relatively rare [59, 60]. An open-source CFD model is developed to simulate bubble dynamics in film boiling. Accuracy of the numerical model is validated by comparing the results with existing experimental and numerical data in the literature. The validated model is then used to optimise geometrical parameters of the proposed design and to maximise heat transfer performance based on thermal characteristics. Performance of the proposed design is evaluated according to various indicators. Numerical simulation results indicate that the proposed design can effectively modify bubble formation to meet specific objectives and provide a significant improvement in heat transfer performance.

2. Numerical Model for the Thermal Simulation of a Data Centre

2.1. Governing Equations

Accurate modelling of heat transfer between air and water can be achieved through a multi-region Conjugate Heat Transfer (CHT) model. This model creates distinct regions for air and water, solving continuity, momentum, and energy equations for each region. It accounts for turbulence and buoyancy effects. The fluid region's compressible and turbulent flow is depicted using unsteady continuity and momentum equations in tensor form, employing Reynolds averaging:

$$\frac{\partial \rho}{\partial t} + \frac{\partial \rho u_j}{\partial x_j} = 0 \tag{1}$$

$$\frac{\partial}{\partial t}(\rho u_i) + \frac{\partial}{\partial x_j}(\rho u_i u_j) = -\frac{\partial p'}{\partial x_i} + \frac{\partial}{\partial x_j}(\mu \frac{\partial u_i}{\partial x_j}) + \frac{\partial}{\partial x_j}(-\rho u_i' u_j') \tag{2}$$

$$p' = p + \frac{2}{3}\rho k + \frac{2}{3}(\mu + \mu_t)\frac{\partial u_k}{\partial x_k} \tag{3}$$

where ρ is the density, t is the time, u_i is the velocity component in the x_i direction, p' is the modified pressure, μ molecular viscosity, μ_t viscosity. The turbulent stress in Eq. (2) can be calculated from the Boussinesq approximation:

$$-\rho u_i' u_j' = \mu_t(\frac{\partial u_i}{\partial x_j} + \frac{\partial u_i}{\partial x_i}) - \frac{2}{3}k\delta_{ij} \tag{4}$$

where k is the turbulent kinetic energy and δ_{ij} is the Knocker delta. In this study $k - \omega$ SST turbulence closure model is employed to simulate turbulence effects in the air region. Laminar flow conditions employed to model the behaviour of the water region. Two transport equations are solved for the kinetic energy k and specific dissipation rate ω [61]. The turbulent viscosity can be calculated from the following equation:

$$\mu_t = \frac{\rho a_1 k}{max(a_1 \omega, SF2)} \tag{5}$$

where S is the strain rate invariant and a_1 is the model constant. The energy equation is solved for the compressible flow:

$$\frac{\partial}{\partial t}(\rho E) + \frac{\partial}{\partial x_i}[u_i(\rho E + p)] = \frac{\partial}{\partial x_j}\left[\lambda_{eff}\frac{\partial T_f}{\partial x_j} + u_i\frac{\partial}{\partial u_j}(\mu\frac{\partial u_i}{\partial x_i} - \rho u_i' u_j')\right] + S_E \qquad (6)$$

where E is the total energy and S_E is the source term. The simplest form of the energy equation, commonly used in the literature, is employed in this study. In calculations where variations in density and specific heat capacity with respect to temperature are considered, these factors have been accounted for [62]. The heat flux q_i can be determined using the following equation:

$$q_i = kn_i\frac{\partial T}{\partial n} \qquad (7)$$

where k is the thermal conductivity and n is the surface normal vector. In a CHT model, energy balance is maintained by solving the energy equation in both fluid and solid regions, ensuring heat transfer continuity at the interfaces. The energy equation accounts for convective and conductive heat transfer in the fluid region, while conduction is modelled within the solid regions. At the boundaries where the fluid and solid meet, the heat flux is matched, ensuring that the heat leaving the fluid region equals the heat entering the solid region, thereby preserving overall energy conservation across the system.

2.2. Numerical Modelling of Servers

A server level CFD model plays a vital role in optimising the thermal and airflow dynamics within data centres. By simulating the detailed behaviour of air and heat around individual servers, it enables the identification of critical inefficiencies, such as localised hot spots, air recirculation, and uneven cooling. Addressing these issues at the server level is essential for preventing overheating, ensuring system reliability, and maximising energy efficiency. These models provide valuable insights that allow data centre operators to implement targeted cooling strategies, reduce energy consumption, lower operational costs, and extend the lifespan of equipment, ultimately leading to more sustainable and high-performance data centre environments.

Figure 2.1: Snapshot of the Leopard V3.1 OCP server.

2.2.1. A Virtual Wind Tunnel for the Modelling of Servers

The virtual wind tunnel simulation is a powerful tool for evaluating the pressure drop through the server components within data centres, providing insights into thermal performance and airflow management. This CFD study aims to analyse the pressure drop in a server environment, where efficient airflow is critical for optimising cooling solutions and maintaining energy efficiency. By simulating the airflow behaviour around server components, the virtual wind tunnel allows for a detailed examination of how different design configurations and cooling strategies impact the pressure drop encountered in the overall system. This approach not only reduces the need for physical testing but also accelerates the design process.
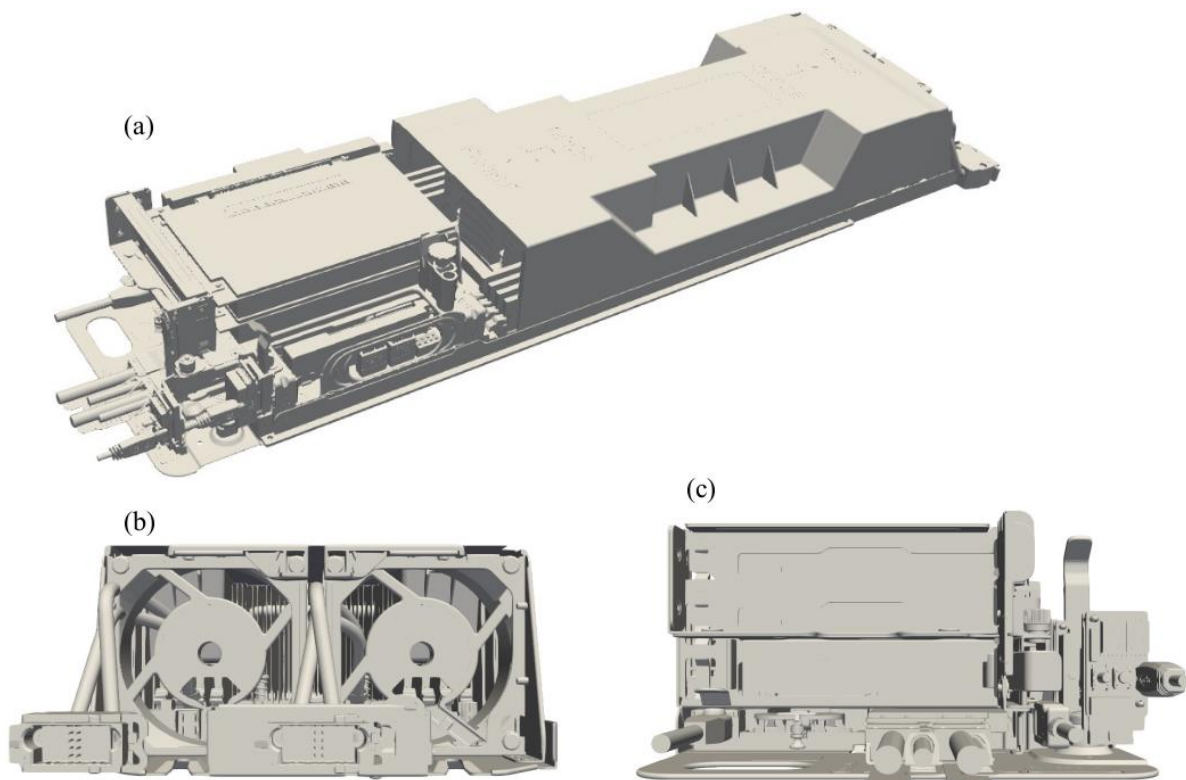
Figure 2.2: Three-dimensional views of the Leopard V3.1 OCP server a) top, b) back and c) front.

Since the original server model used in the experimental studies conducted in the wind tunnel studies had modifications, the same adjustments were applied to the CAD model to ensure accuracy in the simulations. These modifications were crucial for aligning the virtual model with the real-world configuration, allowing the simulations to closely mimic the performance and behaviour of the modified server. By implementing these changes, we ensured that the simulation results would be both reliable and representative of the actual experimental setup, maintaining the integrity and relevance of the overall analysis.
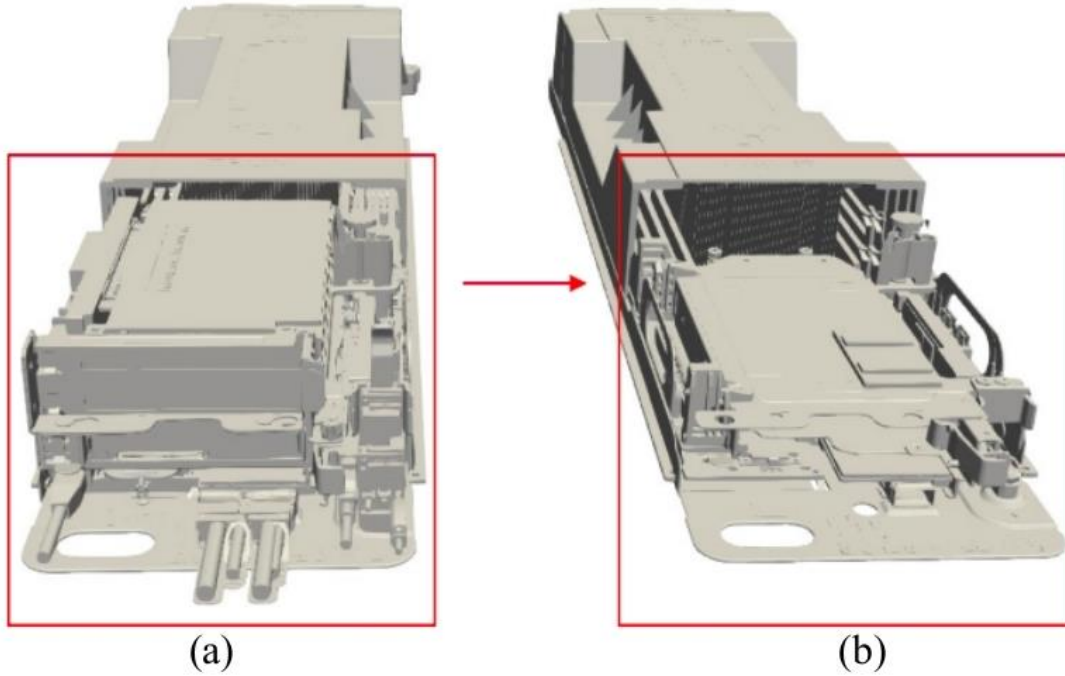
Figure 2.3: Modifications of the Leopard V3.1 OCP server. a) original model and b) modified model.

2.2.2. Modelling Fans

The servers and cooling unit fans inside the data centre were simulated using the fan boundary condition provided in OpenFOAM-v2312 [62]. Fan curves were created specifically for this boundary condition's use, sourced from product data sheets. To enable the utilisation of the fans' operational RPM values, suitable fan curves were produced and integrated by applying fan laws.

$$\frac{cfm_2}{cfm_1} = \frac{rpm_2}{rpm_1} \tag{8}$$

$$\frac{SP_2}{SP_{ref}} = \left(\frac{rpm_2}{rpm_{ref}}\right)^2 \tag{9}$$

The first of the fan laws mentioned above establishes the relationship between fan speed and flow rate, while the second one relates fan speed to pressure jump. An example of using fan boundary conditions in OpenFOAM is provided below.

```
rack1fr21Fan0HalfPlaneMaster
{
    type            fan;
    patchType       cyclic;
    jumpTable       tableFile;
    file            "$FOAM_CASE/constant/fanCurves/ocp2000.0";
    outOfBounds     clamp;
    reverse         yes;
    value           uniform 0;
}

rack1fr21Fan0HalfPlaneSlave
{
    type            fan;
    patchType       cyclic;
    value           uniform 0;
}
```

Figure 2.4: Implementation of fan boundary conditions in OpenFOAM [62].

2.2.3. Modelling Pressure Drop Through the Server

We conducted high-resolution numerical simulations on an OCP server under various inlet flow rates [63], considering both active and inactive conditions. Due to the complexity and computational intensity of modelling the complete server geometry, we adopted a porous media approach. This method effectively reduced the number of cells required in the simulation to just 0.3% of what would be needed for a full detailed model, without compromising accuracy.
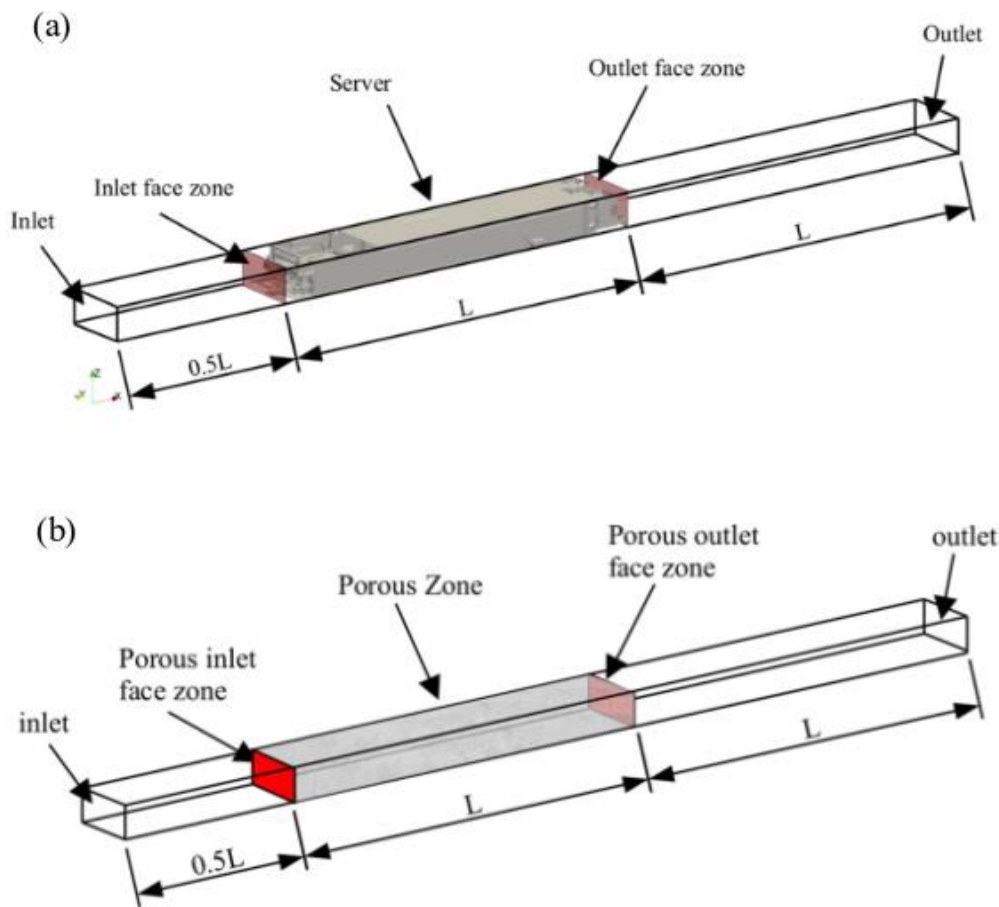
Figure 2.5: Three-dimensional views of the Virtual Wind Tunnel: a) 3D server model and b) porous model.

Key findings from the study include the determination of porosity coefficients that accurately represent the inertia and viscous resistance of the server components. These coefficients enable the efficient prediction of pressure drops within the server, facilitating the design of safer and more energy-efficient air-cooled data centres. The study's results demonstrated that the proposed model could predict pressure drops accurately, making it a valuable tool for data centre designers to ensure optimal cooling and thermal management [63].
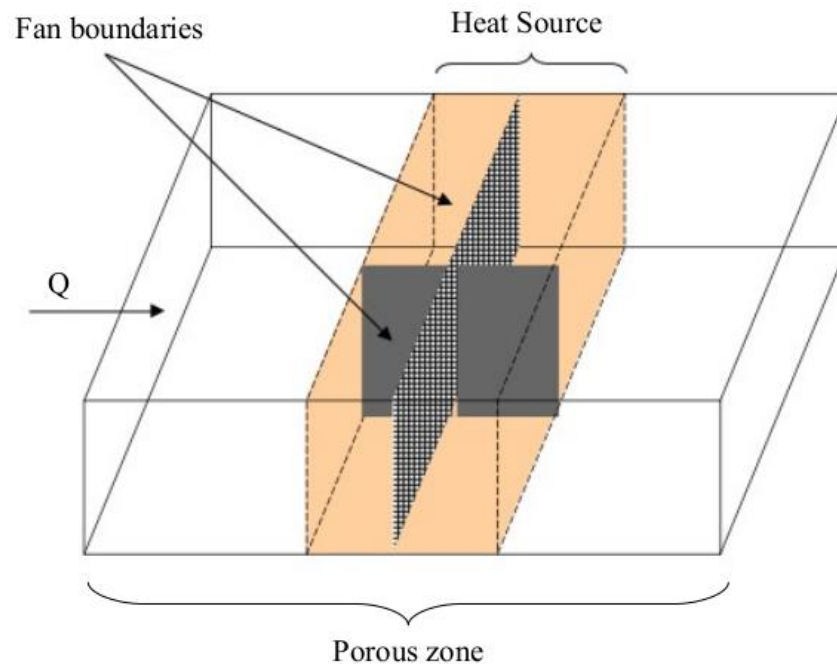
Figure 2.6: Implementation of the heat source and fan boundaries in the porous model.

2.2.4. Mesh Independent Study

In this study, we generated a hexagonal mesh for the OCP Leopard V3.1 server within a virtual wind tunnel to facilitate detailed CFD analysis. Initially, we employed blockMesh to construct the wind tunnel, defining the spatial boundaries and establishing the domain for the simulation. Following this, snappyHexMesh employed to incorporate the server model into the wind tunnel and refine the mesh around its geometry. To enhance computational efficiency, we executed snappyHexMesh in parallel, ensuring the mesh generation process was both precise and time-efficient for subsequent analysis. During this process, two different meshes were generated. Characteristics of each mesh are presented in Table 2.1 to compare their performance and suitability for the study.

Table 2.1: Mesh statistics for the server model.

Mesh	Number of Cells (Million)	Max. Volume	Min. Volume	Max. Skewness	Max. Non-Orthogonality
Mesh1	3.99	1.57×10^{-7}	1.31×10^{-11}	19.28	64.99
Mesh2	4.82	1.24×10^{-7}	1.63×10^{-11}	15.92	64.99

This work constitutes a mesh independency study, where two different meshes were generated and evaluated. Simulations were performed for both meshes, and pressure values at the inlet and outlet were predicted. By comparing these values in the Table2.2, we assessed the consistency of the results, ultimately selecting the most appropriate mesh for further analysis. This approach ensures that the results are not significantly influenced by the mesh resolution, enhancing the reliability of the CFD study. As a result, Mesh 1 was selected for further analysis. This decision was based on the fact that there was no significant difference in the simulation results between the two meshes, and Mesh 1 was more computationally economical, making it the more efficient choice for continued study.

Table 2.2: Pressure drops predicted from each mesh.

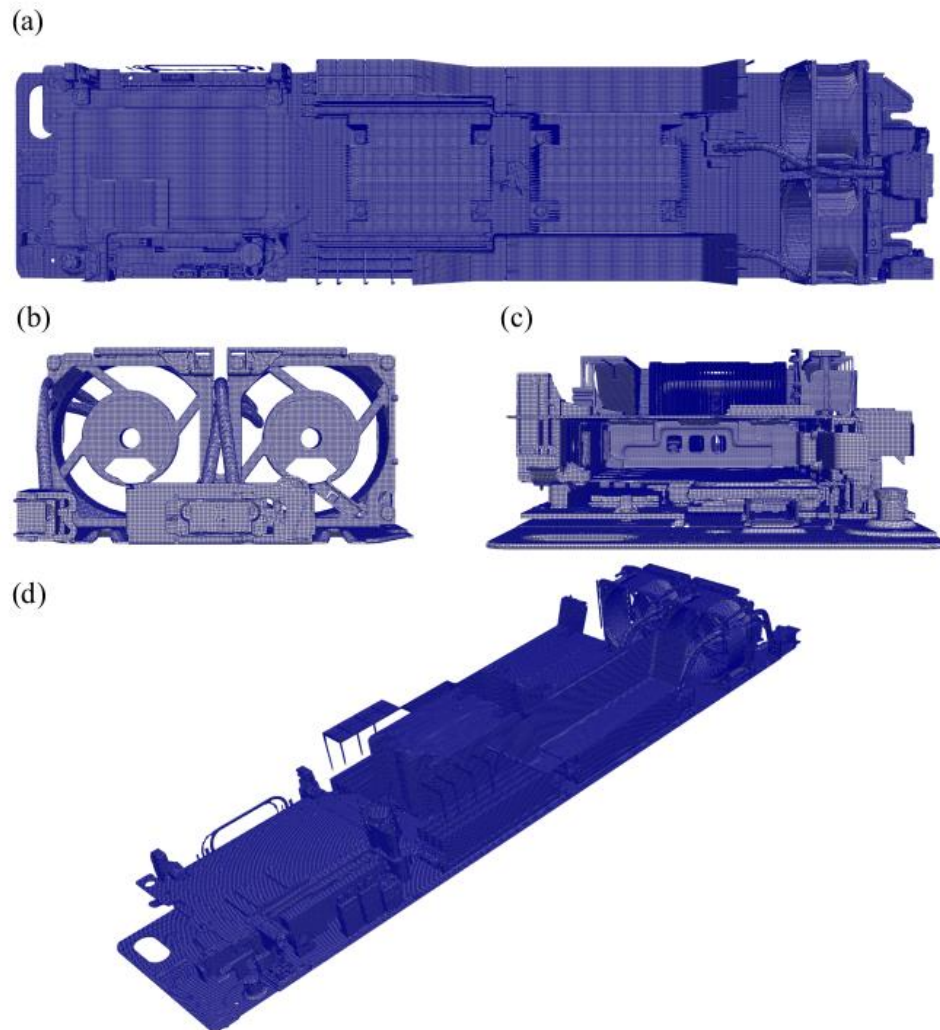| Mesh	Number of Cells (Million)	Pressure Drop (Pa)
Mesh1	3.99	1.92
Mesh2	4.82	1.97

Figure 2.7: Three-dimensional views of the hexahedral mesh for the OCP server: a) top, b) back, c) front and d) isometric views.

2.2.5. Airflow Structure Through the Server

Upon completion of the mesh generation and simulation phases, the subsequent section focuses on post-processing the results to thoroughly analyse the internal flow behaviour within the OCP Leopard V3.1 server. Specifically, the analysis will investigate the flow structure, pressure distribution, and velocity characteristics. This examination is fundamental to understanding the aerodynamic performance within the server, providing insights into how the internal design influences fluid dynamics.

In the accompanying visual representation of the velocity profile for the server, we highlight the regions around specific components where the flow velocity significantly increases. This phenomenon occurs because the cross-sectional areas around these components narrow, causing the flow to accelerate. By zooming in on these areas, the following figure demonstrates how the constriction around components results in higher velocity regions, providing insights into the complex fluid dynamics within the server. This detailed depiction highlights the impact of component placement on the overall flow characteristics.
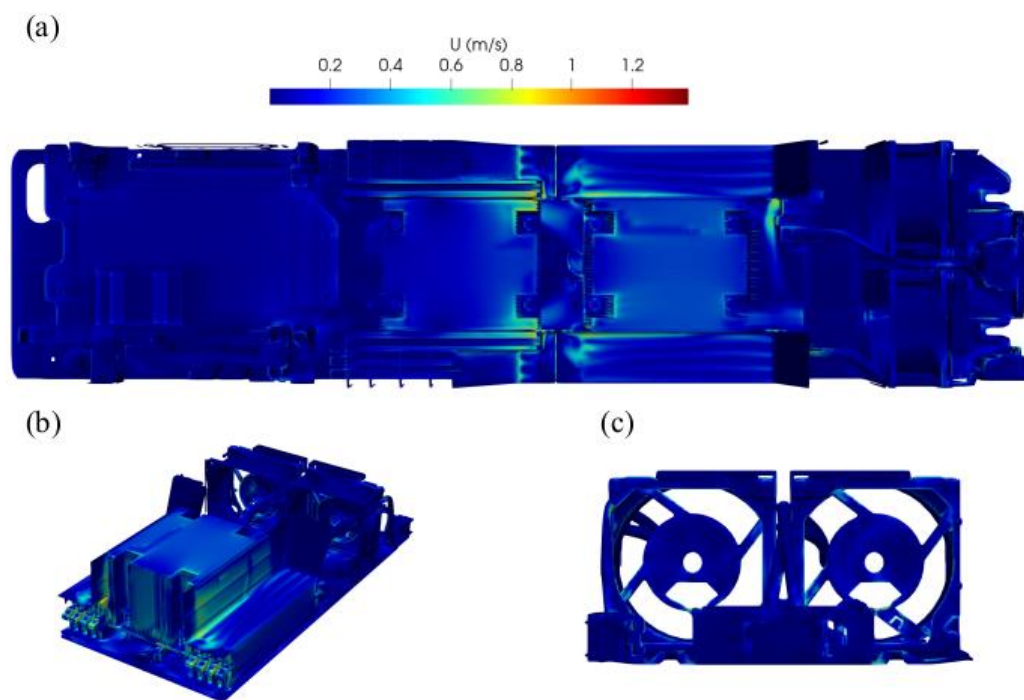

Figure 2.8: Contours for the magnitude of air velocity: a) top, b) heatsink and c) fans.

Following the velocity profile figure, we included a detailed glyph representation that zooms in on the heatsinks and fans. This figure provides a closer examination of how airflow interacts with these critical components, illustrating the direction and magnitude of the velocity vectors. By focusing on the heatsinks and fans, the glyphs offer valuable insights into the localised flow patterns and their impact on cooling performance.
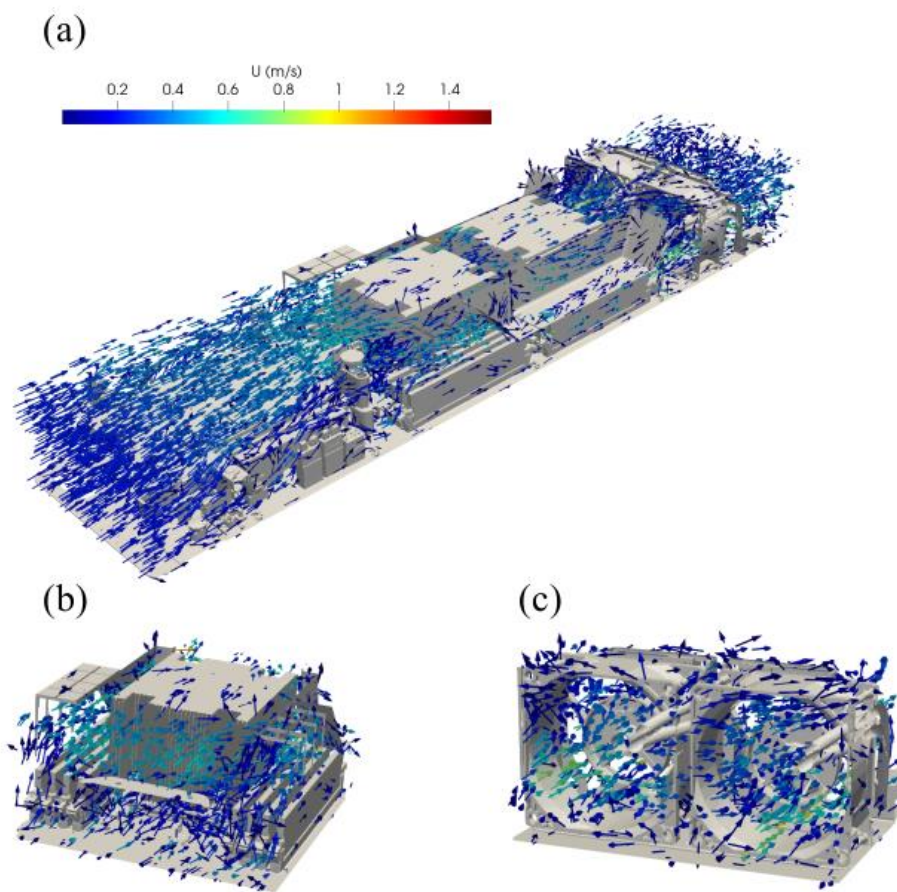
Figure 2.9: Velocity vectors of the airflow through the server: a) top, b) zoom in to the heatsink and c) zoom in to the fans.

The following figure depicts the pressure distribution along the server, which will offer a comprehensive view of how pressure values vary throughout the system, highlighting critical areas where pressure changes significantly. By analysing these patterns, we can uncover insights into the aerodynamic forces and their implications for cooling efficiency. This approach provides a deeper understanding of the pressure dynamics, which is crucial for optimising the server's thermal management and enhancing overall performance.
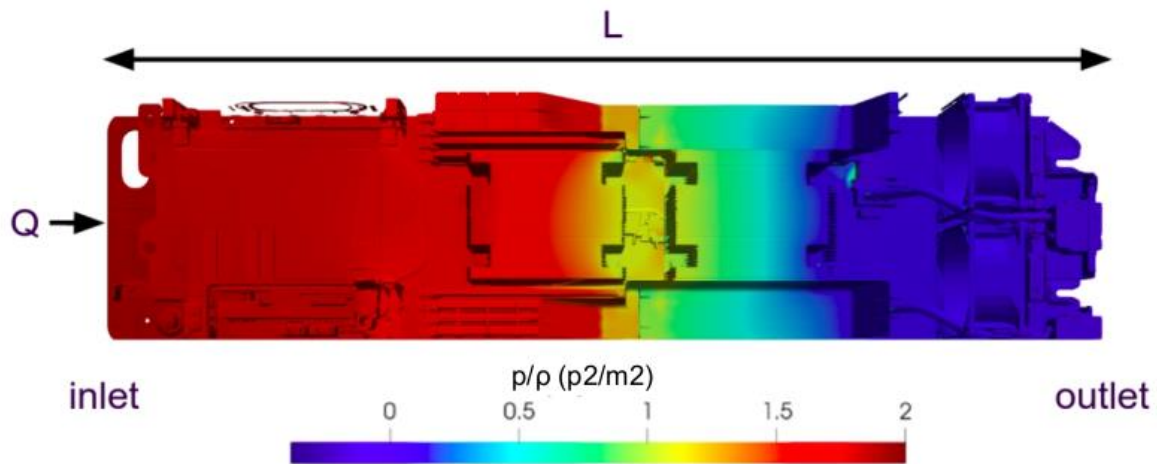
Figure 2.10: Pressure counters at the top plane of the server.

2.2.6. Development of a Porous Model for Data Centre Simulations

We conducted simulations for 20 different flow rates ranging between 0.003 and 0.06 m^3/s, during which we calculated the pressure differences resulting from each simulation. To replicate the observed pressure differences in the following stages, we intend to develop a porous zone approach. Reverse engineering was employed to determine the Darcy-Forchheimer coefficients [64] required to match the pressure difference values, and the derived coefficients have been presented in Table 2.3.

$$\nabla P = \frac{\Delta p}{\Delta L} = \mu D u_i + \frac{1}{2}\rho F u_i{}^2 \tag{10}$$

where L is the length of the porous zone and μ is the viscosity of the fluid. The pressure

drop can be approximated to the results obtained from the fully resolved three-dimensional simulations by choosing appropriate D and F coefficients [64]. where Darcy and Forchheimer coefficients, respectively.

A detailed plot has been generated based on the simulation results, illustrating the relationship between the pressure drop and flow velocity. The following plot serves as a visual representation of the data, allowing for a clear comparison of how the pressure drop varies with the flow velocity. A curve fitting process was performed using the obtained data, and R^2 value was calculated as 0.99, indicating a high accuracy. As a result, the D and F coefficients were calculated and listed in Table 2.3.
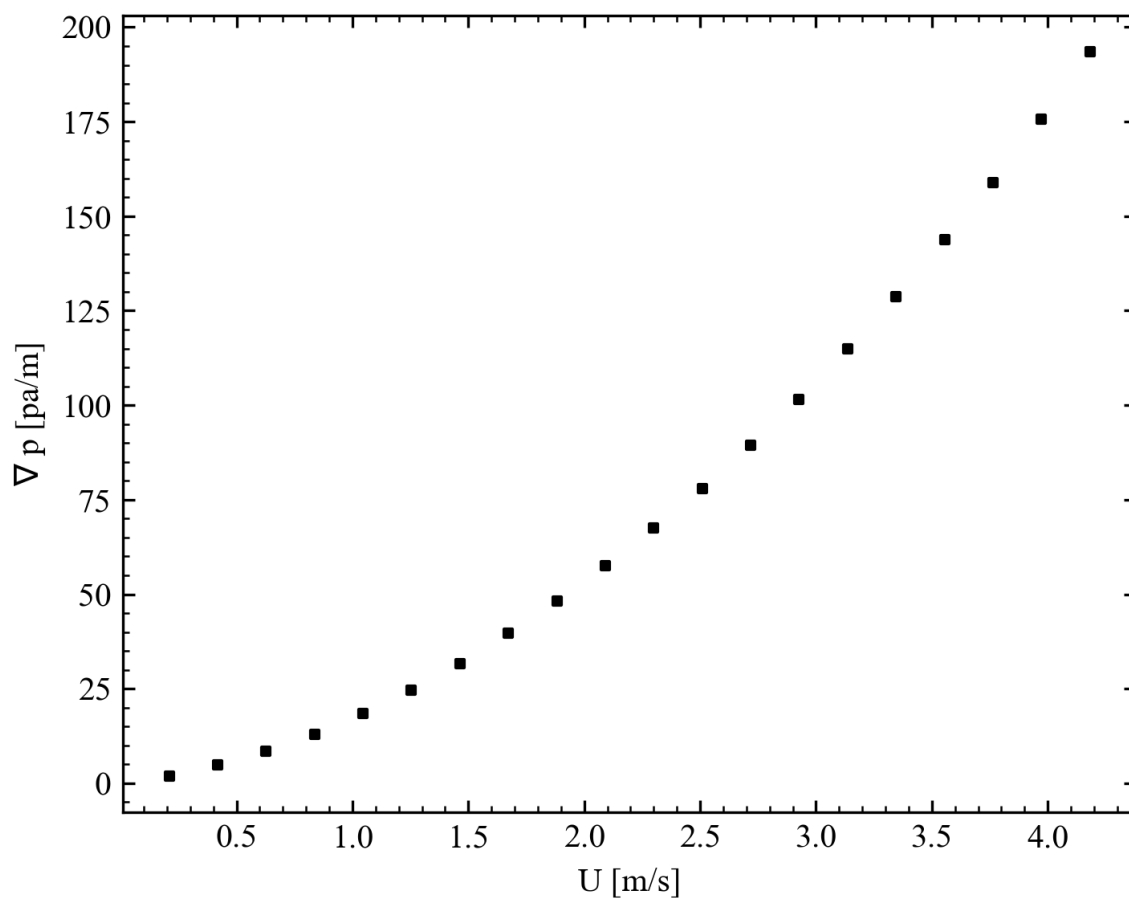

Figure 2.11: Variations of the pressure gradients with the inlet velocity from the full Navier-Stokes simulations.

Table 2.3: Darcy-Forchheimer coefficients.

D (1/m^2)	F (1/m)
5.62×10^5	18.02

The obtained coefficients were used to define a porous zone in the same location as the server, and a series of simulations were rerun. The results from the complete model and the porous zone approach were then compared in the following figure to assess their accuracy and performance under identical conditions. As can be clearly seen in the figure, the proposed porous approach can yield identical results with the full solution even on a coarser mesh.
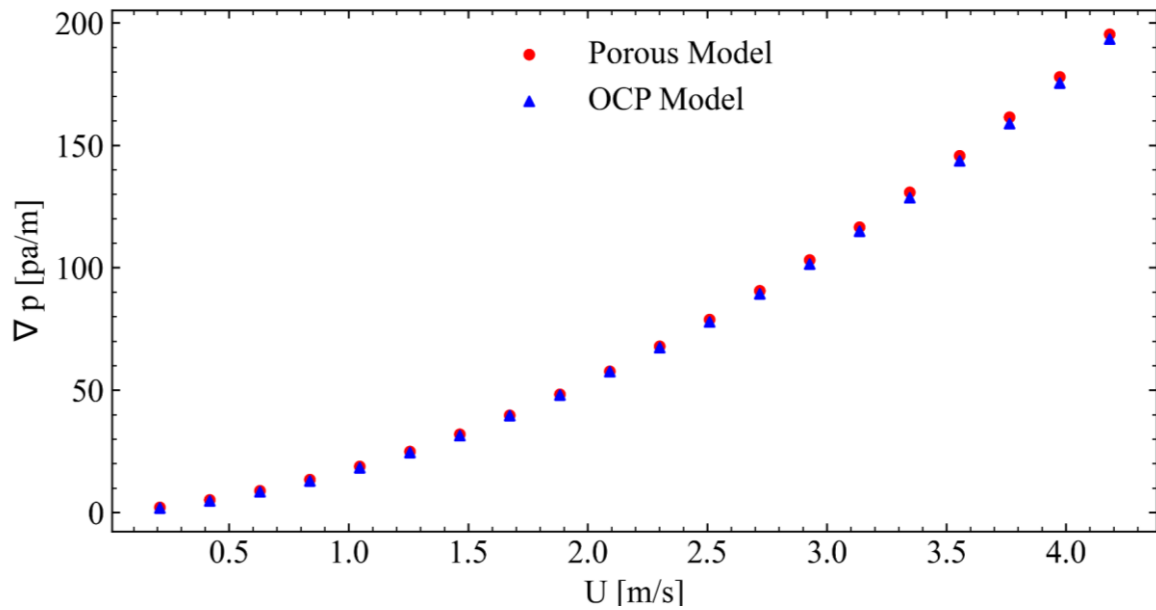

Figure 2.12: Comparison of pressure gradients predicted from full Navier-Stokes and porous simulations.

The uncertainty of the data can be estimated from the following uncertainty index (UI) [63]:

$$UI = \frac{\left| \Delta P_{complete} - \Delta P_{porous} \right|}{\Delta P_{complete}} \qquad (11)$$

where $\Delta P_{complate}$ and ΔP_{porous} are predicted pressure drops in complete and porous models, respectively. The UI is calculated for the tested flow rates and given in table for complete and porous model. The average UI is found to be 0.0258 when the OCP model and porous model are compared.

Table 2.4: Uncertainty indexes for complete and porous models.

Q (m³/s)	UI	Q (m³/s)	UI
0.003	0.1317	0.033	0.0079
0.006	0.0725	0.036	0.0137
0.009	0.0509	0.039	0.0143
0.012	0.0414	0.042	0.0172
0.015	0.0314	0.045	0.0149
0.018	0.0200	0.048	0.0167
0.021	0.0153	0.051	0.0142
0.024	0.0049	0.054	0.0165
0.027	0.0061	0.057	0.0142
0.03	0.0035	0.06	0.0101

2.2.7. Development of a Thermal Model for OCP Servers

In the previously developed OCP server model, a heat source was incorporated beneath the heatsinks to enhance heat distribution and determine thermal performance. A cellZone was designated in this region, and a semiImplicitSource representing a thermal design power of 100 W for Chip1 and Chip2 was applied through fvOptions. This case is solved with buoyantSimpleFoam in OpenFOAM[62]. This solver is a steady state solver that takes buoyant effects into account. The temperature on chip 2 is approximately around 360K, and the temperature distribution is higher than that of chip 1. The reason for this is that the heated air from the chip reaches chip 2. This situation is commonly encountered in air-cooled servers. This configuration enables a more detailed analysis of

the system's thermal behaviour, providing critical data for improving heat management and ensuring efficient cooling.
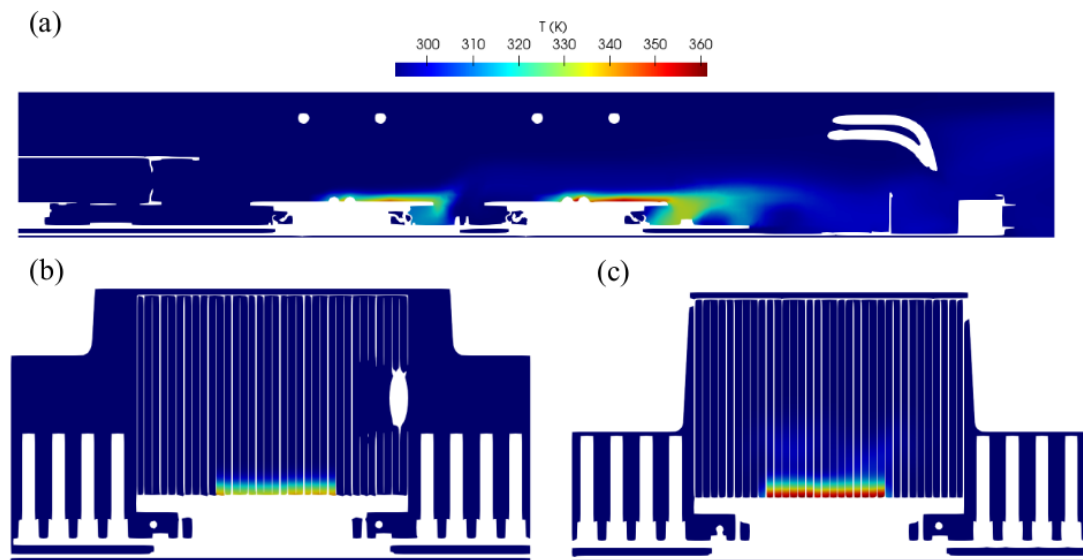

Figure 2.13: Temperature distribution on the a) along the server in a cross-section along the y-axis, b) heatsink of the first chip and c) of the second chip in a cross-section along the x-axis.

Following figure depicts variation of the average inlet and outlet temperatures with the iteration number. The solution converges to the steady-state solution after the iteration number of 1800.
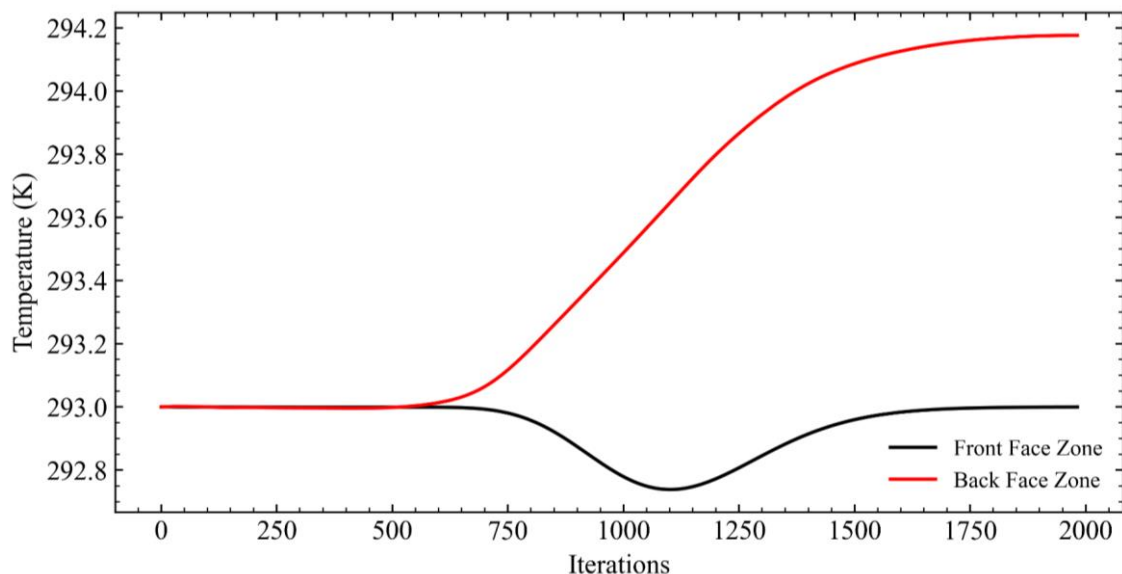
Figure 2.14: Iteration-dependent temperature distribution graph on the inlet and outlet face zones.

2.3. Numerical Modelling of the Cooling System

The cooling units in data centres are modelled as patches since they serve as surfaces where air enters and exits. The surfaces supplying cold air to the data centre function as inlets, while the surfaces where the heated air leaves the system operate as outlets. Therefore, the same logic is applied during the modelling process. The following figure shows definitions of supply and return patches from the cooling units inside the PSNC micro data centre.
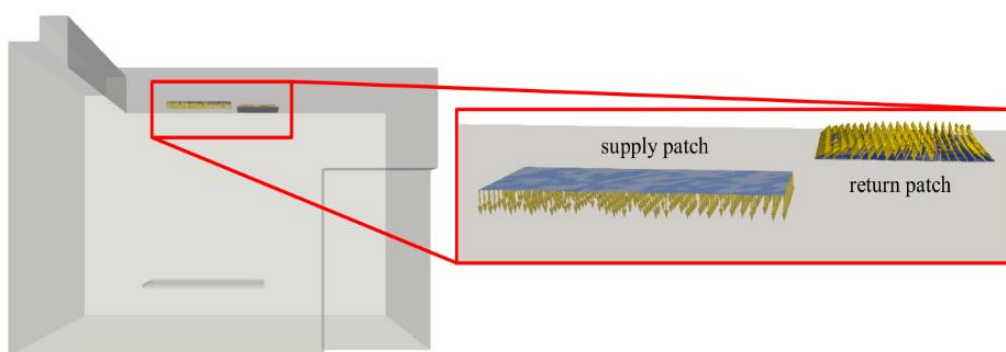

Figure 2.15: Modelling faces of the cooling unit using patches.

As seen in the figure, the air flows toward the data centre through the supply patch, providing cooled air. In contrast, the return patch discharges the heated air from the data

centre. Since these surfaces are modelled as inlets and outlets, as can be seen in the following figure, they function as boundary conditions in the solver.

Figure 2.16: Definitions of the boundary conditions for the cooling unit: a) velocity and b) temperature.

In the supply patches, the operational flow rate and temperature values supplied to the


```
(a)

hvac_1_return
{
    type            inletOutlet;
    inletValue      uniform (0 0 0);
    value           uniform (0 0 0);
}

hvac_1_supply
{

    type                flowRateInletVelocity;
    volumetricFlowRate  constant 0.5;
}
```

```
(b)

hvac_1_return
{
    type            zeroGradient;
}

hvac_1_supply
{
    type            fixedValue;
    value           uniform 288.28;
}
```

data centre are implemented, while in the return patch, no direct intervention is made for the velocity, using the inletOutlet condition, and for the temperature, the zeroGradient condition is applied. The resulting dynamics are left entirely to the solver, allowing observation of the outcomes. In the Empa centre, however, the cooling units use coils, which results in a completely different modelling approach. This phenomenon is explained in detail in the following sections.

2.4. Open-Source CFD Model for Data Centres: dataCenterDST

The dataCenterDST is a framework system developed using Python code to automate the modelling of data centres. When performing a model in this system, two critical inputs are required: the layout file and the settings file. The layout file defines key parameters such as which cabinet contains the servers, the starting position in the cabinet, the height in U units, power consumption, and flow rate values.

The settings file is divided into three main sections. Under the "Conditions" section, the properties to be implemented for rack cabinets, active and inactive IT equipment, and the CRAC unit are specified. In the "meshSettings" section, the boundaries and grid numbers related to blockMesh are provided, which are later used in mathematical calculations to create the topoSet. In the "rackSettings" section, the starting corner coordinates of the

rack cabinets, the U height for a shelf, the cabinet dimensions, and the airflow direction through the server are specified. These data are also used in the mathematical calculations of the components to be created and to determine the direction of the resources to be supplied.

(a)

Rack	First Row	Height	Type	Model	pwrConsumption	Q	rpm	condition	CoolingType
1	1	1	empty		0	0	0	null	A
1	2	7	ITEquipment		0	0	0	null	A
1	9	1	empty		0	0	0	null	A
1	10	1	ITEquipment		0	0	0	null	A
1	11	1	empty		0	0	0	null	A
1	12	2	ITEquipment	R7525_1	304.4	0.05	0	null	A
1	14	2	ITEquipment	R7525_2	124.18	0.05	0	null	A
1	16	6	empty		0	0	0	null	A
1	22	1	emptyClosed		0	0	0	null	A
1	23	2	ITEquipment	RH228H_V3_1	308.07	0.04	0	null	A
1	25	4	ITEquipment	X6800_1	968.96	0.1	0	null	A
1	29	1	empty		0	0	0	null	A
1	30	1	empty		0	0	0	null	A
1	31	4	ITEquipment	X6800_2	982.51	0.13	0	null	A
1	35	2	ITEquipment	RH2288H_V3_2	321.04	0.05	0	null	A
1	37	6	empty		0	0	0	null	A
2	1	6	empty		0	0	0	null	A
2	7	1	emptyClosed		0	0	0	null	A
2	8	6	empty		0	0	0	null	A
2	14	1	emptyClosed		0	0	0	null	A
2	15	4	empty		0	0	0	null	A
2	19	1	empty		0	0	0	null	A
3	1	2	ITEquipment	Arneb	668.4	0.04	0	null	A
4	1	1	empty		0	0	0	null	A
4	2	2	ITEquipment	HN	136.74	0.02	0	null	A
4	4	1	emptyClosed		0	0	0	null	A
4	5	3	ITEquipment		0	0	0	null	A
4	8	1	emptyClosed		0	0	0	null	A
4	9	3	ITEquipment		0	0	0	null	A
4	12	1	empty		0	0	0	null	A
4	13	2	ITEquipment	R760XD2	265.3	0.03	0	null	A
4	15	4	empty		0	0	0	null	A
4	19	2	emptyClosed		0	0	0	null	A
4	20	1	ITEquipment		0	0	0	null	A
4	21	1	emptyClosed		0	0	0	null	A
4	22	1	ITEquipment		0	0	0	null	A
4	23	1	empty		0	0	0	null	A
4	24	2	ITEquipment		0	0	0	null	A

(b)

```
#------------------------------------------
#
#       ___  __   ___ ___  ___   __   _   _
#      |   \/ __||_   _|| __| / __| | | | |
#      | |) |\__ \  | |  | _| | (__  | |_| |
#      |___/ |___/  |_|  |___| \___|  \___/
#
#------------------------------------------

settings
{
    conditions
    {
        rack                rightLeftTopWallsCreateBaffleTs;
        ITEquip             bottomWallCreateBaffleTs;
        activeITEquip       (momentumSourceTs heatSourceTsMp porosityTs);
        inactiveITEquip     porosityTs;
        emptyClosedITEquip  removeVolumeTs;
        CRACUnit            null;
    }

    meshSettings
    {
        min (0 0 0);
        length (4.86 4.1 3.5);
        nGrids (151 123 105);
    }

    rackSettings
    {
        rack1
        {
            U       0.04645;
            coord   (1.4 1.95 0);
            height  42;
            width   0.6;
            length  1.18;
            flowDir (0 1 0);
        }
```

Figure 2.17: Implementation of the server layout in the dataCenterDST: a) Input file and b) code.

The code snippet below represents the porosityTs condition, which is one of the conditions defined within the settings file. Frequently used conditions have been prepared and named to apply the desired properties to multiple elements and reuse them. In the provided condition, Darcy-Forchheimer coefficients are calculated based on the parameters of the server and then assigned to the servers as a porous zone.

```
#-------------------------------------------------
#
#          ____  _____ _____ _____  ____  _   _
#         |  _ \/ ____|_   _|  ___|/ ___|| | | |
#         | | | (___   | | | |__  | |    | |_| |
#         | | |\___ \  | | |  __| | |    |  _  |
#         | |_|___) |  | | | |___ | |___ | | | |
#         |____/____/   |_| |_____| \____||_| |_|
#
#-------------------------------------------------

from dc.settings import settings
from dc.write.createFunctions import *

def porosityTs(i):
    i.topoSet = True
    i.midPart = False
    p = 0.5
    A = i.area()
    width = i.width
    height = i.height
    C = (width+height)*2
    dH = (4*A)/C
    d = (120*(1-p)**2)/((p**3)*(dH**2))
    f = (2.3*(1-p))/((p**3)*(dH))
    boundBox = i.boundBox()
    createPorosZone(i.name(), boundBox, d, f)
    return
```

Figure 2.18: Definition of porosity parameters in the dataCenterDST.

Within the class structure created for the server properties, many parameters are defined. These parameters can be used to generate custom conditions tailored to specific needs.

```python
class ITEquipment(DCObject):
    def __init__(self, coords, data, rack):
        self.minCoords = coords
        self.data=data
        self.rack = rack
        self.flowDir = rack.flowDir
        self.length = rack.length
        self.width = rack.width
        self.height = self.heightM()
        self.calcCoords(self.height)
    def type(self):
        return self.data.type
    def model(self):
        return self.data.model
    def name(self):
        return self.data.name
    def pwrConsumption(self):
        return self.data.pwrConsumption
    def fanRpm(self):
        return self.data.fanRpm
    def condition(self):
        return self.data.condition
    def Q(self):
        return self.data.Q
    def heightU(self):
        return self.data.height
    def empty(self):
        return self.type() == 'empty'
    def emptyClosed(self):
        return self.type() == 'emptyClosed'
    def active(self):
        return self.Q() != 0
    def inactive(self):
        return self.Q() == 0 and not(self.empty() or self.emptyClosed())
    def bottomIT(self):
        return self.data.firstRow == 1
    def topIT(self):
        return self.data.firstRow + self.height() == self.rack.height
    def heightM(self):
        return self.heightU()*self.rack.U
    def meanVelocity(self):
        velocity = self.Q()/self.area()
        return velocity*self.rack.flowDir
```

Figure 2.19: Definition of the class structure for the IT Equipment.

Once the desired properties are defined in the settings file, the dataCenterDST generates include files to be used in the mesh and case files. Two of the include files created for use in the mesh are topoSetInclude and createBafflesInclude, which will be examined in detail.

createBaffl
eDictInclud
e

topoSetDict
Include
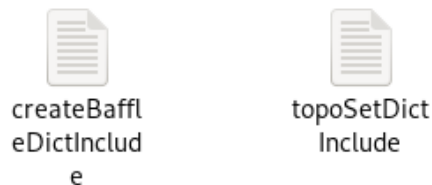
Figure 2.20: Files created by the dataCenterDST to define baffles in the geometrical model.

The topoSetInclude file is used to define the regions or sets within the mesh that are relevant to the simulation. It creates zones for specific parts of the data centre, such as rack cabinets or IT equipment, based on the layout and settings provided. These zones are then used to apply specific conditions, such as porous zones or boundary conditions. createBafflesInclude file is responsible for defining the creation of baffles within the mesh. Baffles are physical barriers or flow-guiding elements that can be added to control the airflow within the data centre. The createBafflesInclude file specifies their location, size, and characteristics, which are then incorporated into the final mesh for the simulation. These files are essential for automating the preparation of the mesh.

By reading the coordinates provided in the settings file and the parameters obtained from the layout file, the required coordinates for the server walls are determined. These coordinates are then written to the topoSetInclude file. This process automates the definition of specific regions within the mesh that correspond to the server walls

```
{
    name    rack1fr2BottomWallfaceSet;
    type    faceSet;
    action  new;
    source  boxToFace;
    sourceInfo
    {
        box (1.38075497 1.93      0.03     ) (1.99871523 3.13666667 0.03666667) ;
    }
}

{
    name    rack1fr9BottomWallfaceSet;
    type    faceSet;
    action  new;
    source  boxToFace;
    sourceInfo
    {
        box (1.38075497 1.93      0.36333333) (1.99871523 3.13666667 0.37      ) ;
    }
}
```

Figure 2.21: Definition of a faceSet in the dataCenterDST.

Additionally, to define sources like porousZone, heatSource, and momentumSource later, the cellSets within the servers are automatically calculated and generated by dataCenterDST. This ensures that the regions inside the servers where these sources need to be applied are accurately identified. Based on the layout and settings data, dataCenterDST calculates the relevant cellSets that correspond to areas within the server volumes.

```
{
    name    rack1fr2CellSet;
    type    cellSet;
    action  new;
    source  boxToCell;
    sourceInfo
    {
        box (1.38075497 1.93      0.03     ) (1.99871523 3.13666667 0.37      ) ;
    }
}
```

Figure 2.22: Definition of a cellSet in the dataCenterDST.

The names of the sets created by topoSet are automatically written to the createBafflesInclude file as well. This ensures that the sets generated by topoSet are transformed into baffles.

```
rack1fr2BottomWallfaceZone
{
    type        faceZone;
    zoneName    rack1fr2BottomWallfaceZone;

    patches
    {
        master
        {
            name    rack1fr2BottomWall;
            type    wall;
        }
        slave
        {
            ${..master}
        }
    }
}
```

Figure 2.23: Definition of a baffle dataCenterDST.

By automating this process, dataCenterDST identifies the regions defined by topoSet and converts them into physical baffles in the mesh. These baffles can influence airflow by acting as barriers or flow-guiding elements. The automated inclusion of these set names in the createBafflesInclude file ensures consistency and accuracy, allowing the baffles to be effectively integrated into the simulation model. A visual representation of a sample mesh created using dataCenterDST is provided below.
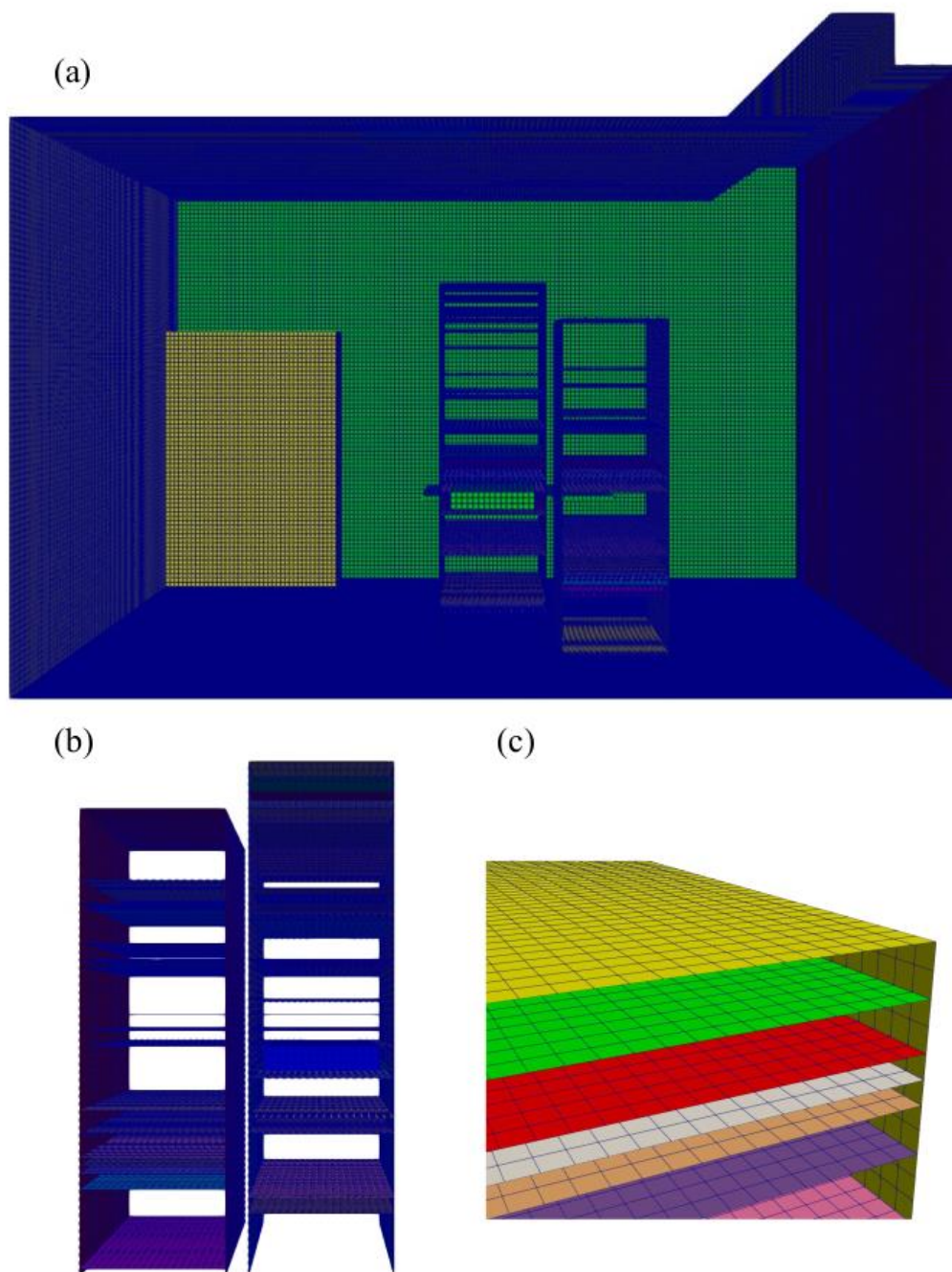
Figure 2.24 Generation of the three-dimensional model and mesh by the dataCenterDST a) Front view of the data centre, b) rack cabinets and c) zoom into the rack cabinets.

While dataCenterDST helps create auxiliary files for the mesh structure, it also generates include files to implement the conditions specified in the settings file within the case. To ensure that the expected files are included, it is necessary to specify them within the fvOptions file. The fvOptions file is essential for managing additional physical models and source terms in OpenFOAM simulations. By detailing the required include files in this section, dataCenterDST allows the simulation to recognize and utilise the specified conditions, such as porousZone, heatSource, and other defined properties.
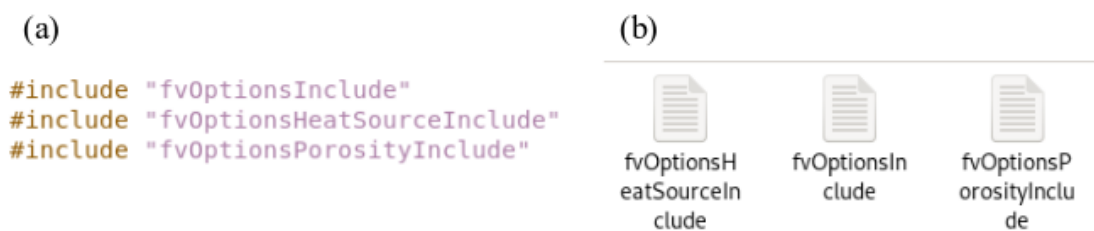
Figure 2.25: Views of the a) fvOptions and b) include files in the dataCenterDST.

The contents of the provided include files contain the power consumption and flow rate values specified in the layout file, which are supplied to the servers. Similarly, the porousZone property outlined in the settings is implemented for each server in the same manner.

(a)

```
rack1fr2
{
    type                explicitPorositySource;

    explicitPorositySourceCoeffs
    {
        selectionMode   cellZone;
        cellZone        rack1fr2CellZone;

        type            DarcyForchheimer;

        D 1235.9252936023677;
        F 20.87749155295646;

        d   ($D $D $D);
        f   ($F $F $F);

        coordinateSystem
        {
            type    cartesian;
            origin  (0 0 0);
            coordinateRotation
            {
                type    axesRotation;
                e1  (1 0 0);
                e2  (0 1 0);
            }
        }
    }
}
```

(b)

```
rack1fr12MomentumSource
{
    type                vectorFixedValueConstraint;
    active              yes;

    selectionMode   cellZone;
    cellZone        rack1fr12CellZone;
    fieldValues
    {
        U               (0.        0.8176305 0.        );
    }
}
```

(c)

```
rack1fr12midBoxHeatSource
{
    type      semiImplicitSource;
    active    true;
    timeStart   0;
    duration    20000;
    selectionMode    cellZone;
    cellZone    rack1fr12midBoxCellZone;
    volumeMode   specific;
    sources
    {
        h
        {
            explicit    21333.147684024898;
            implicit    0;
        }
    }
}
```

Figure 2.26: Definitions of a) porous zone, b) momentum source and c) heat source in the dataCenterDST.

All the case and mesh files corresponding to the specified properties are automatically generated by the dataCenterDST. Whether these files will be used and the order of their usage is left to the user, who must prepare the Allrun and Allmesh scripts according to their specific needs. By preparing these scripts, it becomes possible to create the mesh and case for the data centre and run the simulation effectively. The flexibility in customising the scripts allows users to tailor the simulation process to meet their particular requirements, ensuring that the modelling and analysis are both efficient and relevant to their objectives.

2.5. Validation of the Numerical Model at Empa Data Centre

The validation of a CFD model using experimental data is crucial for ensuring its accuracy and reliability. While CFD simulations offer detailed insights into complex fluid dynamics and heat transfer phenomena, they are based on mathematical approximations and assumptions. Comparing the simulation results with experimental data provides a benchmark to assess how closely the model reflects real-world behaviour. This process helps identify any discrepancies and refine the model, improving its predictive capability. By aligning CFD results with experimental observations, engineers can confidently use the model for design optimization, troubleshooting, and decision-making, knowing that it accurately represents the physical system.

Empa, the Swiss Federal Laboratories for Materials Science and Technology[65], is an interdisciplinary research institute within the ETH Domain. Their cutting-edge research focuses on developing innovative materials and technologies that meet industry requirements and societal needs.
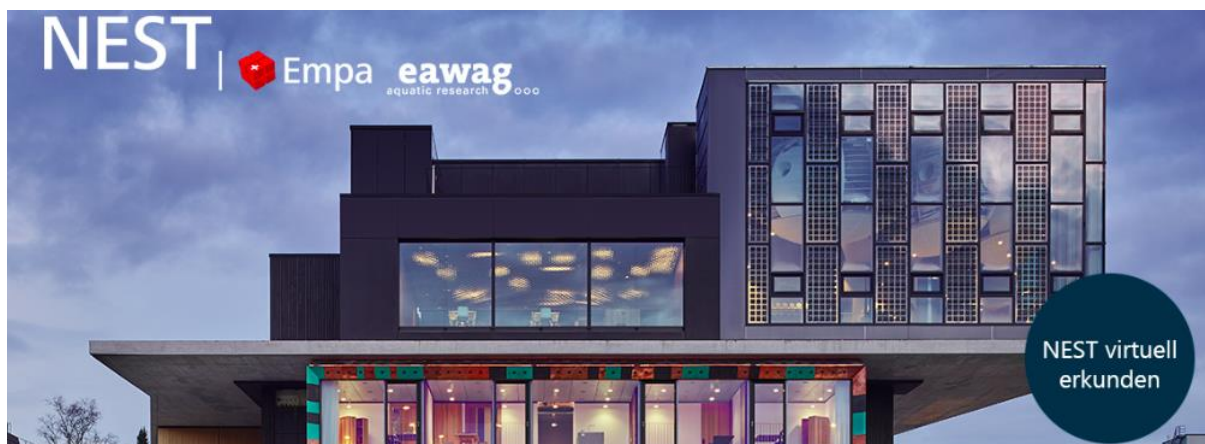
Figure 2.27: Snapshot of the EMPA nest.

Empa DC[65] is a micro data centre structure focused on energy efficiency and environmental sustainability. In Empa DC, IT equipment such as servers, power shelves, and switches are housed in rack cabinets. The cooling system is designed to efficiently cool these components using water coils and fans. Unlike traditional data centres that consume a lot of energy, the cooling unit in Empa's data centre plays a crucial role in energy conservation. As air flows through the water coils, it absorbs heat and cools down, but the energy transferred to the coils is not wasted. Instead, this waste energy is

repurposed to heat the building, thanks to the integration of the data centre with the surrounding structure. Figure 2.28 a illustrates the cooling unit and rack cabinet setup in Empa DC.

The OCP (Open Compute Project) servers located within the rack cabinet are one-third the width of a rack. The servers are positioned on the right and left sides of the cabinet shelves, and the remaining central space is closed off to prevent obstruction of airflow. The layout plan of the servers is provided in Figure 2.28 b.
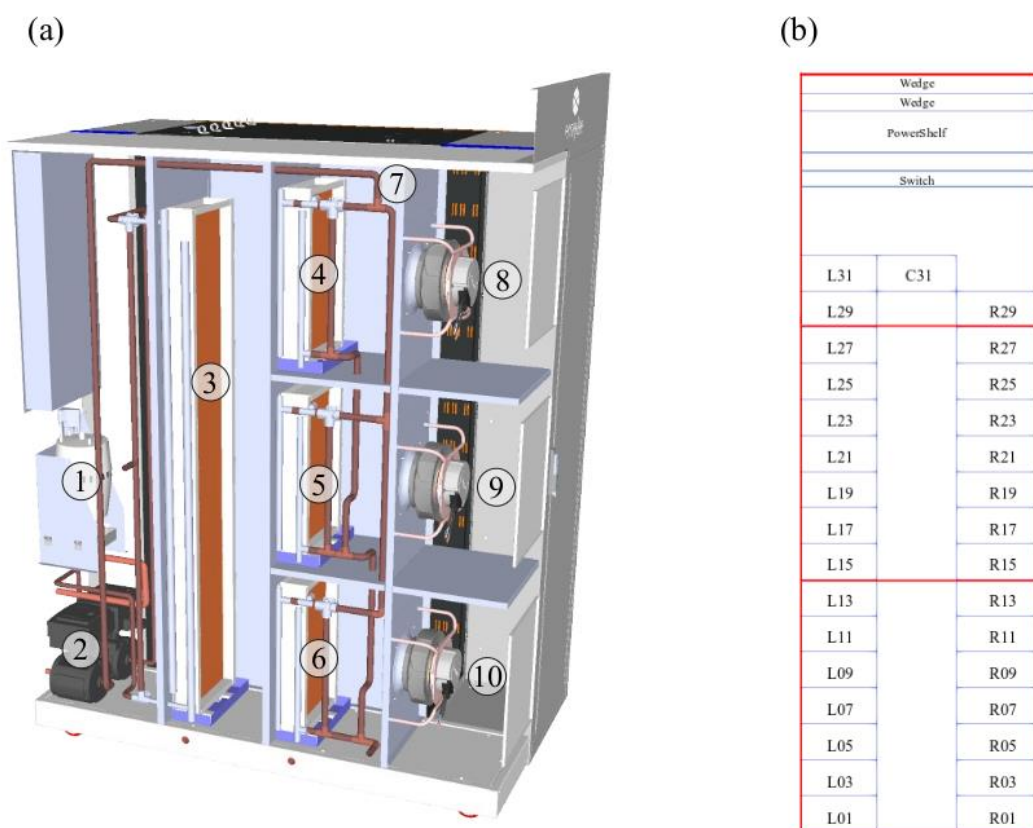
Figure 2.28: a) Cooling unit and b) rack layout at the Empa data centres.

Table 2.5: Components of the cooling unit.

Component	Description
1	Humidifier
2	Low and medium temperature grid pumps
3	MTG
4, 5, 6	LTG
7	Valve
8, 9, 10	Fans

The components MTG (medium temperature grid) and LTG (low temperature grid) in Figure 2.28 are the water coils responsible for cooling within the data centre. As the air heated by the servers passes through these water coils, it releases its energy, resulting in cooled air. Cooled air is then circulated back to the server inlets with cooling unit fans. LTG consists of three water coils. The total water flow entering these coils is the same as the water flow passing through the 3-way valve. This water flow from the three-way valve is distributed among the three coils. Meanwhile, the heated air is collected in a single pipe before exiting the system. The water heated in LTG is sent to the chiller again to be cooled. This means that the cooling load in the chiller is due to the hot water coming from LTG. The water heated in MTG, on the other hand, is referred to as waste heat and provides heat recovery.

The computational mesh is created using a combination of open-source software and utilities such as GMSH, Python, and snappyHexMesh. This mesh is prepared as a hexahedral mesh utilising the parallel computation utility snappyHexMesh. Stereolithography (STL) files contain the geometry of the data centre and its structural components, including server fans, separators between server fans, racks, interior walls, objects (low-temperature grid pump and medium-temperature grid pump), and cooling units. The cooling properties of the low-temperature and medium-temperature grids were not accounted for in the analysis. Instead, these components were modelled as porous zones to represent the alterations they induce in the flow dynamics. The hex-

dominant mesh generation algorithm in snappyHexMesh is used to snap internal solid objects, producing a high-quality mesh with maximum allowable skewness and non-orthogonality. Details of the computational mesh configurations are provided in Table 2.6.
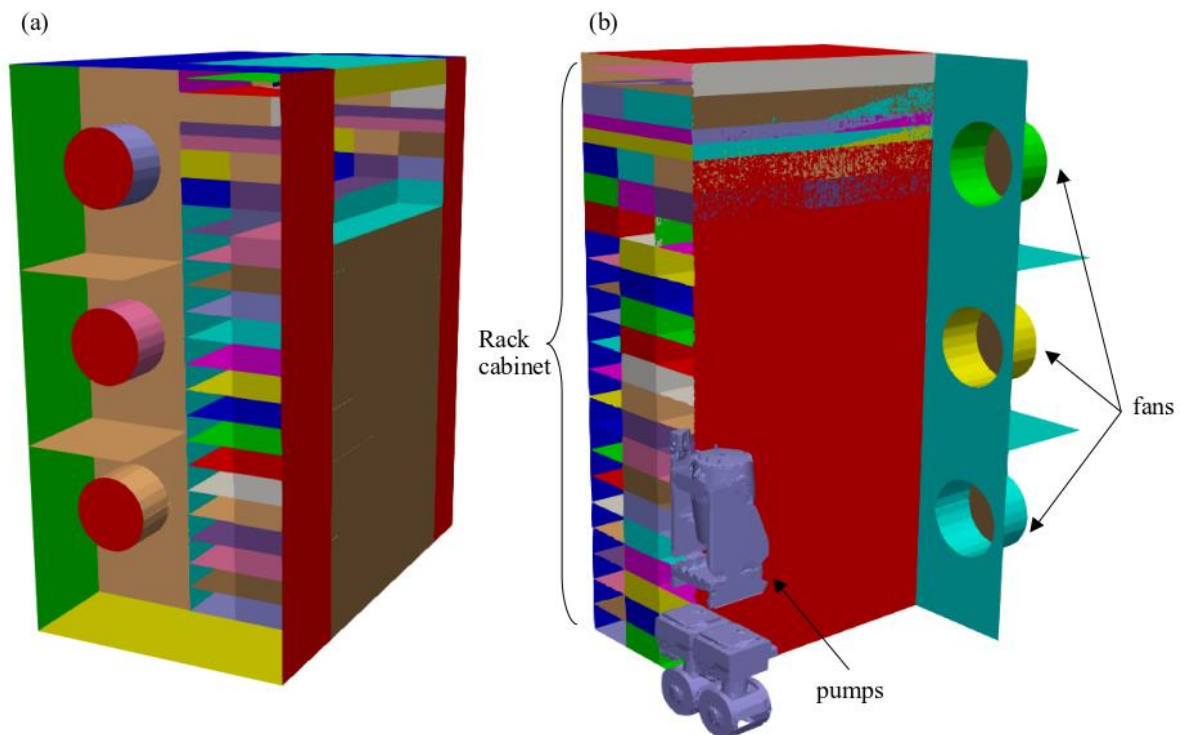
Figure 2.29: CFD mode of the Empa data centre generated by the dataCenterDST.

Table 2.6: Mesh statistics of the CFD model for Empa Data Centre.

Number of Cells (Million)	Maximum Skewness	Minimum Volume	Maximum Volume
2.2	18.07	2.25e-09	6.07e-06

Our numerical model utilises the solution of steady-state Reynolds-Averaged Navier-Stokes (RANS) equations to simulate fluid flow. This simulation incorporates turbulent flow with buoyancy effects and is conducted using DataCenterDST©, an open-source software based on OpenFoam specifically developed for modelling data centres. In our

approach, the convective terms are discretized using a first-order accurate upwind scheme, while the divergence terms are handled with a more precise second-order accurate Gauss linear scheme. The coefficients resulting from the discretization of the governing equations are solved using the Generalised Preconditioned Biconjugate Gradient (PBiCGStab) algorithm and stored in matrices for further analysis.

For validation study, we employed the buoyantSimpleFoam solver to ensure the accuracy and reliability of our results. buoyantSimpleFoam is used for stable solutions based on the SIMPLE (Semi-Implicit Method for Pressure-Linked Equations) algorithm, with a relaxation factor set to 0.3 for each field. To reduce the computational cost associated with long-term solutions, a function object has been added to the OpenFoam library. This object controls the residuals and terminates the steady-state solution if the residual slope falls below 0.05 in certain fields.

2.5.1. Validation of the CFD Model with the IPMI Data

To validate our numerical model driven by fan data, we compared it with IPMI (Intelligent Platform Management Interface) data, focusing specifically on outlet temperatures. The fans in our setup operated at a speed of 500 rpm, with each fan constantly supplying air at a temperature of 24 °C. We recorded the outlet temperatures using the Prometheus data monitoring system. For the CFD model, we selected power consumption values of 295 W for 8 servers in the data centre. The running servers were L1, L9, L15, L23, R1, R9, R15, and R23, while the other servers were idle with a power consumption of 69 W. The validation results are shown in Fig. 2.30.
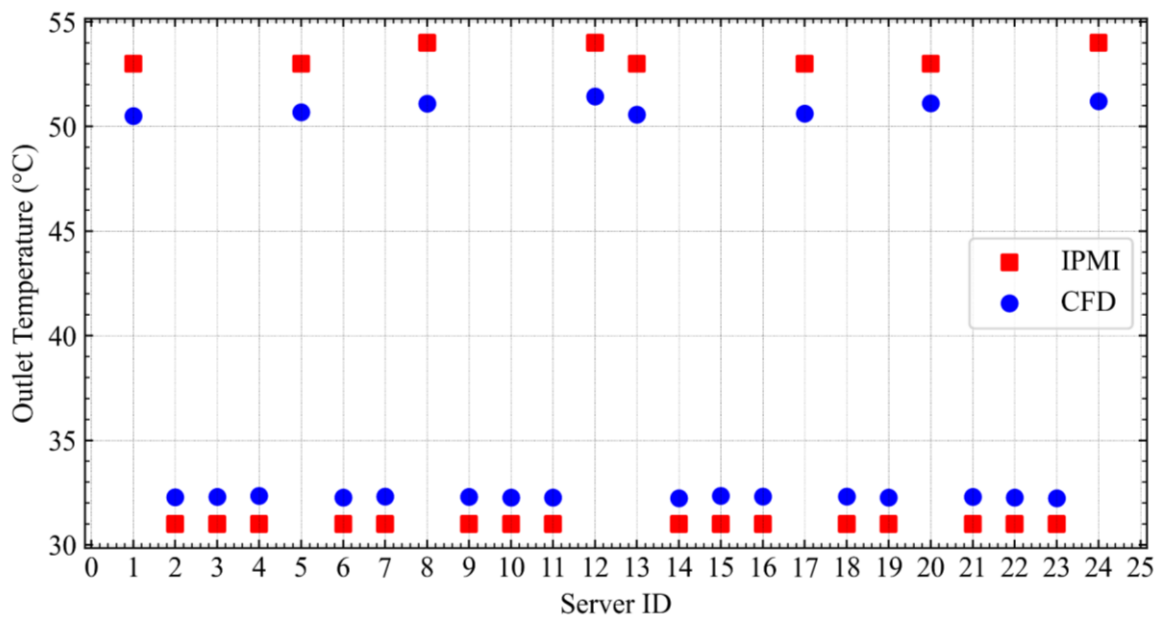
Figure 2.30: Validation of the numerical model with the IPMI data for Empa data centre.

In comparing the IPMI and CFD results for outlet temperature, maximum and average errors were calculated as 2.92 °C and 1.69 °C, respectively.

2.5.2. CHT Modelling of Empa Data Centre

Numerical simulations were performed using OpenFOAM-v2312 [62]. This software applies a finite volume approach to discretize the governing equations within a control volume. The simulations utilised the PIMPLE algorithm, which combines aspects of the PISO (Pressure Implicit with Splitting of Operator) and SIMPLE (Semi-Implicit Method for Pressure-Linked Equations) algorithms. This combination allows the PIMPLE algorithm to couple velocity and pressure in a pressure-based manner.

In the air region, convective terms were discretized with bounded Gauss upwind schemes. The gradient terms used Gauss linear schemes. Laplacian terms were handled using a limited corrected Gauss linear method with a limiting coefficient of 0.33. For the water region, convective terms were also discretized using bounded Gauss upwind schemes. However, the gradient terms used Gauss linear schemes, and the Laplacian terms were handled with a Gauss linear uncorrected scheme. Matrix solutions for both regions were obtained using GAMG and PBiCGStab solvers.

The numerical mesh consisted of two distinct regions: air and water. The interiors of the coils, filled with water, were designated as the water region. This water region mesh was prepared using blockMesh. The computational mesh for the air region was created using the snappyHexMesh utility. This utility used both hexahedral and split-hexahedral meshing techniques and was run in parallel computing mode. The mesh included the entire geometry of the data centre. This encompassed internal elements such as racks, fans, and a humidifier. The rack cabinets and servers for the data centre have been positioned and meshed using dataCenterDST©. A multi-region mesh was created by combining this model with a prepared mesh for the low temperature grid. The low temperature grid is designated as the water region. Porous zones have been defined across the entire domain of the low temperature grid, with these specifications determined based on velocity and pressure drop data provided by the manufacturer. An advanced hex-dominant meshing algorithm was applied to snap the internal solid objects, ensuring a high-quality mesh. This approach minimised skewness and non-orthogonality. Figure 2.31 is a visual representation of the mesh along with a statistical table detailing its properties.
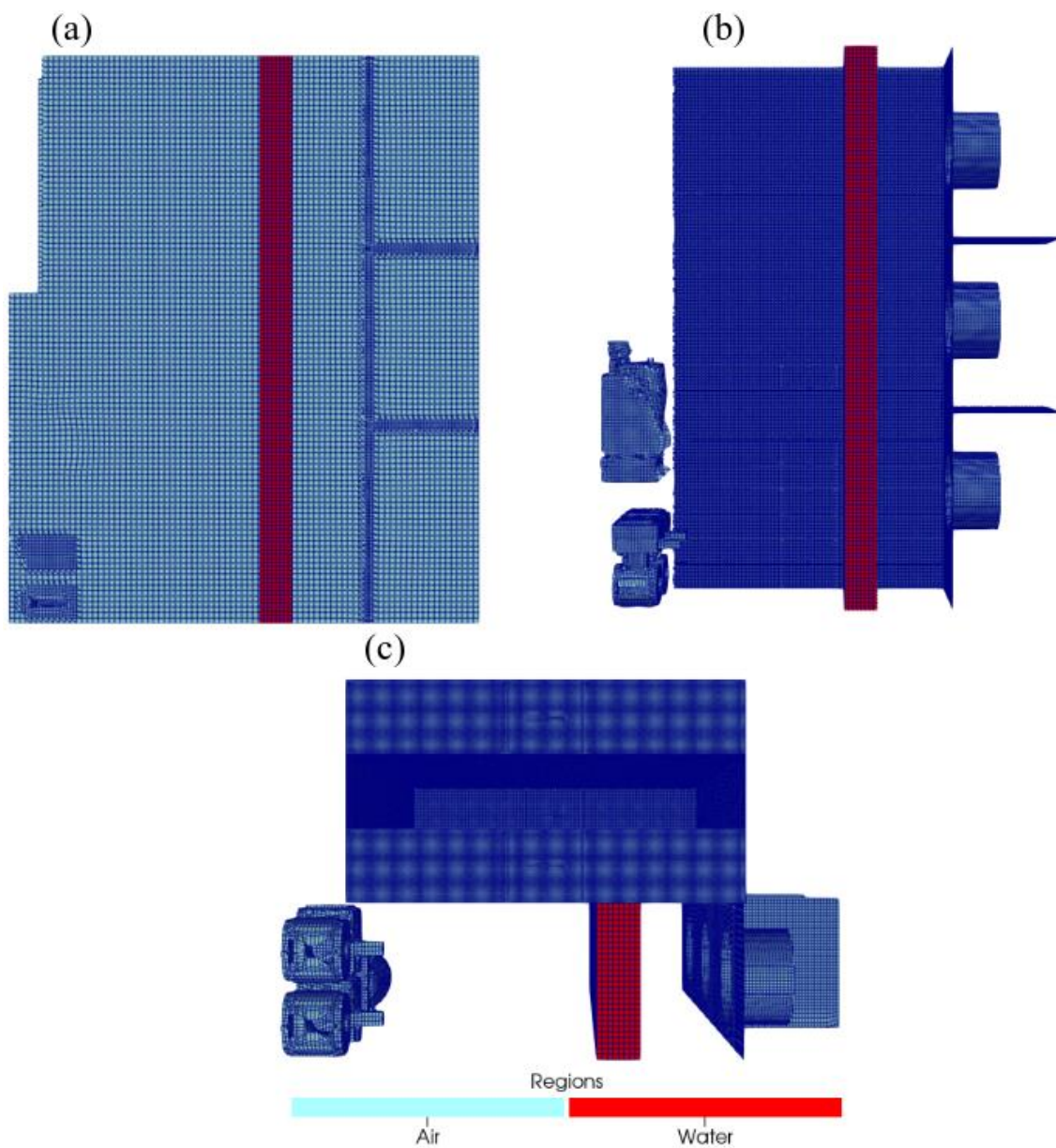
Figure 2.31: Views of the mesh for Empa Data Centre generated by dataCenterDST: a) Right view of the internal mesh, b) right view of the internal components and c) top view of the internal components.

Table 2.7: Mesh statistics of the Empa CHT model.

Region	Number of Cells	Maximum Skewness	Minimum Volume	Maximum Volume
Air	3,150,557	8.42	2.09e-08	1.35e-05
Water	31,136	1.20e-13	3.27e-06	3.28e-06

2.5.3. Validation of the CHT Model with the IPMI Data

As a result of the experimental studies conducted at the Empa data centre, the relationship between the water flow rate passing through the grids and the valve opening ratio (VOR) has been determined. Additionally, the relationship between the air flow rate provided by the cooling unit's fans and the inverter fan speed (IFS), as well as the impact of these two parameters on the cooling dynamics of the data centre, are known. The heated air inside the rack cabinet transfers its energy to the water as it passes through the cooling coils, thereby cooling down. The cooled air is then supplied to the server inlets via the cooling unit's fans.

Since the low-temperature grid has now been incorporated into the model as a water region, the operational parameters of this grid have gained significance. In the CFD model, the supply temperature of the cooling unit was previously taken as equal to its operational value and considered constant. With the implementation of conjugate heat transfer modelling, the flow and thermal structure within the data centre have been represented more accurately.

In this study, the aim was to assess whether the created numerical model accurately mimics the physical conditions within the data centre. To achieve this goal, parameters from experimental studies were integrated into the CHT model, and simulations were conducted accordingly. The results obtained from the CHT simulations were compared with the experimental data.

2.5.3.1. Validation Case-1

In the experimental study, servers L7, L13, L21, R7, R13, and R21 operate with 56 cores each. The layout of the working scenario is provided below:
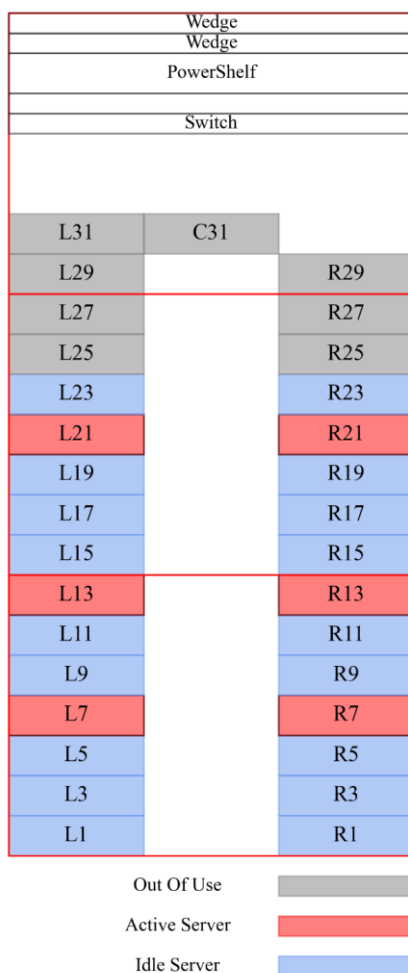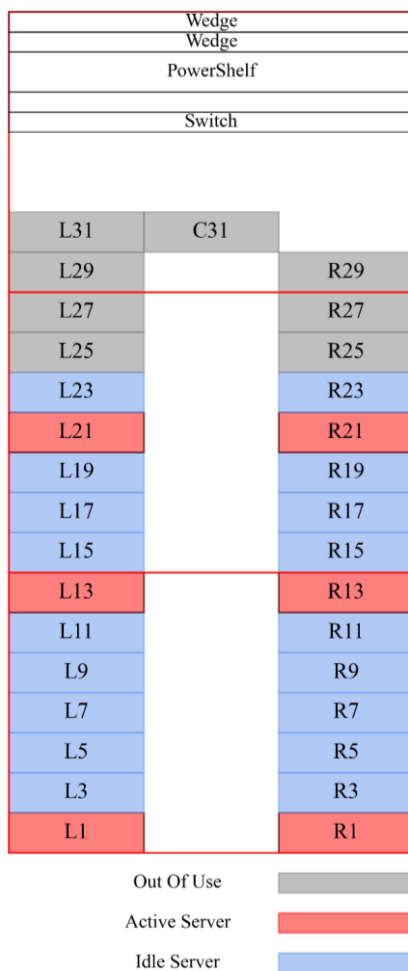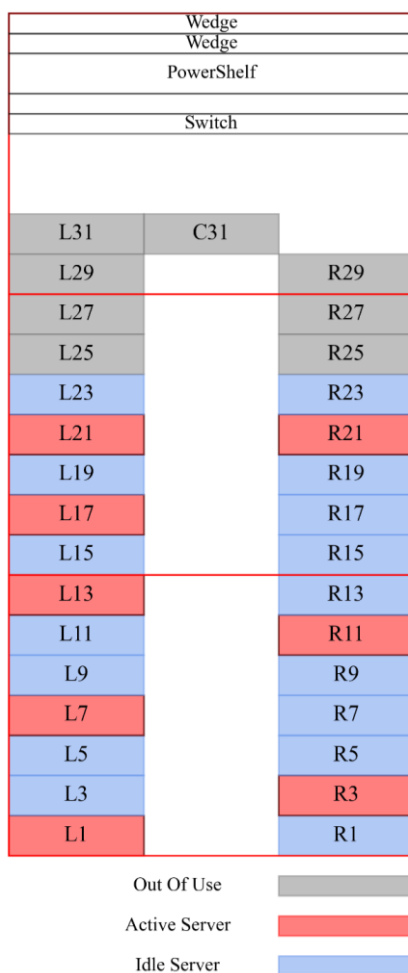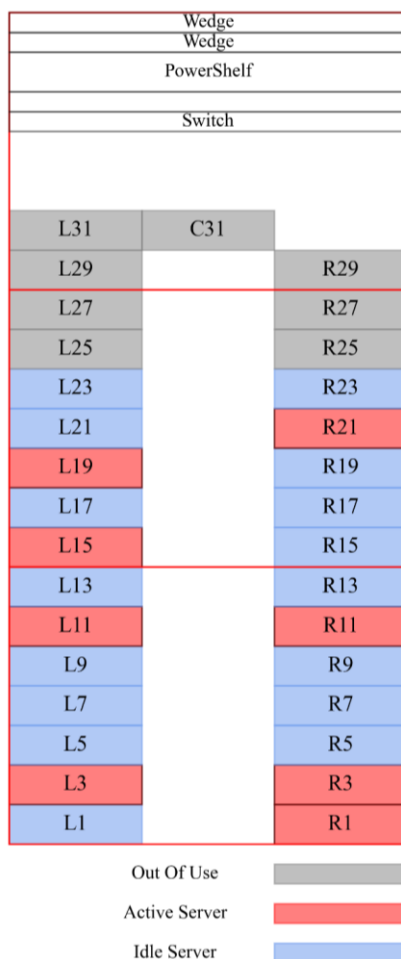
Figure 2.32: Layout for Case-1.

The parameters used as inputs in the CFD model and obtained from the experimental study are presented in Table 2.8.

Table 2.8: Input parameters for Case-1.

Water Inlet Temperature (°C)	VOR (%)	IFS (%)
11.1	55	30

The data obtained from simulations has been recorded and compared with experimental data. The information regarding the results is presented in Table 2.9.

Table 2.9: Comparison of simulated and measured data for Validation Case-1.

	Water Outlet Temperature (°C)	Air Inlet Temperature (°C)	Air Outlet Temperature (°C)
Experimental Data	15.16	27.64	20.86
CFD Data	14.28	27.13	19.76
Error (°C)	0.88	0.51	1.10
Error (%)	5.80	1.85	5.26

2.5.3.2. Validation Case-2

In the experimental study, servers L1,L13,L21,R1,R13 and R21 operate with 8 cores each. The layout of the working scenario is provided below:

Working Scenario Layout

Figure 2.33: Layout for Case-2.

The parameters used as inputs in the CFD model and obtained from the experimental study are presented in Table 2.10.

Table 2.10: Input parameters for Validation Case-2.

Water Inlet Temperature (°C)	VOR (%)	IFS (%)
11.31	55	30

The data obtained from simulations has been recorded and compared with experimental data. The information regarding the results is presented in Table 2.11.

Table 2.11: Comparison of simulated and measured data for Validation Case-2.

	Water Outlet Temperature (°C)	Air Inlet Temperature (°C)	Air Outlet Temperature (°C)
Experimental Data	15.06	56.59	20.62
CFD Data	13.95	24.82	18.48
Error (°C)	1.11	1.67	2.14
Error (%)	7.36	6.30	10.37

2.5.3.3. Validation Case-3

In the experimental study, servers L1, L7, L13, L17, L21, R3, R11 and R21 operate with 56 cores each. The layout of the working scenario is provided below:

Working Scenario Layout

Figure 2.34: Layout for Case-3.

The parameters used as inputs in the CFD model and obtained from the experimental study are presented in Table 2.12.

Table 2.12: Input parameters for Validation Case-3.

Water Inlet Temperature (°C)	VOR (%)	IFS (%)

| 10.68 | 50 | 30 |

The data obtained from simulations has been recorded and compared with experimental data. The information regarding the results is presented in Table 2.13.

Table 2.13: Comparison of simulated and measured data for Validation Case-3.

	Water Outlet Temperature (°C)	Air Inlet Temperature (°C)	Air Outlet Temperature (°C)
Experimental Data	16.14	28.47	22.06
CFD Data	15.59	29.31	20.49
Error (°C)	0.55	0.84	1.57
Error (%)	3.42	2.96	7.10

2.5.3.4. Validation Case-4

In the experimental study, servers L3, L11, L15, L19, R1, R3, R11, and R21 operate with 56 cores each. The layout of the working scenario is provided below:

Working Scenario Layout

Figure 2.35: Layout for Case-4.

The parameters used as inputs in the CFD model and obtained from the experimental study are presented in Table 2.14.

Table 2.14: Input parameters for Validation Case-4.

Water Inlet Temperature (°C)	VOR (%)	IFS (%)
11.24	55	30

The data obtained from simulations has been recorded and compared with experimental data. The information regarding the results is presented in Table 2.15.

Table 2.15: Comparison of simulated and measured data for Validation Case-4.

	Water Outlet Temperature (°C)	Air Inlet Temperature (°C)	Air Outlet Temperature (°C)
Experimental Data	15.29	27.60	21.02
CFD Data	14.38	27.52	19.90
Error (°C)	0.91	0.08	1.12
Error (%)	5.98	0.27	5.31

When the results of the comparison between the IPMI data obtained from various experimental studies and the numerical model were examined, it was concluded that the numerical model accurately represents the data centre, and the numerical model was validated.

3. Numerical Modelling of Two-Phase Heat Transfer

3.1. Numerical Model

The interface between liquid and vapor phases is tracked by monitoring the volume fraction of each phase that varies between 0 and 1. A value of 0 or 1 within a computational cell indicates that the cell is either completely empty or fully filled with a specific phase, respectively. The summation of volume fractions is always constant and equals to unity within a cell [66, 67]:

$$\alpha_v + \alpha_l = 1 \tag{12}$$

This ensures that the total volume of the cell is occupied by either vapor, liquid or liquid-vapor phases. The interface between liquid and vapor phases can be tracked by solving the following transport equation for the vapor phase in the Volume of Fluid (VOF) method [66, 67]:

$$\frac{\partial}{\partial t}(\rho_v \alpha_v) + \nabla \cdot (\rho_v \alpha_v u) = S_v \tag{13}$$

Where, α_v, ρ_v and u represent the vapor volume fraction, density and velocity field, respectively, and S_v denotes the mass source term associated with the phase change. The phase change is assumed to occur at a constant pressure and quasi-thermal equilibrium state in the Lee phase change model [67] Moreover, the phase change is mainly dependent on the deviation between interfacial cell temperature and saturation temperature. An empirical multiplier can be used to adjust associated mass flux through the interface. The mass transfer between phases can be defined as a mass source using the Lee model:

$$S_v = C\rho_l \alpha_l \left(\frac{T - T_{sat}}{T_{sat}}\right) \tag{14}$$

Where, C is the mass transfer intensity factor, ρ_l is the liquid density and α_l is the volume fraction of the liquid cell. Here, saturation and condensation processes can be modelled shifting the sign of the C in Eq. (14). The mass transfer intensity factor of 100 s^{-1} is considered as an optimal value in the Lee phase change model. Numerical results are

highly sensitive to the intensity factor and values significantly higher or lower than 100 s⁻¹ may result in unrealistic results [68, 69, 70, 71].

Physical properties of the fluid can be calculated by a weighted averaging of volume fractions within a cell to reflect the phase mixture accurately:

$$\phi = \alpha_l \phi_l + \alpha_v \phi_v \qquad (15)$$

Where, ϕ denotes the physical property of the mixture. Vapour and liquid phases share the same velocity field and can be governed by a single momentum equation [66]:

$$\frac{\partial}{\partial t}(\rho u) + \nabla.(\rho uu) = -\nabla p + \nabla[\mu(\nabla u + \nabla u^T)] + \rho g + F_s \qquad (16)$$

Where, p represents the pressure field, g is the gravitational acceleration vector and u is the mixture velocity. The body force F_s resulting from the surface tension at the interface can be calculated using the Continuum Surface Force (CSF) model [72]. The enthalpy at the phase change can be determined from the following equation:

$$\frac{\partial}{\partial t}(\rho E) + \nabla.[u(\rho E + p)] = \nabla.[k\nabla T] + S_h \qquad (17)$$

Where, S_h is the volumetric energy source and is the sensible enthalpy [66, 67]:

$$E = C_p(T - T_{sat}) \qquad (18)$$

Where, T is the temperature of the fluid and C_p is the specific heat capacity, which can be calculated from the following equation [66, 67]:

$$C_p = \frac{\alpha_v \rho_v C_{p,v} + \alpha_l \rho_l C_{p,l}}{\alpha_v \rho_v + \alpha_l \rho_l} \qquad (19)$$

Where, $C_{p,v}$ and $C_{p,l}$ are specific heat capacities of vapor and liquid phases, respectively.

The boiling heat flux generated from the solid to the fluid can be described by the following Newton's law of cooling:

$$T_{boiling} = h(T_{sub} - T_{sat}) \qquad (20)$$

Where, h is the heat transfer coefficient, T_{sub} and T_{sat} are subcooled and saturation temperatures, respectively.

3.2. Validation of the Numerical Model

3.2.1. One-Dimensional Stefan Problem

The one-dimensional Stefan problem is simulated within a two-dimensional region using OpenFOAM v2112 [62] (icoReactingMultiphaseEulerFoam and Lee phase change model). The phase change model is implemented via user-defined functions, with heat transfer and interface movement occurring along the x-axis. Free-slip and adiabatic conditions are applied at the top and bottom boundaries. Since no gradient exists along the y-axis, the solution is made one-dimensional.

Initially, a thin vapour film adheres to the wall, which is maintained at a constant temperature T_{wall}. This wall temperature is 5 K higher than the saturation temperature of the liquid. The vapour film is in contact with saturated liquid. In this simulation, the vapour film thickness corresponds to the thickness of the first mesh layer adjacent to the wall. The computational domain extends to a length of 1 mm. A no-slip condition is applied at x=0 and a specified pressure condition is imposed at x=1 mm. As time progresses, heat transfers from the wall to the vapour film and the phase interface. Consequently, the liquid phase transitions into the vapour phase, causing the interface to move along the x-axis. The analytical solutions for the interface position $x(t)$ and the temperature distribution $T(x,t)$ are provided by the Eq. (21) and Eq. (22):

$$x(t) = 2\beta \sqrt{\frac{k_v t}{\rho_v C_{p,v}}} \tag{21}$$

$$T(x,t) = T_{wall} + \left(\frac{(T_{sat} - T_{wall})}{erf(\beta)}\right) erf\left(\frac{x}{2\sqrt{tk_v/\rho_v C_{p,v}}}\right) \tag{22}$$

Where $erf(x)$ is the error function, and β is the solution of the transcendental equation:

$$\beta exp(\beta^2) erf(\beta) = \frac{C_{p,v}(T_w - T_{sat})}{h_{lv}\sqrt{\pi}} \tag{23}$$
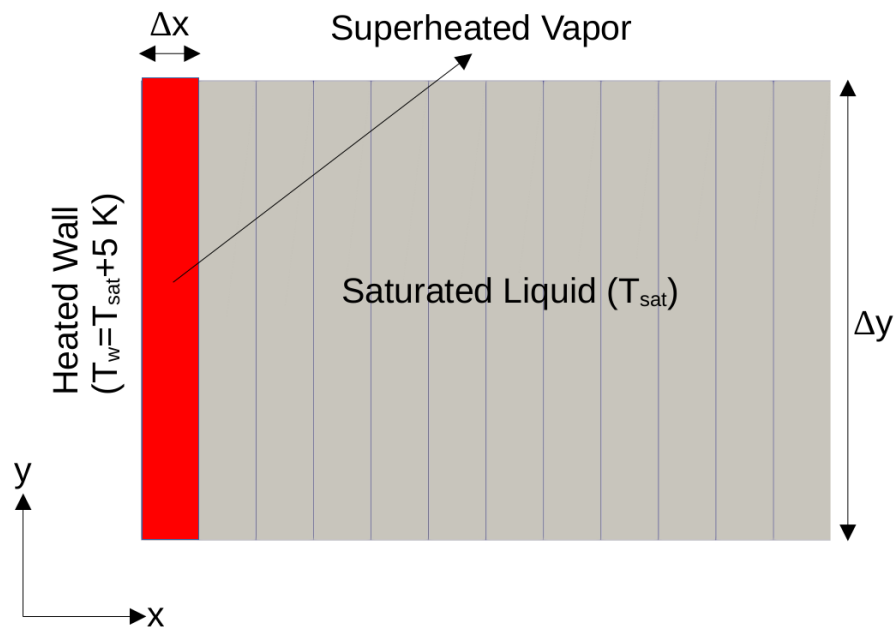
Figure 3.1: Schematic description of the Stefan Problem.

Table 3.1: Boundary conditions for the Stefan Problem.

Field	heatedWall	outlet	frontAndBack
alpha.gas	zeroGradient	zeroGradient	empty
alpha.water	zeroGradient	zeroGradient	empty
p	fixedFluxPressure	totalPressure	empty
p_rgh	fixedFluxPressure	totalPressure	empty
T	fixedValue 378.15 K	zeroGradient	empty
U	noSlip	pressureInletOutletVelocity	empty

Table 3.2: Phase change properties for the Stefan Problem.

Phase	heatedWall	outlet	frontAndBack
Vapour	pureMovingPhaseModel	Lee	373.15 K
Liquid	pureMovingPhaseModel	Lee	-

Table 3.3: Thermophysical properties of water and water vapour at 101.3 kPa for the Stefan Problem.

Phase	$\rho\ (kg/m^3)$	$\mu\ (kg/ms)$	$C_p\ (J/kgK)$	$k\ (W/mK)$	$h_{lv}\ (J/kg)$	$\sigma_{lv}\ (N/m)$
Vapour	0.597	1.26×10^{-5}	2030	0.025	2.26×10^6	0.0559
Liquid	958.4	2.8×10^{-4}	4216	0.679	2.26×10^6	0.0559

Table 3.4: Statistics of the computational mesh for the Stefan Problem.

Mesh	Number of Cells	Max Non-orthogonality	Skewness	Max. Aspect Ratio	Min. Volume	Max. Volume
Mesh1	400	0	2.77e-13	1	9.99e-14	1e-13
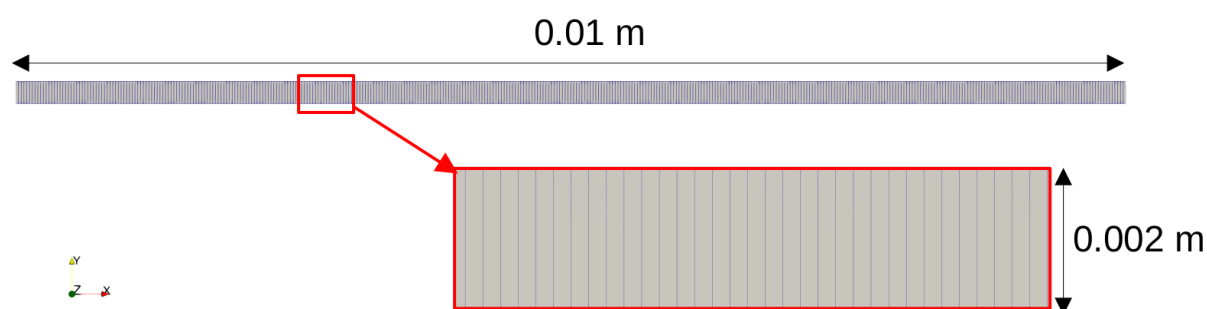
Figure 3.2: View of the block structured computational mesh.
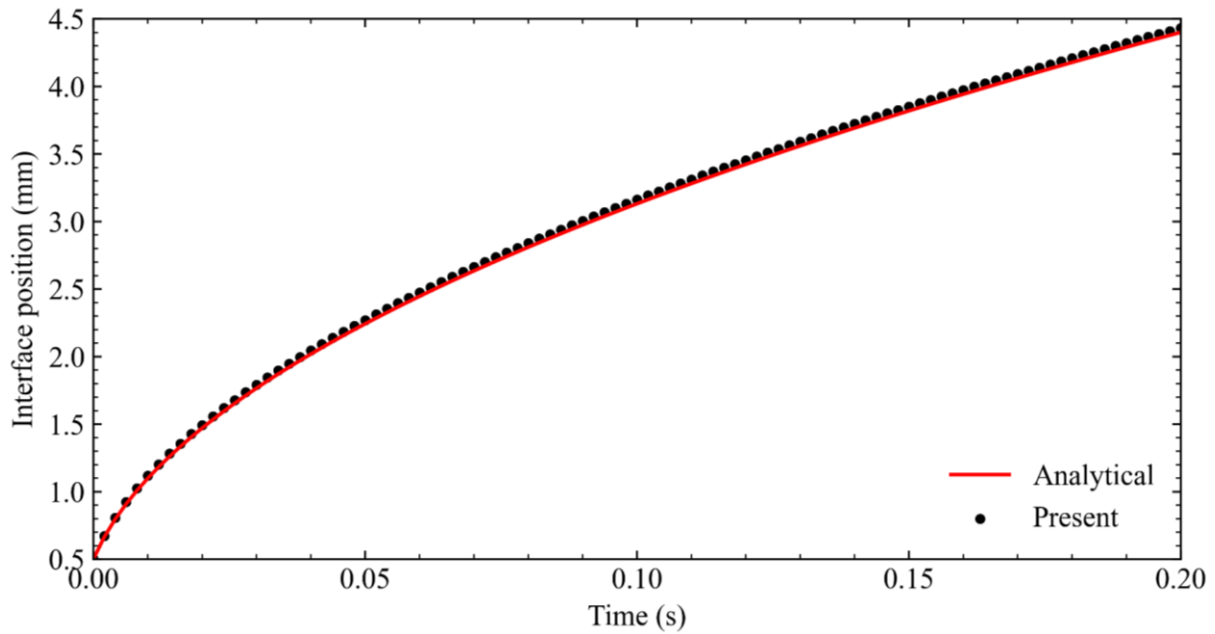
Figure 3.3: Comparison of numerical and analytical results for the Stefan Problem.
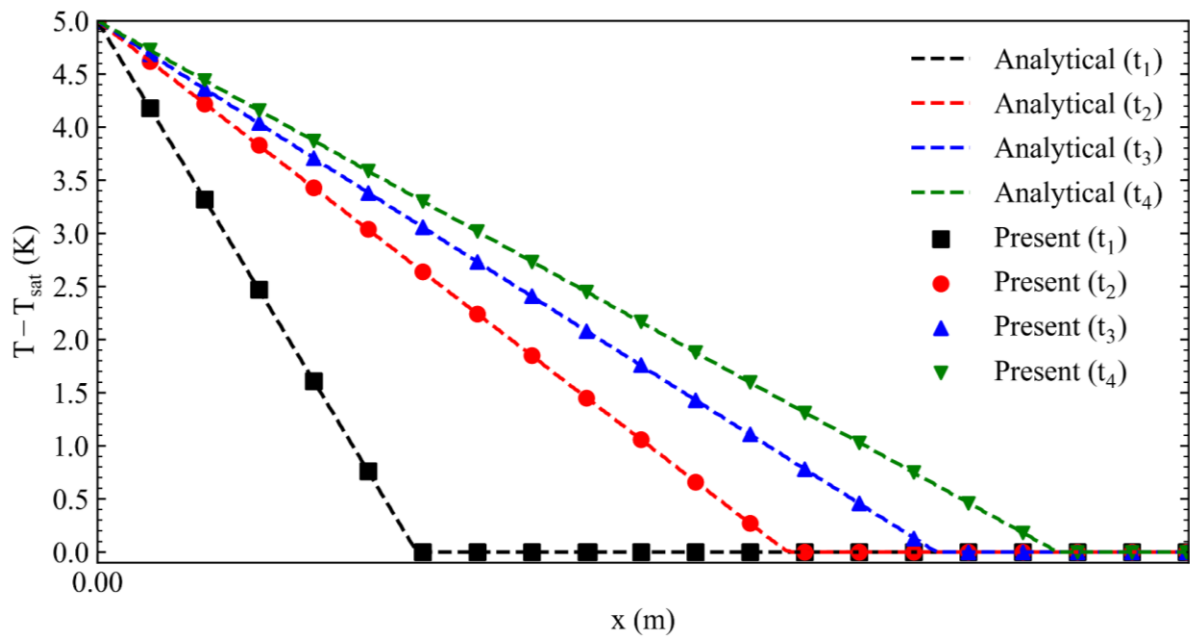
Figure 3.4: Variation of the superheat (T-Tsat) temperature with horizontal coordinate at various time-instants: t1=0.02 s, t2=0.1 s, t3=0.15 s and t4=0.2 s.

3.2.2. Two-Dimensional Film-Boiling

The present study utilises the icoReactingMultiphaseInterFoam solver in OpenFOAM [59] for the simulation of phase change heat transfer. Stability and accuracy of the numerical model are ensured through the Euler scheme for the implicit discretization of unsteady terms and Gauss-based schemes for the spatial discretizations of convective and diffusive terms in the governing equations. The vanLeer scheme is adopted for the discretization of divergence terms in the multiphase interaction to improve stability of the numerical model. Coefficients of a discretized equation are stored into a single matrix and each matrix is solved using a matrix solution algorithm in the segregated solution architecture of OpenFOAM. In this study, the GAMG (Generalised Geometric-Algebraic MultiGrid) solver is employed for the pressure field and the smoothSolver is used with the symGaussSeidel smoother for the remaining fields to ensure an efficient convergence. The Courant number is set to 1 to adjust time step dynamically during unsteady simulation of the film boiling process. The time step was calculated between 2.97×10^{-4} s and 1.2×10^{-3} s in the numerical simulations conducted in the present study.

As shown in Fig.3.5, a thin layer of vapor completely covers the surface of the heater by isolating liquid from the heater. Evaporation occurs at the interface, leading the generated vapor to continuously leave the film layer in the form of bubbles. The Rayleigh-Taylor instability induced by the gravity at the liquid-vapor interface results in a periodic wave pattern. The thickness of the vapor film can be predicted from the following equation [66]:

$$\delta = \frac{l_m}{128}\left(4 + cos\left(\frac{2\pi x}{l_m}\right)\right) \tag{24}$$

Where, l_m is the critical wavelength:

$$l_m = 2\pi \sqrt{\frac{3\sigma}{(\rho_l - \rho_v)g}} = 0.07868 \, m \tag{25}$$

Where, σ is the surface tension coefficient and g is the gravitational acceleration. Dimensions of the rectangular domain are defined according to the critical wavelength.
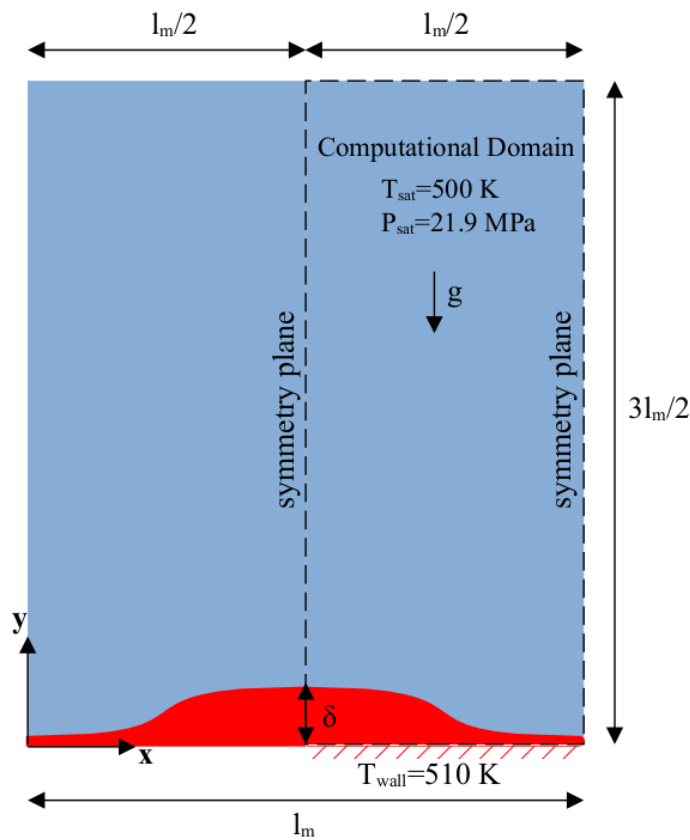
Figure 3.5: Schematic view of two-dimensional film boiling.

As shown in Fig.3.5, symmetry boundary conditions are applied at the vertical boundaries due to the fact that the numerical domain inherently exhibits a horizontal symmetry. The heater surface at the lower boundary is modelled using a constant temperature boundary condition. The wall temperature is set to $T_{sat} + \Delta T$ [66, 67, 73], where ΔT is the temperature difference. A coded boundary condition is developed and implemented to the solver to generate Taylor wavelength for the gas and liquid phases according to Eq. 25. Volume fractions of gas and liquid phases are set to 1 and 0, respectively, at the bottom wall. A no-slip boundary condition is imposed at the lower wall and a pressure-based velocity condition is applied at the upper wall. Pressure is set to 0 and a zero gradient condition is used for the temperature and volume fraction at the upper boundary. Combination of Drichlet and Neumann type boundary conditions ensures the stability and convergence of the present numerical model.

Table 3.5: Boundary conditions for two-dimensional film boiling.

field	upWall	downWall	walls	frontAndBack	internalField
alpha.gas	zeroGradient	fixedValue	symmetryPlane	empty	codeStream
alpha.water	zeroGradient	fixedValue	symmetryPlane	empty	codeStream
p	calculated	calculated	symmetryPlane	empty	uniform 0
p_rgh	prghTotalPressure	fixedFluxPressure	symmetryPlane	empty	uniform 0
T	inletOutlet	fixedValue uniform 510 K	symmetryPlane	empty	codeStream
U	pressureInletOutletVelocity	fixedValue	symmetryPlane	empty	uniform (0 0 0)

Two-dimensional film boiling illustrated in Fig.3.5 is considered for the validation of the numerical model. Initial temperatures of the liquid and interface equal to the and the temperature of the vapor film layer varies linearly from at the heater surface to the T_{sat} at the interface. Thermophysical properties of the fluid are given in Table 3.6 at a saturation temperature of 500 K and a reference pressure of 21.9 MPa, which are considered as near critical conditions [63].

Table 3.6: Thermophysical properties of liquid and gas at near critical conditions.

Phase	ρ (kg/m^3)	μ (kg/ms)	C_p (J/kgK)	k (W/mK)	h_{lv} (J/kg)	σ_{lv} (N/m)
Vapour	5	0.005	200	1	-	-
Liquid	200	0.1	400	40	10^4	0.1

Various mesh resolutions were generated and tested for ΔT_{sup} = 10 K to achieve a mesh independent solution. As compared with the numerical data from the literature in Fig. 3.6, relatively coarse meshes exhibited a premature bubble formation and separation, which is the indication of importance of mesh resolution on the temporal and spatial variations of bubble formation. Identical bubble formations are captured and the solution is no longer dependent on the mesh size when the mesh has 96x288 cells. The present mesh independent solution is identical to the literature data. Therefore, this mesh can be used reliably in the remaining simulations.
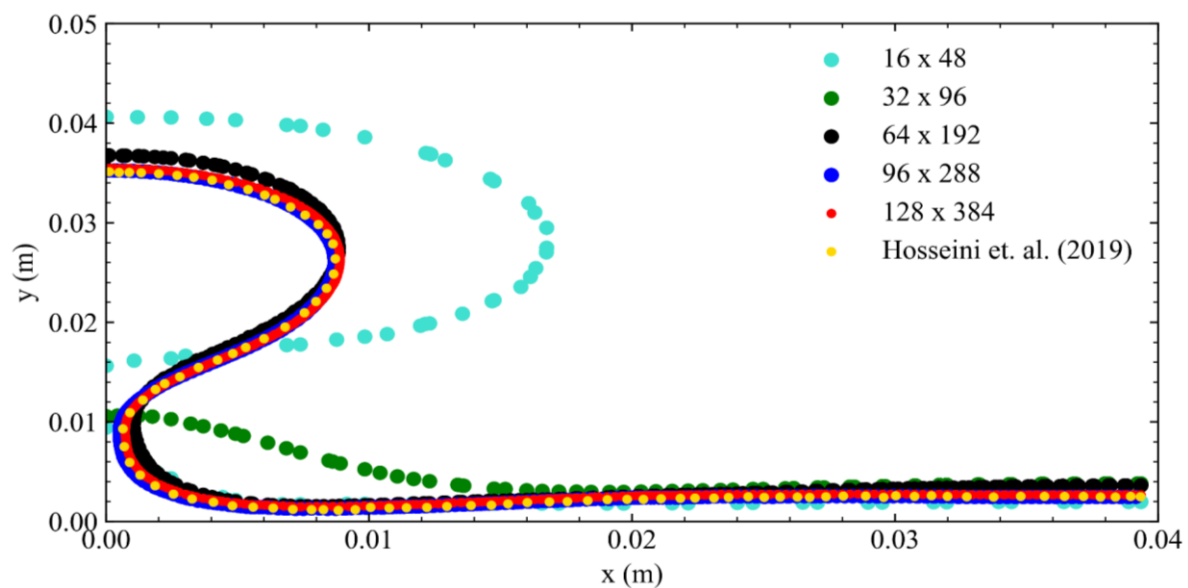
Figure 3.6: Simulated bubble formations at t=0.85 s using various mesh resolutions.

Two numerical simulations are performed using ΔT_{sup} = 10 K and ΔT_{sup} = 30 K and results are compared with previously reported experimental and numerical results [66, 73] in Fig. 3.7. A good consistency observed between present and previous results indicates that the present numerical model can accurately capture formation of bubbles under distinct heating conditions. As the temperature difference increases, the behaviour of the separated vapor film switches from the quasi-periodic bubble regime to the jet column regime, which results in a long term heat transfer. This observation proves that the bubble formation is associated with the heat transfer characteristics and can be managed by altering heat transfer at the interface.
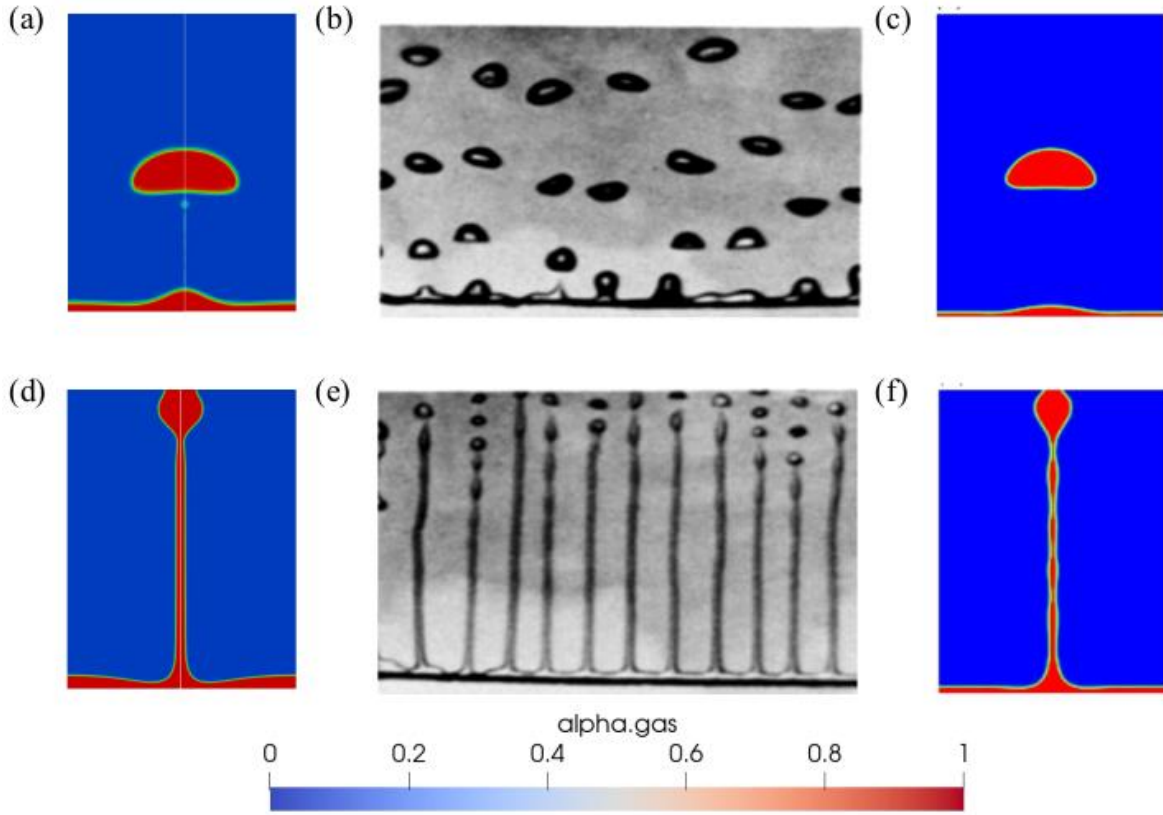
Figure 3.7: Comparison of vapor-liquid interface shapes for ΔTsup = 10 K: a) present, b) experimental [66] and c) numerical [73] and for ΔTsup = 30 K: d) present, e) experimental [66] and f) numerical [73].

A function object is developed and implemented to the present numerical model for the calculation of the Nusselt number from the following equation:

$$Nu = \frac{\int_0^{l_m} \left(\frac{\lambda}{T_e - T_{sat}} \times \frac{\partial T}{\partial y} \right) \partial x}{l_m} \quad (26)$$

The Nusselt number is calculated and printed to an output file with a sampling period of 0.01 s during numerical simulation. Time variation of the calculated Nusselt number is compared with the results of Hosseini et al. [66] in Fig. 3.7 along with the spatially averaged Nusselt numbers predicted by Berenson and Klimenko correlation coefficients [74, 75]. Fig. 3.8 clearly proves that the present numerical model simulates evaporation induced variation of the Nusselt number accurately.
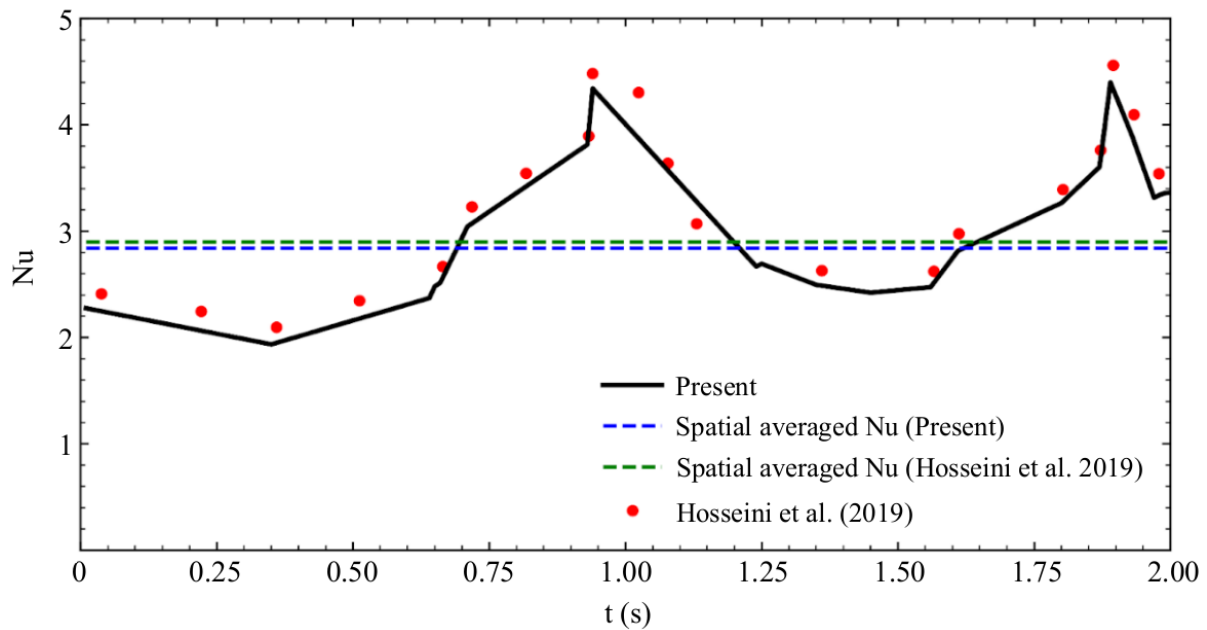
Figure 3.8: Comparison of time variation and spatially averaged Nusselt numbers [66].

3.3. Development of a Baffle Design for Heat Transfer Enhancement

3.3.1. The Micro-Baffle Design

The heat flux supplied from the bottom surface plays a vital role in the formation of bubbles. A continuous vapor layer forms on the bottom surface when the critical heat flux is exceeded, leading to a significant increase in surface temperature, which is essential for heat removal. Numerical simulations conducted in the present study paves the way to enhance heat transfer by altering flow and thermal fields. In this context, a micro-baffle that controls formation of rising bubble is proposed. As depicted in Fig. 3.9, the baffle is placed at a specific location close to the heated surface and oriented from the bottom to the top with an angle of β. Location of the bottom corner of the baffle is represented by C(xb, yb), the length of the baffle is Lb and the orientation angle is, which are design parameters to be optimized to achieve the best performance. The optimal location will be searched between minimum and maximum values of horizontal and vertical coordinates, which are calculated and listed in Table 3.7 for the present heating conditions. Values are also non-dimensionalized with respect to the wavelength for the interpretation of the design parameters in terms of wavelength.

Table 3.7: Minimum and maximum coordinates of the micro-baffle.

Variable	Value (mm)	Non-dimensionalized with respect to the l_m
xb_{min}	5	1/16
xb_{max}	20	1/4
yb_{min}	5	1/16
yb_{max}	15	3/16
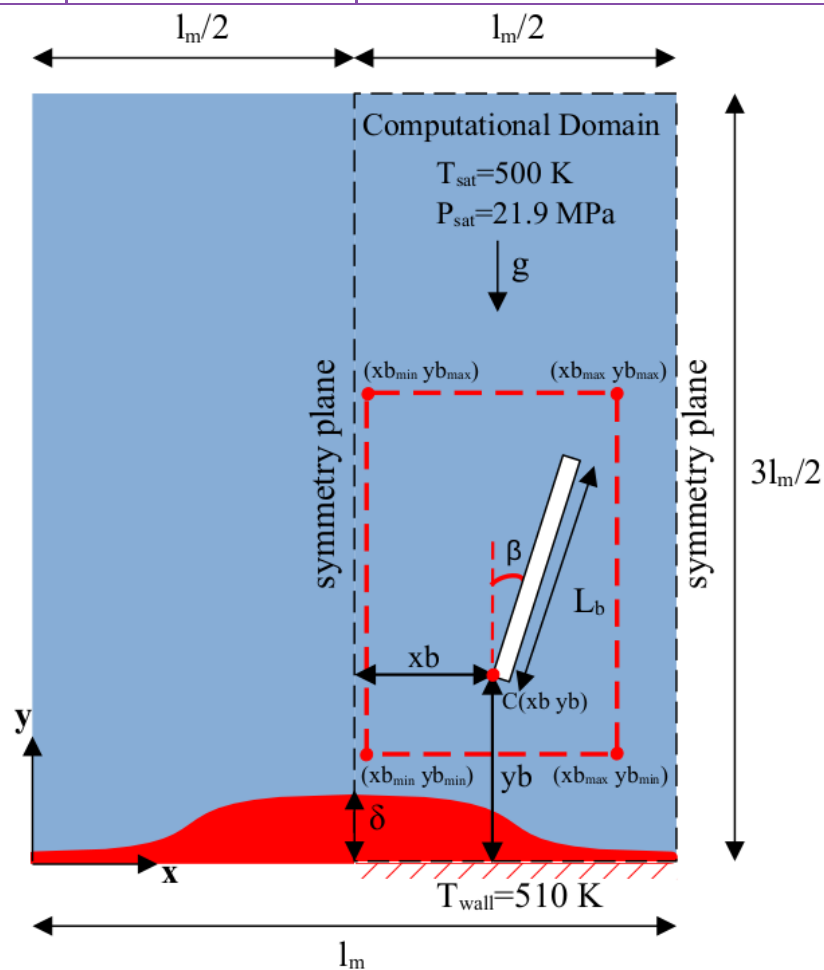
Figure 3.9: Parametric representation of the micro-baffle.

3.3.2. Influence of the Baffle Location

Numerical simulations are performed by changing the location of the baffle corner at 2.5 mm and 5 mm in the horizontal and vertical directions, respectively, keeping β=0 and Lb=20 mm to see the influence of the location on the heat transfer characteristics. As listed in Table 3.8, minimum, maximum and mean Nusselt numbers are calculated along with the performance improvement with respect to the no-baffle case, which is called Case$_0$. Maximum improvement has been achieved in Case$_{Xb3}$, where xb=10 mm and yb=5 mm. Another important observation from the numerical simulations is that the influence of vertical coordinate is trivial on the heat transfer mechanism. Time variations of Nusselt numbers are plotted in Fig. 3.10 for no-baffle and baffle cases.

Table 3.8: Optimization of the baffle location.

Case	xb (mm)	yb (mm)	Nu_{min}	Nu_{max}	Nu_{mean}	Enhancement (%)
Case$_{xb1}$	5	5	2.9	4.2	3.6	13.5
Case$_{xb2}$	7.5	5	1.8	4.8	3.3	4.1
Case$_{xb3}$	10	5	3.8	5.9	4.8	53.6
Case$_{xb4}$	12.5	5	3.4	5.7	4.5	44.5
Case$_{xb5}$	15	5	3.1	5.6	4.3	37.5
Case$_{xb6}$	17.5	5	2.4	3.6	3.0	-5.9
Case$_{xb7}$	20	5	2.6	3.8	3.2	0.6
Case$_{yb1}$	10	7.5	3.6	5.9	4.8	50.8
Case$_{yb2}$	10	10	3.5	5.9	4.7	48.4
Case$_{yb3}$	10	12.5	2.5	4.3	3.4	47.9

Case$_{yb4}$	10	15	3.4	5.9	4.6	47.6

A significant improvement has been achieved in the Nusselt number when the location of the baffle has been optimised. The proposed design also reduced the period of the oscillating Nusselt number successfully. The Nusselt number also remains unchanged between two peaks.
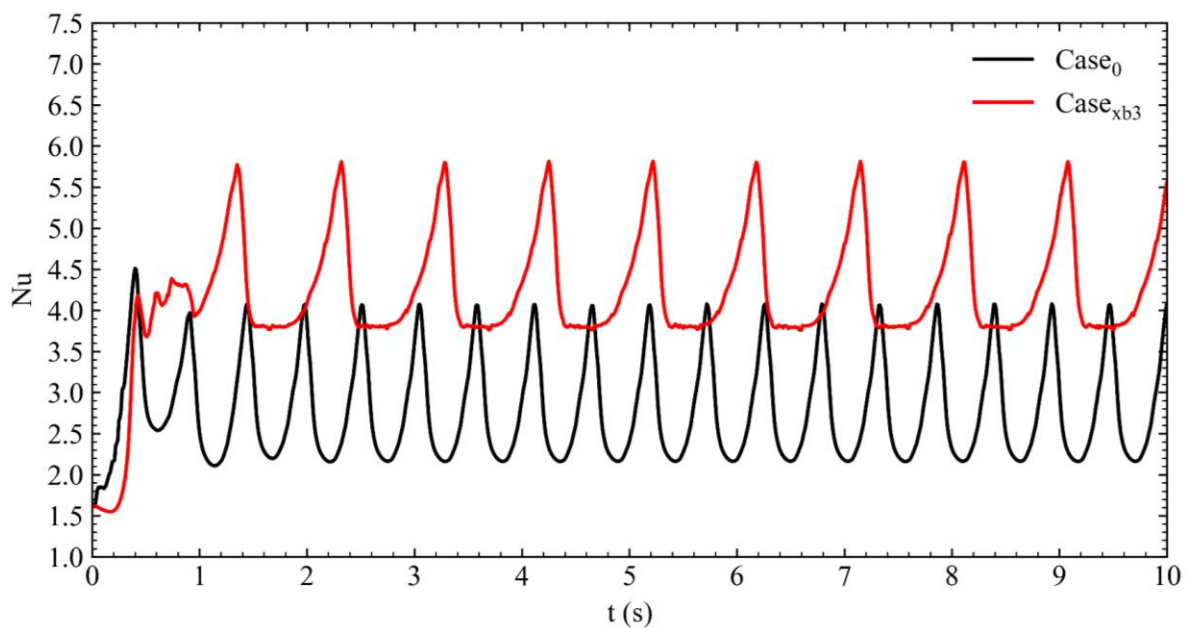
Figure 3.10: Time variations of the Nusselt numbers for Case$_0$ and Case$_{Xb3}$.

3.3.3. Influence of the Baffle Length

The length of the baffle is crucial for the accumulation of gas within the channel and the continuity of the flow. Influence of the baffle length is investigated by changing the length of the baffle between 5 mm and 60 mm for the optimal location determined in the previous part of the study. Maximum enhancement reaches 57.4% for Lb=40 mm and influence of the baffle length is observed to be trivial for longer baffles. Thus, the optimal baffle length has been decided to be as Lb=40 mm considering cost of the design since ratio of the performance improvement to the baffle length approaches zero. On the other hand, choosing a relatively smaller baffle length will provide flexibility in the implementation of the proposed design.

Table 3.9: Optimization of the baffle length.

Case	Lb (mm)	Nu_{min}	Nu_{max}	Nu_{mean}	Enhancement (%)
$Case_{lb1}$	5	1.6	4.8	3.2	0.9
$Case_{lb2}$	10	1.8	5.6	3.7	46.6
$Case_{lb3}$	15	3.8	5.8	4.8	52.8
$Case_{lb4}$	20	3.8	5.9	4.8	53.6
$Case_{lb5}$	25	3.8	5.9	4.9	54.2
$Case_{lb6}$	30	3.8	6.0	4.9	55.2
$Case_{lb7}$	35	3.8	6.0	4.9	55.8
$Case_{lb8}$	40	3.8	6.2	5.0	57.4
$Case_{lb9}$	45	3.8	6.2	5.0	57.5
$Case_{lb10}$	50	3.8	6.3	5.0	59.5
$Case_{lb11}$	55	3.8	6.3	5.0	59.6
$Case_{lb11}$	60	3.8	6.3	5.1	61.0

Time variations of the Nusselt numbers are compared in Fig. 3.11 for $Case_0$ and $Case_{lb8}$. The proposed design has increased not only the Nusselt number but also the oscillation period by changing the formations of bubbles effectively. A strong interaction is observed between oscillation period and maximum value of the Nusselt number. Mean values are calculated when the quasi steady-state is achieved.
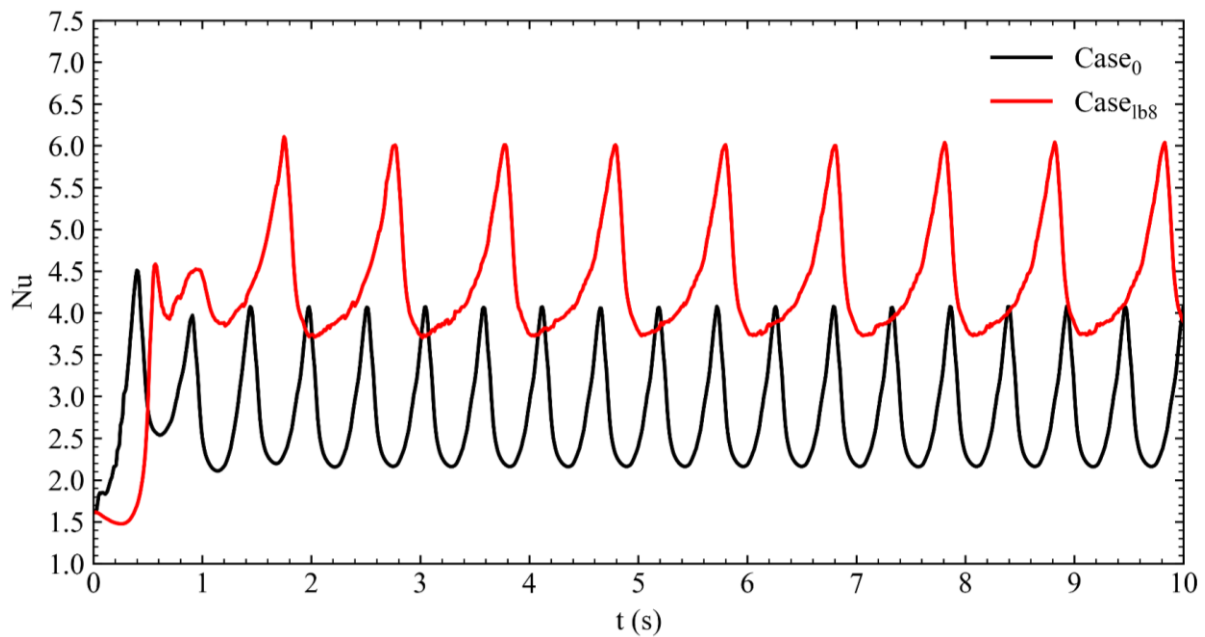
Figure 3.11: Time variations of the Nusselt numbers for $Case_0$ and $Case_{lb8}$.

3.3.4. Influence of the Baffle Rotation

The effect of the orientation is investigated between 0° to 45° keeping the baffle location and length as optimal values. The reason for choosing 45° as the upper limit is that it is the boundary angle where the baffle does not extend beyond the calculation domain. The baffle was oriented clockwise in the numerical experiments. Numerical simulation results listed in Table 3.10 revealed that the orientation angle has a negative effect on the Nusselt number due to the fact that the Nusselt number reduces once the baffle is oriented. Thus, the vertical baffle is preferred for the maximum efficiency.

Table 3.10: Optimization of the baffle rotation.

Case	β (°)	Nu_{min}	Nu_{max}	Nu_{mean}	Enhancement (%)
Caseβ_1	5	3.5	6.1	4.8	52.1
Caseβ_2	10	3.2	5.9	4.6	45.5
Caseβ_3	15	3.5	4.5	4.	27.2
Caseβ_4	20	3.7	4.6	4.1	31.6
Caseβ_5	25	3.8	4.6	4.2	34.7
Caseβ_6	30	3.8	4.5	4.2	32.6
Caseβ_7	35	3.8	3.9	3.9	23.1
Caseβ_8	40	2.5	3.1	2.7	-13.5
Caseβ_9	45	2.3	2.6	2.5	-21.5

Formations of the bubbles are visualized for the optimal micro-baffle design in Fig. 3.12. The optimal micro-baffle design has been observed to significantly increase the volume fraction of the gas phase just prior to the formation of the first bubble and detaches from the lower surface. This elevated volume fraction leads to a rise in the Nu, which in turn enhances the heat transfer. The micro-baffle design creates larger and continuous bubble formations that break over a longer duration. This modification reduces the period of the oscillating Nusselt number calculated on the bottom surface. Additionally, the optimal design promotes continuous bubble formation at lower temperatures. This continuous and stabilized bubble formation indicates a sustained increase in heat transfer efficiency as the process progresses.
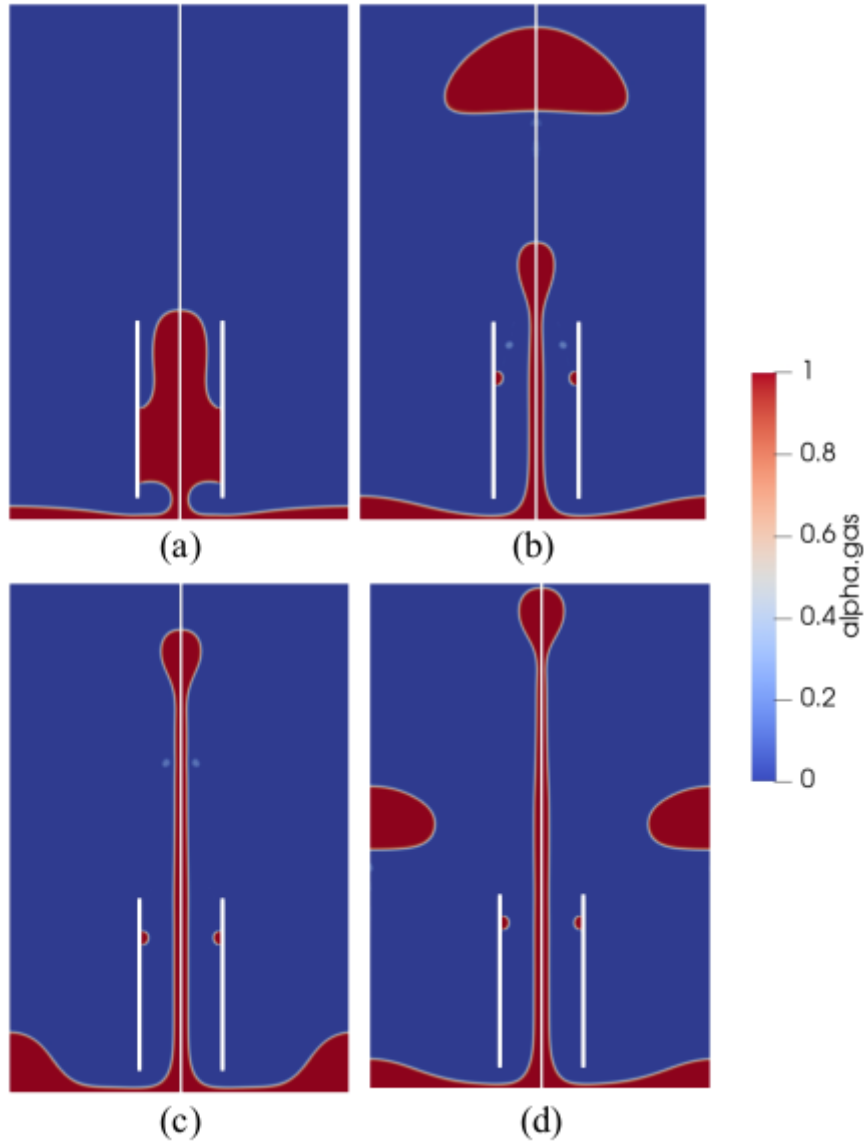
Figure 3.12: Bubble formation for the optimal case at a) t=0.71 s, b) t=1.06 s, c) t=1.55 s and d) t=2.09 s.

The CHF is a good indicator for the assessment of the heat transfer enhancement. The CHF is recognized as the maximum latent energy transport from the heating surfaces, which can be expressed as [76]:

$$q_{CHF} = u_c h_{lg} \rho_v \frac{A_g}{A_h} \tag{27}$$

$$u_c = \sqrt{\frac{2\pi\sigma}{\rho_v l_m}}$$

(28)

Where u_c is the critical vapor velocity, h_{lg} is the latent heat of the working fluid, ρ_v is the vapor density, A_g and A_h are areas of the vapor column and heater surface, respectively. The values are calculated as 100.03 kW/m2 and 166.40 kW/m2 for the cases of no-baffle and optimal baffle design, respectively. Thus, the proposed design yields a 66.4% improvement in the CHF, which is a significant improvement.

A series of numerical simulations are performed for the optimization of the parameters of the proposed design. The results indicated that the vertical baffle yielded the maximum efficiency. While the horizontal position of the baffle significantly influenced the heat transfer performance, the vertical position was found to be less impactful. The length of the baffle emerged as a critical factor in enhancing heat transfer efficiency. The optimal baffle design resulted in a 57.4% improvement in the Nusselt number and a 66.4% increase in the CHF. Moreover, the proposed baffle facilitated the formation of a continuous bubble column, even with a smaller temperature difference between the wall and the subcooled liquid ($T_{wall} - T_{sat}$), which is essential for energy-efficient engineering designs where film boiling occurs.

The current study primarily focuses on the conceptual validation of a micro-baffle design for enhancing heat transfer during film boiling. The placement of the micro-baffles at the optimal location can be achieved using fine and high-temperature-resistant micro cables, which can be deployed laterally over the heat source. While the current approach demonstrates the feasibility of the design, future work will address practical considerations in more detail. This includes investigating the integration of the micro-baffle system in real-world settings, such as flow and pool boiling applications, where structural stability and ease of installation are critical.

4. Numerical Modelling of Direct-on-chip Two-Phase Cold Plate

4.1. Dataset Generated from the ZutaTool

The ZutaTool developed by ZutaCore provides graphs showing the relationship between water temperature, pressure drop, and flow rate for specified Heat Rejection Unit (HRU) and CPU models. Within ZutaTool, the HRU and CPU models are selected from the available options. Additionally, the number of CPUs, TDP, and required case temperature are provided as inputs. Based on these inputs, a graph specific to water temperature, pressure drop, and flow rate is generated. A figure of the tool's interface is provided below [77].
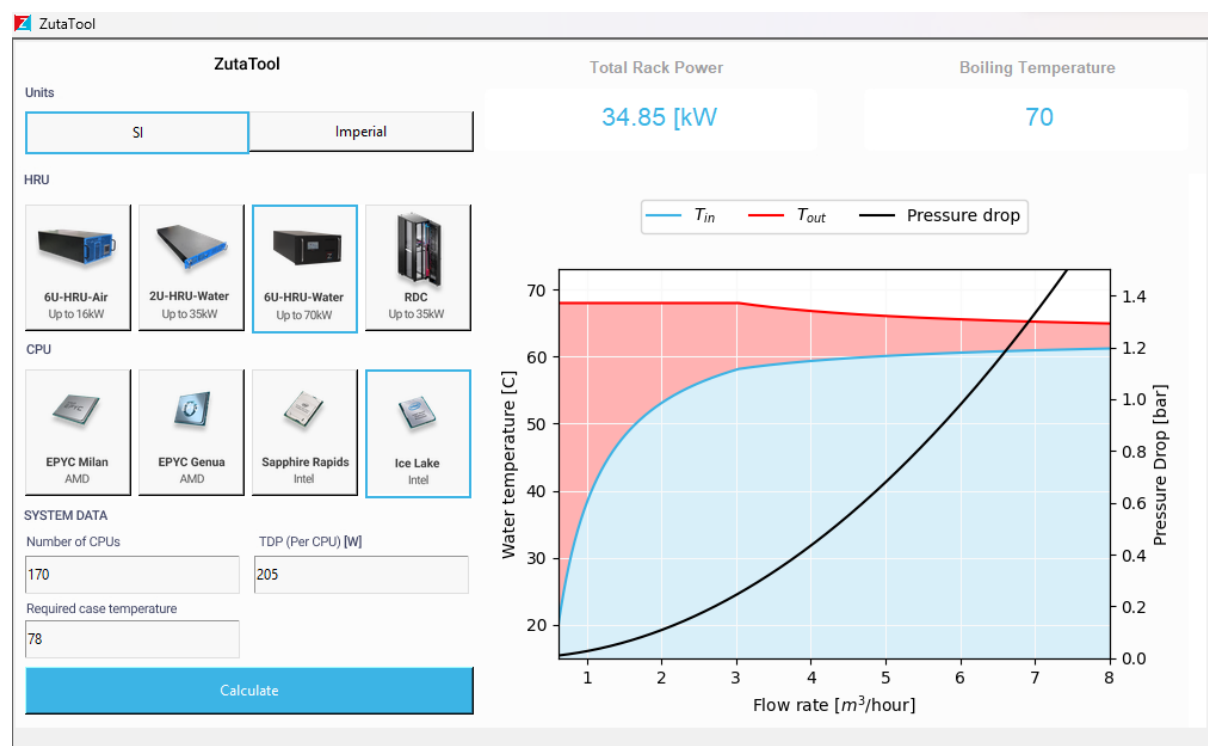
Figure 4.1: Snapshot of the ZutaTool interface.

The use of this tool aims to generate a dataset for the validation of the numeric model. In this dataset, considering the Empa data centre, the number of CPUs has been set to 64. The parameters from the resulting dataset have been compiled into a graph.

Table 4.1: Parameters of the data set generated by ZutaTool.

Dataset	TDP (W)	TRP (kW)	Boiling Temperature (°C)
Dataset1	35	2.24	79
Dataset2	55	3.52	78
Dataset3	75	4.8	77
Dataset4	95	6.08	76
Dataset5	115	7.36	76
Dataset6	135	8.64	75
Dataset7	150	9.6	74

Each graph corresponding to the provided parameters has been saved for use in validation studies.

4.2. Governing Equations

A three-dimensional numerical model of two-phase flow and solid-fluid Conjugate Heat Transfer (CHT) is used to capture the flow and heat transfer characteristics in a ZutaCore solution [77]. The model assumes a uniform, time-independent heat flux along the bottom surface of the chip. Additionally, the thermo-physical properties of the fluid (both liquid and vapor phases) and the solid are considered constant throughout the simulation. A two-phase numerical model based on the Euler-Euler approach is employed to solve the CHT problem [78, 79, 80]. Phase change phenomena such as boiling are integrated into the model by adjusting the source terms in the mass, momentum and energy conservation equations. In this model, the liquid phase is treated as the continuous primary phase,

while the vapor phase is modelled as depending on the boiling temperature secondary phase. Where, v is the vapor, l is the liquid, i and j are vector indices, α is the volume fraction, ρ is the density, S_{mass} is the mass source, S_{mom} is the momentum source and S_{en} is the energy source.

$$\frac{\partial}{\partial t}(\rho_v \alpha_v) + \frac{\partial}{\partial x_i}(\rho_v \alpha_v u_i) = S_{mass,v} \tag{29}$$

$$\frac{\partial}{\partial t}(\rho_l \alpha_l) + \frac{\partial}{\partial x_i}(\rho_l \alpha_l u_i) = S_{mass,l} \tag{30}$$

$$\frac{\partial}{\partial t}(\rho_v \alpha_v u_i) + \frac{\partial}{\partial x_j}(\rho_v \alpha_v u_i u_j) = -\alpha_v \frac{\partial p}{\partial x_i} + \frac{\partial}{\partial x_j}(\alpha_v \tau_{ij}) + \alpha_v \rho_v g_i + S_{mom,v} \tag{31}$$

$$\frac{\partial}{\partial t}(\rho_l \alpha_l u_i) + \frac{\partial}{\partial x_j}(\rho_l \alpha_l u_i u_j) = -\alpha_l \frac{\partial p}{\partial x_i} + \frac{\partial}{\partial x_j}(\alpha_l \tau_{ij}) + \alpha_l \rho_l g_i + S_{mom,l} \tag{32}$$

$$\frac{\partial}{\partial t}(\rho_v \alpha_v h_v) + \frac{\partial}{\partial x_j}(\rho_v \alpha_v u_i h_v) \tag{33}$$
$$= -\alpha_v \frac{\partial(\rho u_i)}{\partial x_i} + \frac{\partial}{\partial x_j}(\alpha_v \tau_{ij} u_i) - \alpha_v \frac{\partial q_i}{\partial x_i} + \alpha_v \rho_v g_i u_i + S_{en,v}$$

$$\frac{\partial}{\partial t}(\rho_l \alpha_l h_l) + \frac{\partial}{\partial x_j}(\rho_l \alpha_l u_i h_l) = -\alpha_l \frac{\partial(\rho u_i)}{\partial x_i} + \frac{\partial}{\partial x_j}(\alpha_l \tau_{ij} u_i) - \alpha_l \frac{\partial q_i}{\partial x_i} + \alpha_l \rho_l g_i u_i + S_{en,v} \tag{34}$$

4.3. A box model for ZutaCore Solution

A fictitious two-phase CHT model was developed using a box model, based on the external dimensions and the inlet/outlet locations extracted from the STEP file of the EOL 2011 cold plate model. This model mirrors ongoing experimental studies being conducted on OCP servers.
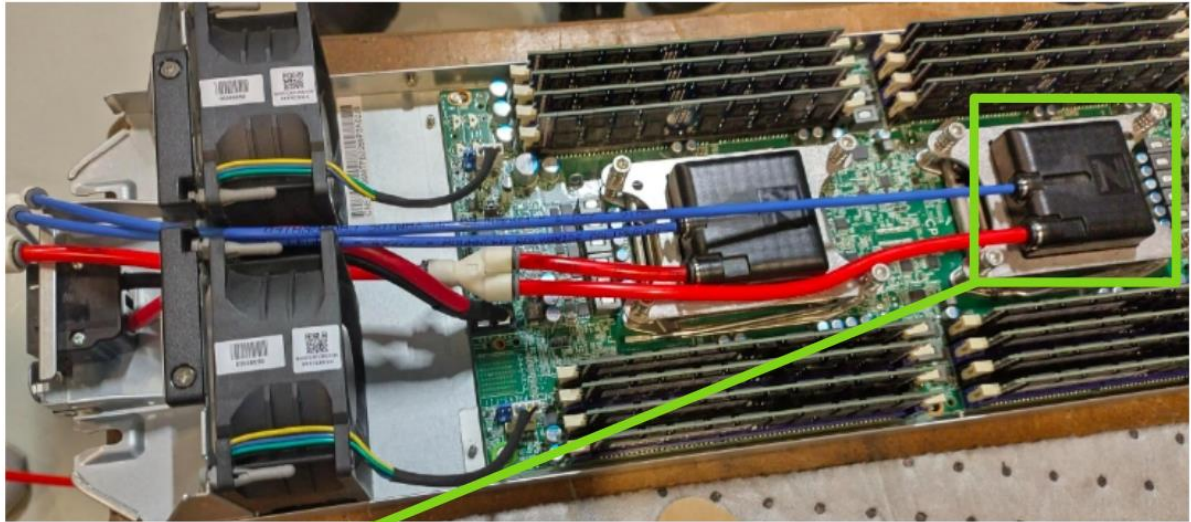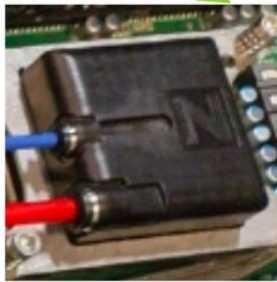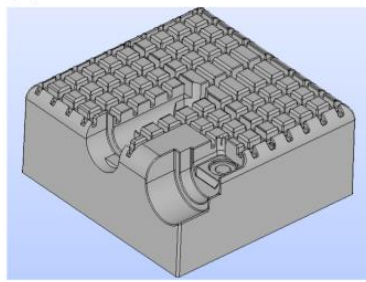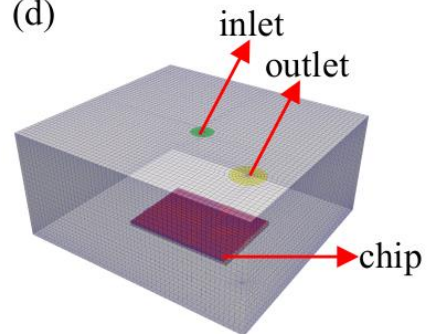
Figure 4.2: a) Snapshot of the direct-on-chip two-phase cold plate to the OCP Leopard v3.1 server, b) real model of EOL cold plate, c) CAD model and d) box model.

In the box numerical model, the computational domain is initially half-filled with liquid. Liquid enters through the inlet (u_{inlet} = 0.25 m/s), while only vapor exits at the outlet. Boiling occurs at the chip surface, where the generated vapor accumulates at the top of the domain and is subsequently removed from the system. The model also incorporates constant pressure and constant boiling temperature conditions to simulate the phase change behaviour accurately. The ZutaCore solution uses Opteon SF33 dielectric fluid as heat transfer fluid. The thermophysical properties of Opteon SF33 are [81]:

- Molecular weight: 164 g/mol
- Boiling point: 33.4 °C
- Density at 25 °C: 1.36 g/cm3
- Viscosity at 25 °C: 0.38 cP

- Vapor pressure at 25 °C: 0.07MPa
- Critical temperature: 171.3 °C
- Critical pressure: 2.9 MPa
- Heat of vaporization at boiling point: 166 kJ/kg
- Thermal conductivity at 25 °C: 0.077 W/mK
- Specific heat at 25 °C: 1.2 kJ/kgK
- Surface tension: 0.013 N/m

The properties for phase change were selected according to the thermophysical properties. ThermalPhaseChangeTwoPhaseSystem was selected for phase change and vapor and liquid were defined separately. Boiling temperature was determined with ZutaTool and boiling pressure was selected as constant. For the boiling properties, the alphatWallBoilingWallFunction boundary condition is applied to the walls. Since boiling primarily initiates at the surface where the solid-to-fluid transition occurs, sub-properties are incorporated into the alphatWallBoilingWallFunction. The Lemmert-Chawla [82] model is employed for nucleation site density, with the Cn parameter set to 185. The Departure Diameter Model is governed by the Tolubinski-Kostanchuk [83] theory, while the Departure Frequency Model follows the Cole [84] model. The Leidenfrost behaviour is modelled using the Spiegler [85] theory, the Critical Heat Flux Subcooled Model is governed by the Hua-Xu theory, with Kburn parameter set to 0.5 and the film boiling model is based on Bromley's theory [86].

4.4. Computational Mesh and Boundary Conditions

Heat energy supplied from the bottom of the solid region travels upward, reaching the interface with the fluid domain at the top surface. This surface, which overlaps with the fluid domain, induces boiling and phase change in the fluid. The computational mesh, utilizing a block-structured approach, is shown in Figure 4.3.
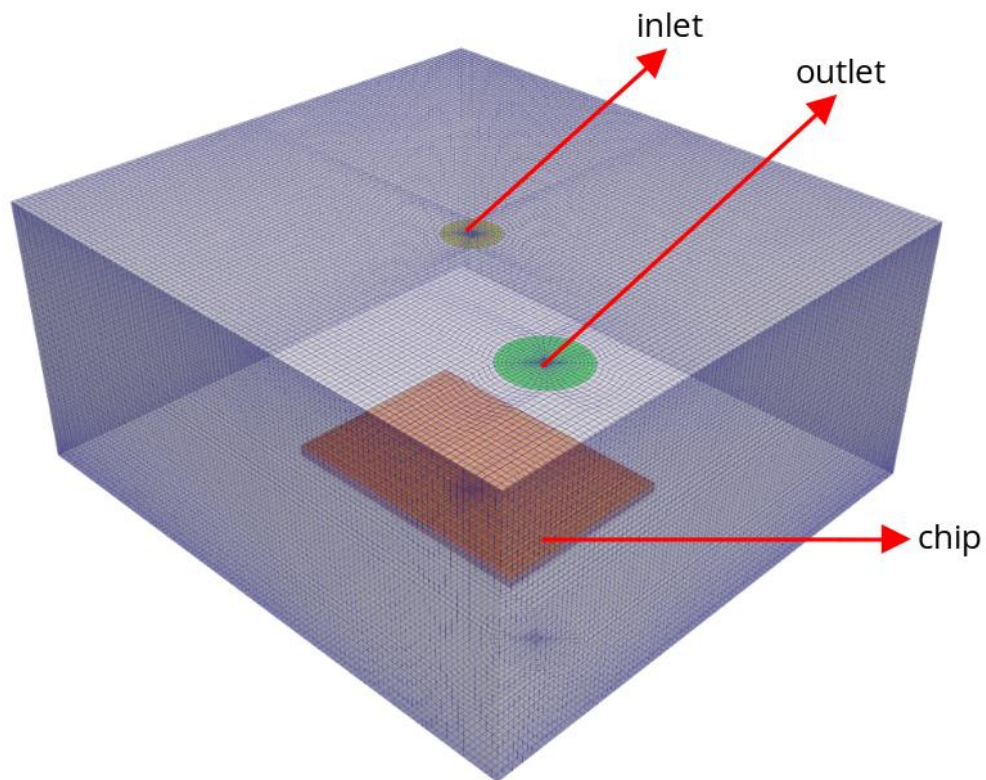
Figure 4.3: Block-structured mesh for the box model.

The computational mesh statistics of the box model are given in Table 4.2.

Table 4.2: Mesh statistics for the box model.

Region	Number of Cells	Max Non-orthogonality	Skewness	Min. Volume	Max. Volume
Fluid	817,040	5.01	0.58	1.36×10^{-12}	1.69×10^{-10}
Solid	2,470	0	0	1.98×10^{-10}	1.98×10^{-10}

Since only dielectric liquid enters through the inlet and only vapor exits through the outlet, the liquid volume fraction is set to 1 at the inlet, while the vapor volume fraction

is set to 1 at the outlet. The boundary conditions for the box model fluid and solid regions are summarized in Table 4.3 and Table 4.4, respectively.

Table 4.3: Boundary conditions for the fluid region.

field	inlet	outlet	walls	fluid_to_solid
alpha.gas	zeroGradient	inletOutlet	zeroGradient	zeroGradient
alpha.liquid	fixedValue	inletOutlet	zeroGradient	zeroGradient
p	calculated	calculated	calculated	calculated
p_rgh	fixedFluxPressure	prghTotalPressure	fixedFluxPressure	fixedFluxPressure
T.gas	zeroGradient	inletOutlet	fixedValue	fixedValue
T.liquid	fixedValue	inletOutlet	fixedValue	compressible::turbulentTemperatureTwoPhaseRadCoupledMixed
U.gas	fixedValue	pressureInletOutletVelocity	fixedValue	fixedValue
U.liquid	fixedValue	pressureInletOutletVelocity	fixedValue	fixedValue
alphat.gas	compressible::alphatWallBoilingWallFunction	calculated	compressible::alphatWallBoilingWallFunction	compressible::alphatWallBoilingWallFunction
alphat.liquid	compressible::alphatWallBoilingWallFunction	calculated	compressible::alphatWallBoilingWallFunction	compressible::alphatWallBoilingWallFunction (with sub-models)
f.gas	zeroGradient	inletOutlet	zeroGradient	zeroGradient

k.gas	fixedValue	inletOutlet	kqRWallFunction	kqRWallFunction
k.liquid	fixedValue	inletOutlet	kqRWallFunction	kqRWallFunction
epsilon.gas	fixedValue	inletOutlet	epsilonWallFunction	epsilonWallFunction
epsilon.liquid	fixedValue	inletOutlet	epsilonWallFunction	epsilonWallFunction
nut.gas	fixedValue	calculated	nutkWallFunction	nutkWallFunction
nut.liquid	fixedValue	calculated	nutkWallFunction	nutkWallFunction

Table 4.4: Boundary conditions of box model for solid region.

field	solid_bottom	solid_walls	solid_to_fluid
p	calculated	calculated	calculated
T	externalWallHeatFluxTemperature	zeroGradient	compressible::turbulentTemperatureTwoPhaseRadCoupledMixed

4.5. Results of the Box Model

In this box model which is half-filled with liquid, the inlet velocity of the liquid is set to 0.25 m/s, while the chip's temperature is maintained at 80°C. Additionally, the thermal design power (TDP) is specified at 115 W. In the two-phase flow model, bubble size plays a crucial role in determining flow behaviour, making it essential to generate a mesh capable of accurately capturing the bubbles' dimensions. To ensure the reliability of the results, a mesh independence study was conducted, as shown in Figure 4.4. It was found that simulations using 819,510 cells or more produced consistent results, indicating that

further mesh refinement would not significantly affect the outcomes, thereby confirming mesh independence.
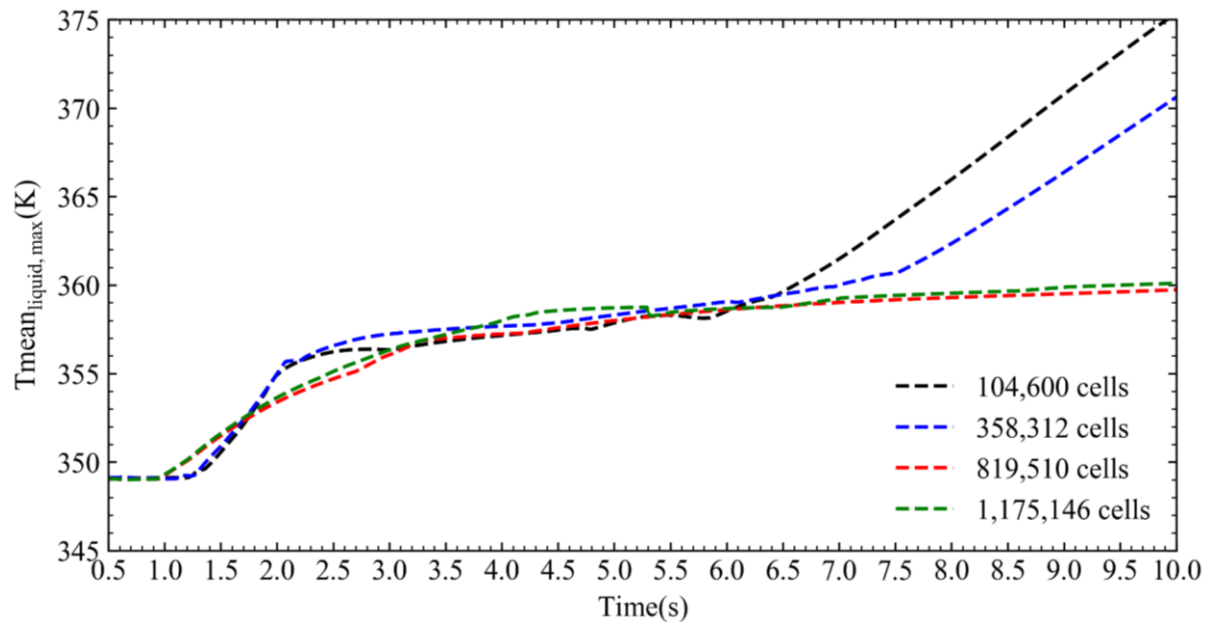
Figure 4.4: Mesh independence study of box model.

According to the ZutaTool's calculations, the boiling temperature is determined to be 76°C which leads to the onset of boiling immediately once the system reaches this temperature. As the process unfolds, the liquid begins to evaporate, causing a noticeable increase in vapor volume, while the liquid volume gradually diminishes. This phase change from liquid to vapor is driven by the thermal energy supplied to the system under the given initial conditions.

Over time, as more liquid evaporates, the interaction between the liquid and vapor phases becomes increasingly complex. The expansion of the vapor phase creates a buoyancy-driven flow, with hot vapor rising through the cooler surrounding gas phase, enhancing convective heat transfer within the system. This interaction continues until the liquid volume is sufficiently reduced, altering the dynamics within the box model.

Eventually, the system progresses toward equilibrium as the rate of evaporation slows down due to the decreasing liquid volume and diminishing thermal gradients. At this point, the vapor volume stabilizes and the gas temperature distribution within the system, including at the outlet, approaches a steady-state condition. In this steady state, the temperature, vapor generation and other system variables remain nearly constant,

indicating that the system has reached a point of dynamic balance between heat input, evaporation and vapor release.
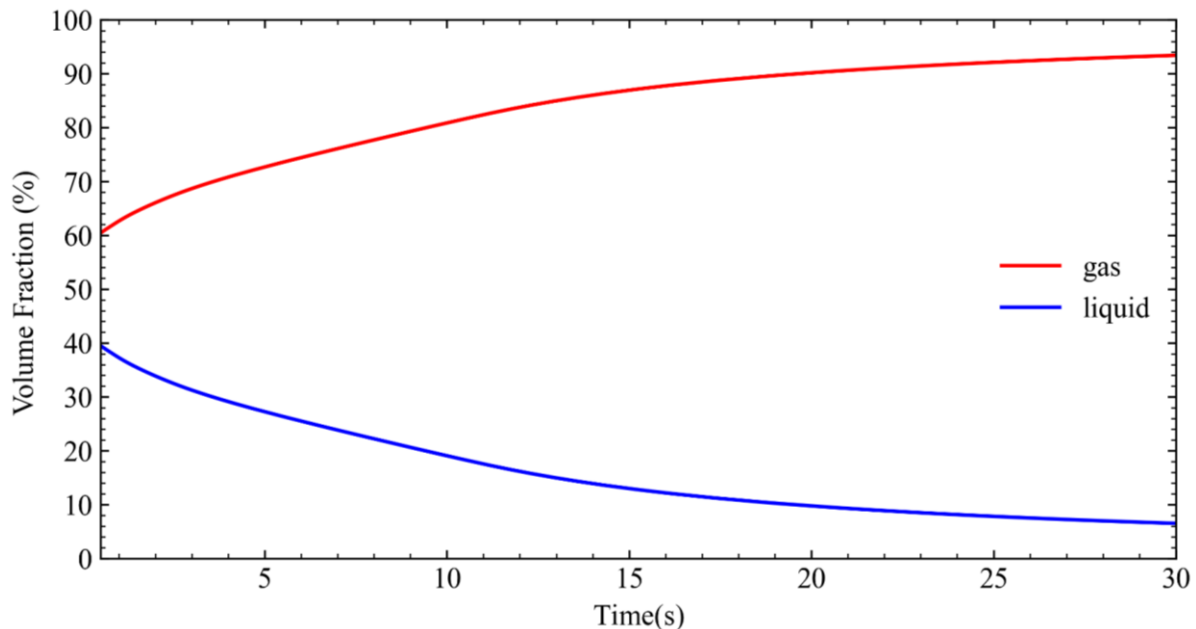
Figure 4.5: Change of the gas and liquid volume fraction with time.

In the initial conditions, the boiling process begins immediately as the box model heats up to a temperature above the boiling point of the liquid. As a result of this heating, hot steam rises due to buoyancy effects, displacing the cooler gas phase. This leads to an increase in both the gas temperature inside the environment and at the outlet for a certain period of time. As the liquid continues to evaporate, the overall amount of liquid decreases, which can be observed in Figure 4.5. After a certain point, the temperature in the gas phase begins to decline as the liquid volume diminishes. Eventually, the system reaches a steady state, at which point the gas temperature at the outlet stabilizes and remains nearly constant. Reaching this steady state is crucial for understanding the long-term behaviour of the boiling process and its impact on heat transfer within the box model. It provides valuable insights into how phase changes influence system performance over time and highlights the importance of initial thermal conditions and fluid dynamics in determining the equilibrium state of the system.
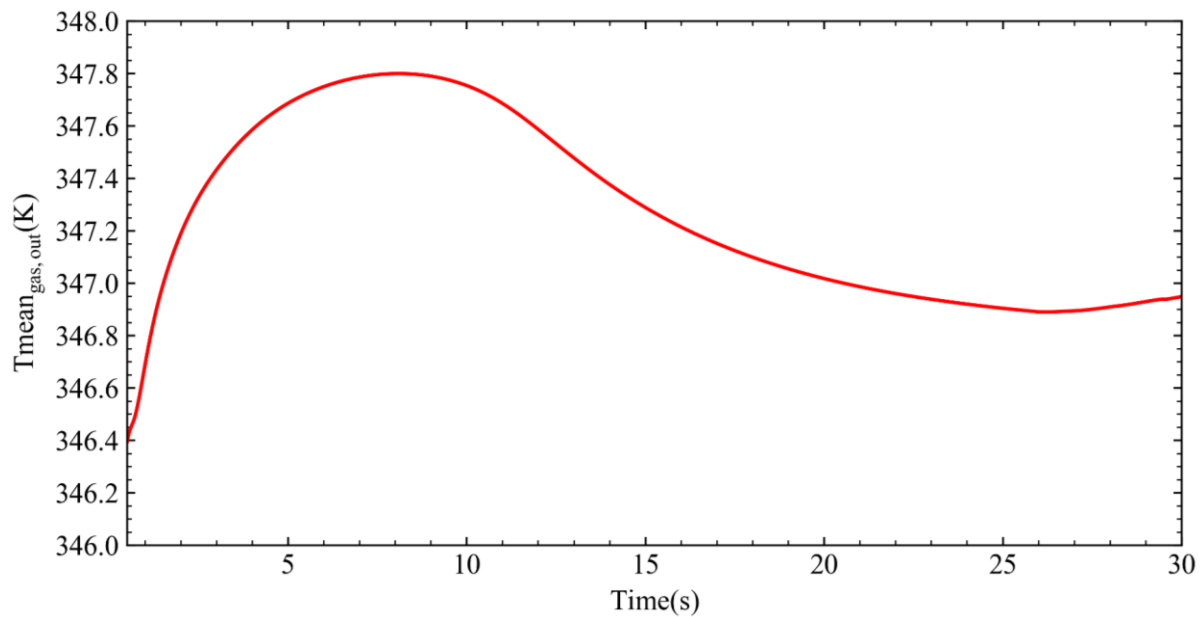
Figure 4.6: Change of mean outlet temperature of vapor phase.

When the model reaches steady-state conditions, the temperature gradient across the box significantly influences the boiling process. Initially, boiling occurs at the interface between the solid and fluid regions. Over time, as the temperature increases upwards, boiling begins to occur at the top of the liquid layer as well. This is due to the phase change initiated when the incoming liquid encounters the critical heat flux, causing rapid vaporization. Figure 4.7 illustrates the mean velocity field and the mean temperature contours along the box under steady-state conditions.
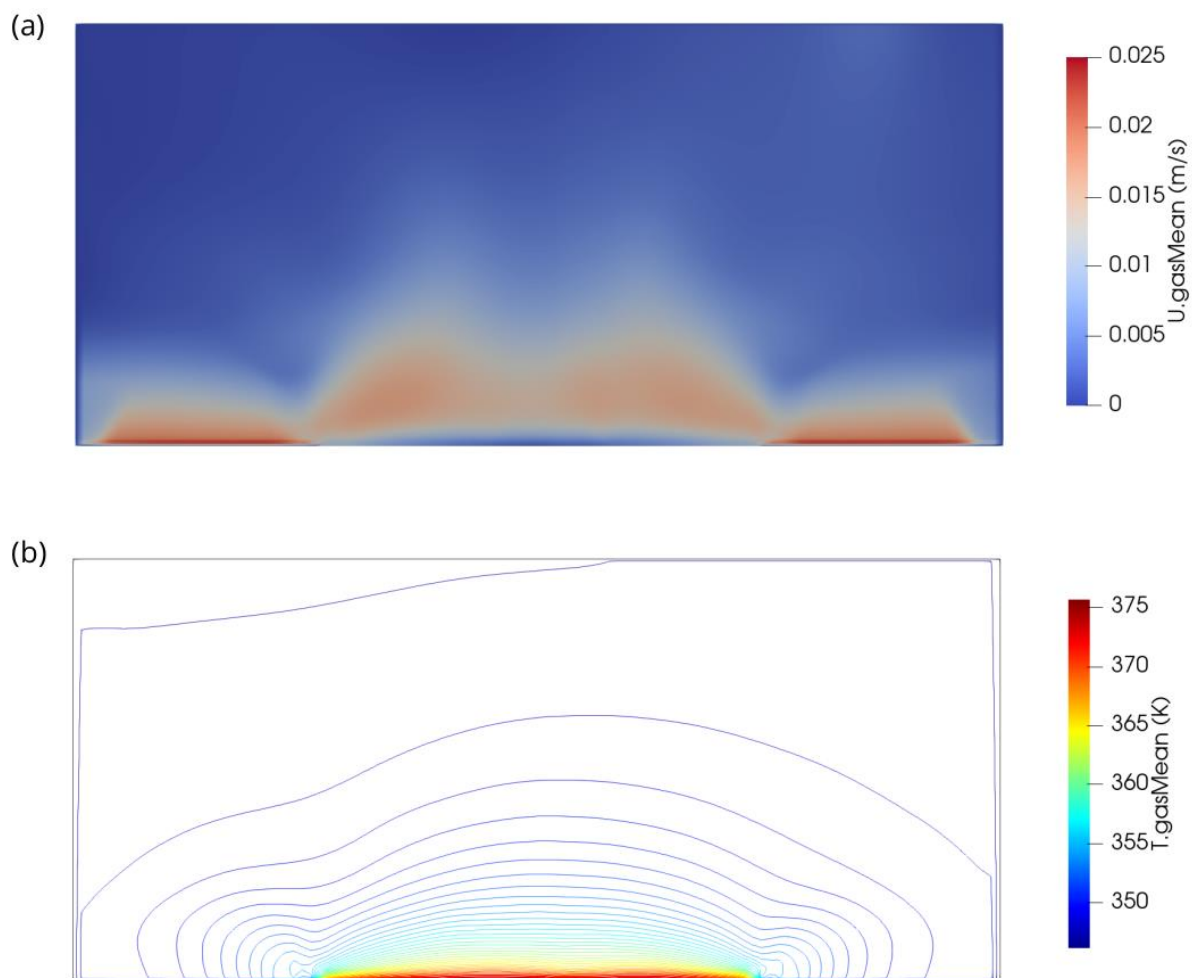
Figure 4.7: a) the mean velocity field and b) the mean temperature contours of the box model.

5. Conclusions

In this study, an open-source CFD model has been developed and validated for the thermal simulations of IT systems. Experimental studies were conducted at Empa data centre using various water flow rates and fan speeds of the cooling system to validate our numerical model. The CHT model is employed for the heat transfer through the heat exchanger of the cooling system. A good agreement between numerical and experimental results shows that the present CHT model can be used reliably for the simulation of waste heat recovery from the data centre. In addition, the following key conclusions can be drawn from the studies conducted in the present study:

1. The present CHT model can predict air and water temperatures at the outlet of the cooling system with a numerical error less than 8%.
2. A series of numerical simulations were performed on the V3.1 Leopard version of the OCP server for the prediction of the Darcy and Forchheimer coefficient in the porous model. Comparison of the full Navier-Stokes solutions with the porous model proves the validity and reliability of the proposed porous model for the modelling of IT equipment in a fast and accurate way.
3. An open-source two-phase model has been developed for the simulation of phase-change heat transfer. The present two-phase model has been validated by comparing numerical results with the available theoretical and numerical results of two benchmark problems in the literature.
4. A micro-baffle design was developed and optimized using the validated two-phase numerical model for the enhancement of heat transfer in two-dimensional film boiling. The proposed baffle design provided a 57.4% improvement in the Nusselt number and a 66.4% increase in critical heat flux (CHF). Our results were published as an open-access paper in the Energies Journal.
5. The validated two-phase thermal model was implemented to the direct-on-chip two-phase cooling model.
6. The present open-source CFD model can be used reliably for the investigation of retrofitting alternatives for pilot sites in our next deliverable. On the other hand, the two-phase model developed in the present study has a potential of maximization of waste heat recovery from servers having high IT loads.

7. Results of two-phase heat transfer studies were submitted to the Future Technologies Symposium of OCP Global Summit. Our study has been accepted by the symposium board as a poster presentation.

6. References

1. Celik, A., Shihada, B., Alouini, M. S. (2018). Wireless data center networks: Advances, challenges, and opportunities. arXiv preprint arXiv:1811.11717. https://doi.org/10.48550/arXiv.1811.11717

2. Simić, M., Prokić, I., Dedeić, J., Sladić, G., Milosavljević, B. (2021). Towards edge computing as a service: Dynamic formation of the micro data-centers. IEEE Access, 9, 114468-114484. https://doi.org/10.1109/ACCESS.2021.3104475

3. Le, N. T., Hossain, M. A., Islam, A., Kim, D. Y., Choi, Y. J., Jang, Y. M. (2016). Survey of promising technologies for 5G networks. Mobile information systems, 2016(1), 2676589. https://doi.org/10.1155/2016/2676589

4. Khalaj, A. H., Halgamuge, S. K. (2017). A Review on efficient thermal management of air-and liquid-cooled data centers: From chip to the cooling system. Applied energy, 205, 1165-1188. https://doi.org/10.1016/j.apenergy.2017.08.037

5. Measuring greenhouse gas emissions in data centres: the environmental impact of cloud computing. Climatiq. Available: https://www.climatiq.io/blog/measure-greenhouse-gas-emissions-carbon-data-centres-cloud-computing

6. Murshed, S. S., De Castro, C. N. (2017). A critical review of traditional and emerging techniques and fluids for electronics cooling. Renewable and Sustainable Energy Reviews, 78, 821-833. https://doi.org/10.1016/j.rser.2017.04.112

7. Akbarzadeh, M., Kalogiannis, T., Jaguemont, J., Jin, L., Behi, H., Karimi, D., Beheshti, H., Mierlo, J.V., Berecibar, M. (2021). A comparative study between air cooling and liquid cooling thermal management systems for a high-energy lithium-ion battery module. Applied Thermal Engineering, 198, 117503. https://doi.org/10.1016/j.applthermaleng.2021.117503

8. Zhang, Z., Wang, X., Yan, Y. (2021). A review of the state-of-the-art in electronic cooling. e-Prime-Advances in Electrical Engineering, Electronics and Energy, 1, 100009. https://doi.org/10.1016/j.prime.2021.100009

9. Pathak, S. K., Sharma, P. O., Goel, V., Bhattacharyya, S., Aybar, H. Ş., Meyer, J. P. (2022). A detailed review on the performance of photovoltaic/thermal system using various cooling methods. Sustainable Energy Technologies and Assessments, 51, 101844. https://doi.org/10.1016/j.seta.2021.101844

10. Ljungdahl, V., Jradi, M., Veje, C. (2022). A decision support model for waste heat recovery systems design in Data Center and High-Performance Computing clusters utilizing liquid cooling and Phase Change Materials. Applied Thermal Engineering, 201, 117671. https://doi.org/10.1016/j.applthermaleng.2021.117671

11. Yuan, X., Liang, Y., Hu, X., Xu, Y., Chen, Y., Kosonen, R. (2023). Waste heat recoveries in data centers: A review. Renewable and Sustainable Energy Reviews, 188, 113777. https://doi.org/10.1016/j.rser.2023.113777

12. Andrae, A. S., Edler, T. (2015). On global electricity usage of communication technology: trends to 2030. Challenges, 6(1), 117-157. https://doi.org/10.3390/challe6010117

13. ASHRAE Technical Committee (TC) 9.9. (2011). Thermal guidelines for data processing environments: Expanded data center classes and usage guidance (White paper). Mission Critical Facilities, Technology Spaces, and Electronic Equipment. Retrieved from https://airatwork.com/wp-content/uploads/ASHRAETC99.pdf

14. Covas, M. T., Silva, C. A., Dias, L. C. (2013). Multicriteria decision analysis for sustainable data centers location. International Transactions in Operational Research, 20(3), 269-299. https://doi.org/10.1111/j.1475-3995.2012.00874.x

15. Uddin, M., Rahman, A. A. (2012). Energy efficiency and low carbon enabler green IT framework for data centers considering green metrics. Renewable and Sustainable Energy Reviews, 16(6), 4078-4094. https://doi.org/10.1016/j.rser.2012.03.014

16. Shehabi, Arman, et al. (2016). United states data center energy usage report. No. LBNL-1005775. Lawrence Berkeley National Lab.(LBNL), Berkeley, CA, United States. https://escholarship.org/content/qt84p772fc/qt84p772fc.pdf

17. Techerati. (2023). Data centres use 18% of all electricity in Ireland. Retrieved from https://www.techerati.com/news-hub/data-centres-ireland-electricity-consumption [accessed July 22, 2024].

18. Global Action Plan an inefficient truth (2007). Retrieved from https://www.greenict.org.uk/sites/default/files/An%20Inefficient%20Truth%20-%20Executive%20Summary.pdf [accessed June 3, 2024].

19. Yuan, X., Xu, X., Wang, Y., Liu, J., Kosonen, R., Cai, H. (2020). Design and validation of an airflow management system in data center with tilted server placement. Applied thermal engineering, 164, 114444. https://doi.org/10.1016/j.applthermaleng.2019.114444

20. Moazamigoodarzi, H., Gupta, R., Pal, S., Tsai, P. J., Ghosh, S., Puri, I. K. (2020). Modeling temperature distribution and power consumption in IT server enclosures with row-based cooling architectures. Applied energy, 261, 114355. https://doi.org/10.1016/j.apenergy.2019.114355

21. Asgari, S., MirhoseiniNejad, S., Moazamigoodarzi, H., Gupta, R., Zheng, R., Puri, I. K. (2021). A gray-box model for real-time transient temperature predictions in data centers. Applied Thermal Engineering, 185, 116319. https://doi.org/10.1016/j.applthermaleng.2020.116319

22. Almoli, A., Thompson, A., Kapur, N., Summers, J., Thompson, H., Hannah, G. (2012). Computational fluid dynamic investigation of liquid rack cooling in data centres. Applied energy, 89(1), 150-155. https://doi.org/10.1016/j.apenergy.2011.02.003

23. Moazamigoodarzi, H., Pal, S., Ghosh, S., Puri, I. K. (2018). Real-time temperature predictions in it server enclosures. International Journal of Heat and Mass Transfer, 127, 890-900. https://doi.org/10.1016/j.ijheatmasstransfer.2018.08.091

24. Moazamigoodarzi, H., Pal, S., Down, D., Esmalifalak, M., Puri, I. K. (2020). Performance of a rack mountable cooling unit in an IT server enclosure. Thermal Science and Engineering Progress, 17, 100395. https://doi.org/10.1016/j.tsep.2019.100395

25. Ebrahimi, K., Jones, G. F., Fleischer, A. S. (2014). A review of data center cooling technology, operating conditions and the corresponding low-grade waste heat recovery opportunities. Renewable and sustainable energy reviews, 31, 622-638. https://doi.org/10.1016/j.rser.2013.12.007

26. Agostini, B., Fabbri, M., Park, J. E., Wojtan, L., Thome, J. R., Michel, B. (2007). State of the art of high heat flux cooling technologies. Heat transfer engineering, 28(4), 258-281. https://doi.org/10.1080/01457630601117799

27. Leonard, P. L., & Phillips, A. L. (2005). The Thermal Bus Opportunity-A Quantum Leap in Data Center Cooling Potential. ASHRAE transactions, 111(2). https://citeseerx.ist.psu.edu/document?repid=rep1&type=pdf&doi=05182c030cd5f471bca26bc71b2b0b3c965a4d17

28. Ganapati, P. (2009). Water-Cooled Supercomputer Doubles as Dorm Space Heater. Retrieved from https://www.wired.com/2009/06/ibm-supercomputer/ [accessed June 3, 2024].

29. Deymi-Dashtebayaz, M., Valipour-Namanlo, S. (2019). Thermoeconomic and environmental feasibility of waste heat recovery of a data center using air source heat pump. Journal of Cleaner Production, 219, 117-126. https://doi.org/10.1016/j.jclepro.2019.02.061

30. Rong, H., Zhang, H., Xiao, S., Li, C., Hu, C. (2016). Optimizing energy consumption for data centers. Renewable and Sustainable Energy Reviews, 58, 674-691. https://doi.org/10.1016/j.rser.2015.12.283

31. Hiltunen, P., Syri, S. (2021). Low-temperature waste heat enabling abandoning coal in Espoo district heating system. Energy, 231, 120916. https://doi.org/10.1016/j.energy.2021.120916

32. Montagud-Montalvá, C., Navarro-Peris, E., Gómez-Navarro, T., Masip-Sanchis, X., Prades-Gil, C. (2023). Recovery of waste heat from data centres for decarbonisation of university campuses in a Mediterranean climate. Energy Conversion and Management, 290, 117212. https://doi.org/10.1016/j.enconman.2023.117212

33. Manickam, M. S. J. M., Schwarz, M. P., & Perry, J. (1998). CFD modelling of waste heat recovery boiler. Applied mathematical modelling, 22(10), 823-840. https://doi.org/10.1016/S0307-904X(98)10020-3

34. Sajjad R., Hussain M., Khan S.U., Rehman A., Khan M.J., Tlili I., Ullah S. (2024). CFD analysis for different nanofluids in fin prolonged heat exchanger for waste heat

recovery. South African Journal of Chemical Engineering. https://doi.org/10.1016/j.sajce.2023.10.005

35. Roumpedakis, T.C., Chapaloglou, S., Pallis, P., Leontaritis, A. D., Braimakis, K., Karellas, S., Vourliotis, P. (2017). Experimental investigation and CFD analysis of heat transfer in single phase subcooler of a small scale waste heat recovery ORC. Energy Procedia, 129, 487-494. https://doi.org/10.1016/j.egypro.2017.09.166

36. Groeneveld, D.C., Shan, J.Q., Vasic, A.Z., Leung, L.K.H., Durmayaz, A., Yang, J., Cheng, S.C., Tanase, A. (2007). The 2006 CHF look-up table. Nuclear Engineering and Design, 237(15-17), 1909-1922. https://doi.org/10.1016/j.nucengdes.2007.02.014

37. Tong, L.S., Weisman, J. (1979). Thermal Analysis of Pressurized Water Reactors. American Nuclear Society.

38. Totten, G.E., Bates, C.E., Clinton, N.A. Spray Quenching. (1993). In Handbook of Quenchants and Quenching Technology. (1st ed). Haddad, M.T., ASM International USA.

39. Faghri, A., Zhang, Y. (2006). Transport Phenomena in Multiphase Systems. (1st ed). Academic Press USA.

40. You, S. M., Kim, J. H., Kim, K. H. (2003). Effect of nanoparticles on critical heat flux of water in pool boiling heat transfer. Applied physics letters, 83(16), 3374-3376. https://doi.org/10.1063/1.1619206

41. Park, S.D., Lee, S.W., Kang, S., Bang, I.C., Kim, J.H., Shin, H.S., Lee, D.W., Lee, D.W.. (2010). Effects of nanofluids containing graphene/graphene-oxide nanosheets on critical heat flux. Appl. Phys. Lett. 97(2) 023103. https://doi.org/10.1063/1.3459971

42. Mori, S. Okuyama, K. (2009). Enhancement of the critical heat flux in saturated pool boiling using honeycomb porous media. Int. J.Multiph. Flow 35, 946–951. https://doi.org/10.1016/j.ijmultiphaseflow.2009.05.003

43. Wang, K., Gong, H., Wang, L., Erkan, N., Okamoto, K. (2020). Effects of a porous honeycomb structure on critical heat flux in downward facing saturated pool boiling. Appl. Therm. Eng., 170, 115036. https://doi.org/10.1016/j.applthermaleng.2020.115036

44. Hao, W., Wang, T., Jiang, Y.-Y., Guo, C., Guo, C.H. (2017). Pool boiling heat transfer on deformable structures made of shape-memory-alloys. Int. J. Heat Mass Transf. 112, 236–247. https://doi.org/10.1016/j.ijheatmasstransfer.2017.04.113

45. Surtaev, A., Kuznetsov, D., Serdyukov, V., Pavlenko, A., Kalita, V., Komlev, D., Ivannikov, A., Radyuk, A. (2018). Structured capillary-porous coatings for enhancement of heat transfer at pool boiling. Appl. Therm. Eng., 133, 532-542. https://doi.org/10.1016/j.applthermaleng.2018.01.051

46. Das, S., Saha, B., Bhaumik, S. (2017). Experimental study of nucleate pool boiling heat transfer of water by surface functionalization with SiO2 nanostructure. Exp. Therm. Fluid Sci., 81, 454–465. https://doi.org/10.1016/j.expthermflusci.2016.09.009

47. Kunkelmann C. (2011). Numerical modeling and investigation of boiling phenomena. Doctoral thesis, Technische Universität Darmstadt, Darmstadt, Germany. https://tuprints.ulb.tu-darmstadt.de/2731/1/PhD_Thesis_Kunkelmann.pdf

48. Ginzburg, I., Wittum, G. (2001). Two-phase flows on interface refined grids modeled with VOF, staggered finite volumes and spline interpolants. J. Comput. Phys., 166(2), 302-335. https://doi.org/10.1006/jcph.2000.6655

49. Hirt C.W., Nichols B.D. (1981). Volume of fluid (VOF) method for the dynamics of free boundary. J. Comput. Phys., 39(1), 201-225. https://doi.org/10.1016/0021-9991(81)90145-5

50. Yakubov, S., Cankurt, B., Maquil, T., Schiller, P., Abdel-Maksoud, M., Rung, T. (2011). Euler-Euler and Euler-Lagrange approaches to cavitation modelling in marine applications. CIMNE, 544-555. https://upcommons.upc.edu/bitstream/handle/2117/333280/Marine-2011-42_EULER-EULER%20AND%20EULER-LAGRANGE.pdf?sequence=1&isAllowed=y

51. Valizadeh, Z., Shams, M. (2016). Numerical investigation of water-based nanofluid subcooled flow boiling by three-phase Euler–Euler, Euler–Lagrange approach. Heat and Mass Transfer, 52, 1501-1514. https://doi.org/10.1007/s00231-015-1675-3

52. Butaye, E., Toutant, A., Mer, S. (2023). Euler–Euler Multi-Scale Simulations of Internal Boiling Flow with Conjugated Heat Transfer. Applied Mechanics, 4(1), 191-209. https://doi.org/10.3390/applmech4010011

53. Chen, M., Liu, M., Tang, Y. (2019). Comparison of Euler-Euler and Euler-Lagrange approaches for simulating gas-solid flows in a multiple-spouted bed. International Journal of Chemical Reactor Engineering, 17(7), 20180254. https://doi.org/10.1515/ijcre-2018-0254

54. Groll, R., Jakirlić, S., Tropea, C. (2009). Comparative study of Euler/Euler and Euler/Lagrange approaches simulating evaporation in a turbulent gas–liquid flow. International journal for numerical methods in fluids, 59(8), 873-906. https://doi.org/10.1002/fld.1844

55. Lou, W., Zhu, M. (2013). Numerical simulation of gas and liquid two-phase flow in gas-stirred systems based on Euler–Euler approach. Metallurgical and Materials Transactions B, 44, 1251-1263. https://doi.org/10.1007/s11663-013-9897-6

56. Van Sint Annaland, M., Deen, N.G., Kuipers, J.A.M. (2005). Numerical simulation of gas bubbles behaviour using a three-dimensional volume of fluid method. Chemical engineering science, 60(11), 2999-3011. https://doi.org/10.1016/j.ces.2005.01.031

57. Welch, S.W., Wilson, J. (2000). A volume of fluid based method for fluid flows with phase change. J. Comput. Phys., 160(2), 662-682. https://doi.org/10.1006/jcph.2000.6481

58. Kleefsman, K.M.T., Fekken, G., Veldman, A.E.P., Iwanowski, B., Buchner, B. (2005). A volume-of-fluid based simulation method for wave impact problems. J. Comput. Phys., 206(1), 363-393. https://doi.org/10.1016/j.jcp.2004.12.007

59. Zeng, Q., Cai, J., Yin, H., Yang, X., Watanabe, T. (2015). Numerical simulation of single bubble condensation in subcooled flow using OpenFOAM. Progress in Nuclear Energy, 83, 336-346. https://doi.org/10.1016/j.pnucene.2015.04.011

60. Deshpande, S.S., Anumolu, L., Trujillo, M. F. (2012). Evaluating the performance of the two-phase flow solver interFoam. Computational science & discovery, 5(1), 014016. http://doi.org/10.1088/1749-4699/5/1/014016

61. Wilcox, D.C. (2008). Formulation of the k-ω turbulence model revisited. AIAA J., 46, 2823–2838. https://doi.org/10.2514/1.36541

62. OpenFOAM. User Guide., Available: https://doc.cfd.direct/openfoam/user-guide-v11/index

63. Dogan A., Yilmaz S., Kuzay M., Yilmaz C., Demirel E., (2022). CFD Modeling of Pressure Drop through an OCP Server for Data Center Applications. Energies, 15, 6438. https://doi.org/10.3390/en15176438

64. Sheth, D.V., Saha, S.K. (2019). Numerical study of thermal management of data centre using porous medium approach. J. Build. Eng., 22, 200–215. https://doi.org/10.1016/j.jobe.2018.12.012

65. Empa, Swiss Federal Laboratories for Materials Science and Technology. Available: https://www.empa.ch/

66. Hosseini, S. A., Kouhikamali, R. (2019). A numerical investigation of various phase change models on simulation of saturated film boiling heat transfer. Heat Transfer—Asian Research, 48(6), 2577-2595. https://doi.org/10.1002/htj.21514

67. Samkhaniani, N., Ansari, M. R. (2016). Numerical simulation of bubble condensation using CF-VOF. Progress in Nuclear Energy, 89, 120-131. https://doi.org/10.1016/j.pnucene.2016.02.004

68. Lee, W. H. (1980). A pressure iteration scheme for two-phase flow modeling. Multiphase transport fundamentals, reactor safety, applications, 1, 407-431. https://codethatflows.wordpress.com/wp-content/uploads/2021/08/406441216-lee-model-pdf-1.pdf

69. Chen, G., Nie, T., Yan, X. (2020). An explicit expression of the empirical factor in a widely used phase change model. International Journal of Heat and Mass Transfer, 150, 119279. https://doi.org/10.1016/j.ijheatmasstransfer.2019.119279

70. Yang, Z., Peng, X. F., Ye, P. (2008). Numerical and experimental investigation of two phase flow during boiling in a coiled tube. International Journal of Heat and Mass Transfer, 51(5-6), 1003-1016. https://doi.org/10.1016/j.ijheatmasstransfer.2007.05.025

71. Fang C, David M, Rogacs A, Goodson K. (2010). Volume of fluid simulation of boiling two-phase flow in a vapor-venting microchannel. Frontiers Heat and Mass Transfer, 1:1-11. https://doi.org/10.5098/hmt.v1.1.3002

72. Brackbill, J.U., Kothe, D.B., Zemach, C. (1992). A continuum method for modeling surface tension. J. Comput. Phys., 100, 335–354. https://doi.org/10.1016/0021-9991(92)90240-Y

73. Reimann, M., Grigull, U. (1975). Free convection and film boiling heat transfer in the critical region of water and carbon dioxide. Wärme-und Stoffübertragung, 8, 229-239. https://doi.org/10.1007/BF01002151

74. Klimenko V.V. (1981). Film boiling on a horizontal plate—new correlation. International Journal of Heat and Mass Transfer, 24(1), 69-79. https://doi.org/10.1016/0017-9310(81)90094-6

75. Berenson P. (1961). Film-boiling heat transfer from a horizontal surface. J Heat Transfer, 83(3), 351-356. https://doi.org/10.1115/1.3682280

76. Seo, H., Bang, I. C. (2016). Revisiting the Rayleigh–Taylor instability and critical heat flux with R-123 for different heater sizes and pressures. International Journal of Thermal Sciences, 100, 324-332. https://doi.org/10.1016/j.ijthermalsci.2015.10.014

77. Hypercool: The waterless liquid cooling solution for Ai + Hpc. Zutacore. Available: https://zutacore.com/solutions/

78. Yang, Z., Herb, J. (2023). Numerical simulation of subcooled flow boiling for nuclear engineering applications using OpenFOAM. Kerntechnik, 88(2), 174-185. https://doi.org/10.1515/kern-2022-0112

79. Godino, D. M., Corzo, S. F., Ramajo, D. E. (2022). CFD simulation of conjugated heat transfer with full boiling in OpenFOAM (R). Applied Thermal Engineering, 213, 118627. https://doi.org/10.1016/j.applthermaleng.2022.118627

80. Shala, M. (2012). Simulation of nucleate boiling flow using a multiphase mixture modelling approach. IMA Journal of Applied Mathematics, 77(1), 47-58. https://doi.org/10.1093/imamat/hxr074

81. Opteon SF33 Speciality fluid, Available: https://www.opteon.com/en/-/media/files/opteon/opteon-sf33-specialty-fluid-technical-bulletin.pdf?rev=67b973acd80745ea841f750921f743f5

82. Wang, H., Xiong, J., Wang, J. (2023). Development and assessment of five-component wall boiling heat flux partitioning model. International Journal of Multiphase Flow, 158, 104306. https://doi.org/10.1016/j.ijmultiphaseflow.2022.104306

83. Parida, P. R., Tsuei, H. H., Chainer, T. J. (2015). Eulerian multiphase conjugate model for chip-embedded micro-channel flow boiling. American Society of Mechanical Engineers., In International Electronic Packaging Technical Conference and Exhibition, Vol. 56901, p. V003T10A027. https://doi.org/10.1115/IPACK2015-48489

84. Cole, R. (1967). Bubble frequencies and departure volumes at subatmospheric pressures. AIChE Journal, 13(4), 779-783. https://doi.org/10.1002/aic.690130434

85. Walker, J. (2010). Boiling and the Leidenfrost effect. Fundamentals of physics, E10-1. https://www.reed.edu/physics/332/pdf/Leidenfrost.pdf

86. Bressler, R. G. (1972). A Review of Physical Models and Heat-Transfer Correlations for Free-Convection Film Boiling. In Advances in Cryogenic Engineering: A Collection of Invited Papers and Contributed Papers Presented at National Technical Meetings During 1970 and 1971, Springer US, 382-406. https://doi.org/10.1007/978-1-4684-7826-6_41

7. List of figures

8. List of tables